A Dynamo Case Study of Mercury, and the Early Orbital and Thermal Evolution of the Moon

by

ZhenLiang Tian

B.S., University of Science and Technology of China (2007)

Submitted to the Department of Earth, Atmospheric and Planetary Sciences
In Partial Fulfillment of the Requirements for the Degree of

Doctor of Philosophy

at the

MASSACHUSETTS INSTITUTE OF TECHNOLOGY

February 2017

© Massachusetts Institute of Technology 2016. All rights reserved.

Signature of Author: Signature redacted
Department of Earth, Atmospheric and Planetary Sciences
October, 2016

Certified by: Signature redacted
Maria T. Zuber
E. A. Griswold Professor of Geophysics
Thesis Supervisor

Accepted by: Signature redacted
Robert Van der Hilst
Schlumberger Professor of Earth and Planetary Sciences
Department Head

MASSACHUSETTS INSTITUTE OF TECHNOLOGY
FEB 22 2017
LIBRARIES
ARCHIVES

Abstract

Mercury's magnetic field is characterized by its weak strength, spin-aligned axisymmetry and a large offset of the magnetic equator relative to Mercury's geographic equator. The combination of these features is difficult to be explained with an Earth-like dynamo. We enhance the traditional dynamo model by adding a stably stratified layer in Mercury's core and a north-south asymmetric heat flux pattern at the core-mantle boundary, and find multiple cases in which the surface magnetic field exhibits all the observed characteristics. This result supports either thermal or chemical stratification at the top of Mercury's core, and suggests that the northern hemisphere mantle could be more convective, which could be caused by moderately elevated concentration of heat-producing elements in that region.

The isotopic similarity between the Earth and Moon and the volatile depletion of the Moon collectively suggest the Moon-forming impact to have been a high-energy, high-angular momentum event. The excess angular momentum of the post-impact Earth-Moon system was suggested to have been drained through an orbital resonance mechanism. We find an alternative mechanism, a limit cycle, that can reduce angular momentum over a much broader parameter range. We couple the orbital evolution with lunar magma ocean solidification to assess the mutual effects of orbital processes and the Moon's thermal profile on each other. We find that the resonance is unstable for causing severe tidal heating in the Moon, while the limit cycle works with satisfaction in the coupled model. Consequently, the limit cycle is a more viable mechanism than the resonance to drain the excess angular momentum.

Lunar volcanism is mainly concentrated in the lunar nearside. Researchers proposed that this hemispheric asymmetry could be the result of a single diaper ascension of deep, radiogenically heated material, but it is unclear why the diaper occurred in the nearside mantle. In an attempt to explain this observation by heterogeneous tidal heating, we computed the distribution of tidal heating in the lunar mantle, and find that tidal distortion is unable to concentrate heating and cause the diaper to occur in the lunar nearside when a spherically symmetric structure of the Moon is assumed.

Contents

Symbols

G	gravitational constant
m_e	mass of the Earth
R_e	radius of the Earth
Q_e	dissipation factor of the Earth
k_{2e}	degree-2 potential Love number of the Earth
m_m	mass of the Moon
R_m	radius of the Moon
Q_m	dissipation factor of the Moon
k_{2m}	degree-2 potential Love number of the Moon

Introduction

This thesis presents research performed during my graduate study. The projects reflect my interest in the relationships between the internal structure of rocky planetary bodies, and their orbital and rotational evolution. The thesis contains four parts: (1) dynamo simulations of Mercury's asymmetric magnetic field assuming a stable layer in the core and laterally heterogeneous heat flux at the core-mantle boundary; (2) the orbital evolution of the early Earth-Moon system with a fast-spinning Earth; (3) the coupled orbital-thermal evolution of the early Earth-Moon system; and (4) an assessment on the role of tidal heating in producing the magmatic asymmetry of the Moon. These topics are briefly introduced below.

1

Mercury's magnetic field is full of unexpected mysteries.

Since the MESSENGER spacecraft's arrival at Mercury in 2008, it gradually accumulated enough measurements to determine the strength and configuration of the planet's magnetic field (Anderson *et al.*, 2011, 2012). The weakness of the field, as expected from data acquired from Mariner 10's flybys of Mercury in the 1970s, is confirmed. The magnetic dipole moment is refined to $\sim 190\text{nT}\cdot r_{planet}^3$, less than 1/100 that of the Earth ($\sim 3\times10^4\text{nT}\cdot R_e^3$). This weak field strength can not be explained by an Earth-like dynamo. Indeed, the weakness of the field, which has been known since the 1970s, has led groups of researchers to speculate the magnetic field to be a crustal remanent field (Stephenson 1975; Srnka 1976; Aharonson *et al.*, 2004). After MESSENGER's measurements of the field's configuration, we have more confidence in an active dynamo origin of the field, but we still need future detection of temporal variations of the field to confirm its dynamo origin.

In addition to confirming Mercury field's weakness, the MESSENGER data has also revealed intriguing features about the configuration of the field. As shown in Fig. 1, the magnetic field is very axisymmetric about the spin axis of Mercury, with the magnetic axis aligned to within 0.8° of

the spin axis. On the other hand, the field strength in the northern hemisphere is much stronger than in the southern hemisphere. This north-south asymmetry can be interpreted as a large offset of 480 km (~20% of Mercury's radius) of the magnetic equator from the geographic equator, or, in terms of spherical harmonic components, a large quadrupole in addition to the conventionally dominant dipole (Anderson *et al.*, 2011; 2012).

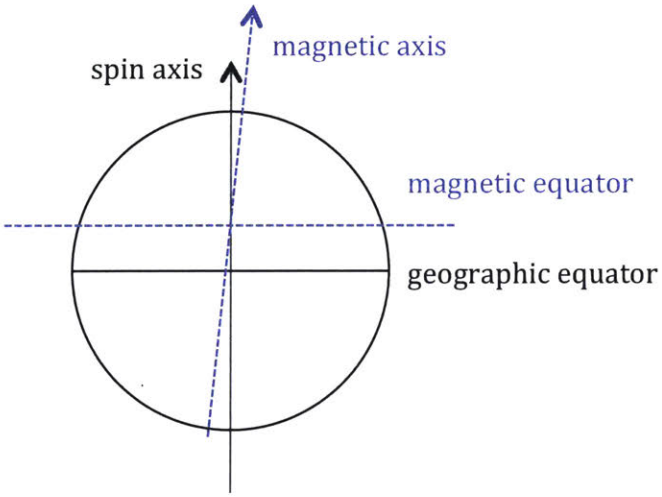

Fig. 1. The configuration of Mercury's magnetic field. The tilt between the two axes and the magnetic equator's offset are exaggerated for view.

This combination of spin-aligned axisymmetry and a large magnetic equator offset has only been observed for Mercury, among all dynamo generated magnetic fields in the solar system, making it an intriguing exception to the norm. Saturn's magnetic field also exhibits spin-aligned axisymmetry (with the tilt less than 1°), but it is north-south symmetric. The combination of these two features is contrary to the predictions of conventional dynamo theory and simulation results. This contradiction can be illustrated in terms of the Gauss coefficients, or the coefficients of the spherical harmonic expansion of planetary magnetic fields. Let g_{lm}, h_{lm} denote the degree-l, order-m coefficients. In this formalism g_{10} denotes the spin-axisymmetric dipole, and g_{11}, h_{11} denote the equatorial dipoles (with their dipole axes lying on the geographic equator). The spin-aligned axisymmetry corresponds to a small $sqrt(g_{11}^2 + h_{11}^2)/g_{10}$ ratio, and the large offset corresponds to a large g_{20}/g_{10} ratio (0.40). Therefore, Mercury's case requires small g_{11}, h_{11} and a large g_{20}. However, in dynamo theories, when the g_{20} mode is excited, the g_{11}, h_{11} modes will also

be activated and strengthened. This is because their *degree+order* numbers are all even and have similar wavelengths, and therefore they belong to the same family (Bullard and Gellman, 1954).

In chapter 1 of the thesis, we will show that by the application of a stratified layer to the top of the outer core, and the use of laterally heterogeneous, north-south asymmetric heat flux at the core-mantle boundary, the dynamo model is able to produce a magnetic field that is weak, highly axisymmetrically aligned with the spin axis, and significantly north-south asymmetric.

To explain the spin-aligned axisymmetry of Saturn's magnetic field, Stevenson (1980) proposed that a stably stratified layer of metallic H-He liquid acts to "axisymmetrize" the surface magnetic field. Since helium is immiscible with hydrogen in the molecular-metallic transition zone, it would rain out of the molecular H-He mixture and become enriched in the metallic H-He region. An inhomogeneous, stably stratified layer of metallic liquid would form in the top of the metallic region (Fig. 2). This layer does not participate in the metallic liquid convection, thus limits the dynamo region to deeper depths. The liquid in this stable layer is in differential rotation due to the equator-to-pole temperature differences, and it is shown by analysis that the differential rotation causes attenuation of the non-axisymmetric components of the magnetic field and does not affect the axisymmetric parts when the Rossby number (the ratio of convection to Coriolis force) is large.

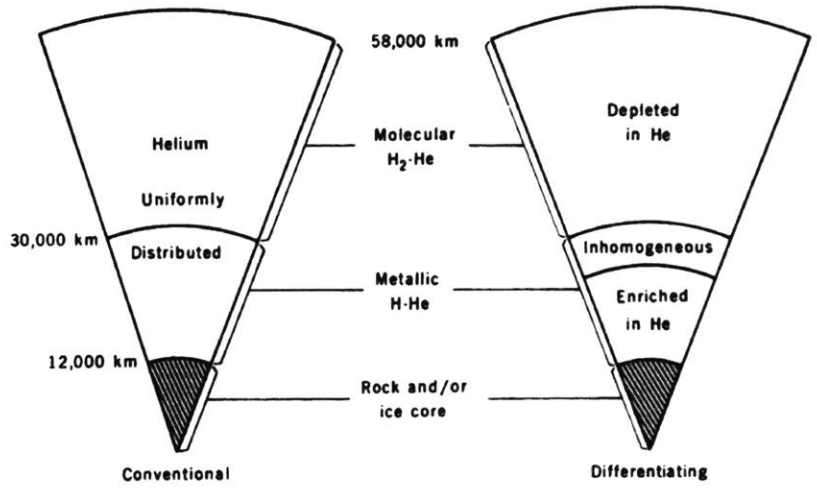

Fig. 2. (From Stevenson 1980) Conventional and proposed internal cross-section of Saturn showing the inhomogeneous stably stratified metallic liquid layer above the dynamo region.

A stably stratified layer could also form in Mercury's outer core by thermal or chemical stratification. Hauck *et al.* (2004) suggested a subadiabatic heat flux at Mercury's core-mantle boundary (CMB). A subadiabatic CMB heat flux leads to a region of stratification at the top of the core. The stable layer can alternatively be a consequence of FeS enrichement in the top region of the core. Mercury's surface sulfur and iron contents indicate a chemically reducing environment for the planet's formation (Nittler *et al.*, 2011), which favors an enrichment of sulfur and silicon in the core. Enriched sulfur in the core could be in the form of FeS, whose liquid mixture property in the high-temperature, high pressure Fe-Ni-S-Si system is complex. If FeS were immiscible with the Fe and Ni core liquids under certain conditions, a stably stratified layer of FeS rich liquid would form at the top of the core.

We applied a north-south asymmetric heat flux pattern at the CMB, with stronger flux in the northern hemisphere. This pattern is supported by the observations of surface K distribution (Peplowski *et al.*, 2012) and the existence of large expanses of volcanic plains near Mercury's north pole as revealed by MESSENGER imaging (Head *et al.*, 2011). The surface concentration of K and other heat-producing elements is moderately higher in the northern high latitudes than in the equatorial regions. The distribution of these elements in the southern hemisphere is currently unknown due to the MESSENGER spacecraft's highly eccentric orbit, which takes the spacecraft too far from Mercury's surface in the southern hemisphere to obtain reliable compositional observations. It is possible that the southern high latitude regions do not possess elevated concentrations of K, and the global surface distribution of K and other heat-producing elements shows a north-south asymmetry with higher concentrations in the north. The surface K variations are interpreted to reflect the compositions of the intrinsic crustal material (Weider *et al.*, 2015). In the case of north-south asymmetry, the surface K distribution could further suggest moderately elevated K concentrations in the northern hemisphere mantle. Since Mercury's mantle is just unstable enough to be in the convective state (Michel *et al.*, 2013), moderately stronger radiogenic heating in the mantle in the northern high latitudes would substantially promote convection there, resulting in either increased rates of convection than other regions, or the occurrence of convection when there is no convection in the southern regions. Either case

will result in stronger heat flux in the north. The presence of the northern smooth plains (Head *et al.*, 2011) also suggests more vigorous mantle thermal activity in the northern high latitudes at the formation time of these plains. Even though this volcanic activity occurred more than 3.8-3.9 billion years ago, it can still be related to the current day CMB heat flux pattern if the elevated volcanism in the northern high latitudes was caused by elevated concentrations of heat-producing elements in the mantle there. The small spatial scales of Mercury's mantle convection cells and overall low activity (Michel *et al.*, 2013) is unlikely to have laterally redistributed mantle material globally, so a pattern of elevated concentration of heat-producing elements in the northern mantle in the ancient eras would have persisted to the present day.

With the application of a stably stratified layer in the core and a variable heat flux at the CMB, and by varying the inner core size, the size of the stable layer, and magnitude of the variable heat flux, we find multiple dynamo cases in which the surface magnetic field exhibit all the three observed characteristics of Mercury's magnetic field. The weak intensity of the surface field is due partly to the stable layer's limiting the dynamo region to the deeper regions of the core, and more importantly, to the skin effect of the stable layer in damping out the high frequency components of the magnetic field in the dynamo region. The latitudinal variability of the CMB heat flux induces differential rotation in the stable layer, which attenuates the non-axisymmetric components of the magnetic field.

2 & 3

The origin of the Moon is strictly constrained by the range of possible lunar orbital histories.

In the early 2000s, with Canup & Asphaug's (2001) then unprecedentedly complex and detailed simulations and visualizations of the proposed Moon-forming giant impact, an impact scenario, since then commonly referred to as the standard model, became widely recognized and accepted as the most probable scenario as the origin of the Moon. One of its key advantages is that the resultant Earth rotates with a ~5 hour period, which is close to expectations based on the current value of the Earth-Moon system's total angular momentum. It was then taken for granted that the Earth-Moon system's total angular momentum, which is the sum of the orbital angular

momentum and the two bodies' individual rotational angular momentum, has stayed relatively constant since the Moon's formation throughout the solar system's history.

It is this angular momentum constraint that helped bring the demise of other lunar formation hypotheses, such as the fission hypothesis. It is also this constraint that filtered out a wide range of possible impact scenarios in numerical simulations like Canup & Asphaug's (2001), limiting the possible scenarios to those in which the bulk of lunar material predominantly comes from the impactor, not the proto-Earth.

As time proceeds, the science community found insights and conflicts on the lunar origin from the chemical perspective. Wiechert *et al.* (2001) reported identical oxygen isotopic compositions between the lunar and terrestrial samples. This is in direct conflict with the standard impact scenario: if the lunar material had predominantly come from the impactor, how can the Moon possess the same isotopic signature as the Earth? Pahlevan & Stevenson (2007) later proposed a chemical equilibration mechanism between the post-impact Earth and the proto-lunar disk to account for the oxygen similarity. However, Zhang *et al.* (2012) reported another species of isotopes that appear to be identical in the Moon and the Earth: titanium. Unlike the volatile oxygen, titanium is highly refractory, and thus unlikely to be equilibrated between the Earth and the disk.

Therefore, titanium, along with other isotopic similarities (O, W, Cr), puts the standard model in question: either the lunar material has a substantial terrestrial contribution, or the impactor is isotopically identical with the proto-Earth by coincidence (Mastrobuono-Battisti *et al.*, 2015; Kaib and Cowan, 2015). The latter possibility is unsatisfying.

Several groups (Cuk and Stewart, 2012; Canup, 2012; Reufer *et al.*, 2012) focused on the first possibility, and identified numerical impact scenarios in which the bulk lunar material largely derives from the proto-Earth. All these scenarios assumed the impact angular momentum to be much larger than the current Earth-Moon value. In the scenario of Reufer *et al.* (2012), also known as the "hit and go" model, the excess angular momentum is drained from the system by the escape of a portion of the impactor material from the Earth's gravity. In both the Cuk and

Stewart (2012) and Canup (2012) models, the excess angular momentum remains in the rotation of the Earth after the impact, causing a fast-spinning Earth with the rotational period as short as 2.5 hours.

Lock *et al.* (2016) proposed that impact scenarios that leave the Earth in a fast-spinning, *i.e.*, high-angular momentum state have the advantage of being able to explain the depletion of volatiles in the Moon. After a high-energy, high-angular momentum giant impact, the Earth could be in a post hot spin stability limit state, in which the Earth's mantle, atmosphere, and the circumplanetary disk (MAD) form an extended structure with no discontinuities in it. This MAD structure of bulk silicate Earth (BSE) vapor can extend beyond the Roche limit. The observed depletion of volatiles in the Moon, as well as the isotopic similarities between the Earth and Moon, is a natural result of the condensing Moon equilibrating with the BSE vapor. The enrichment of the heavy potassium isotopes in the Moon reported by Wang and Jacobsen (2016) supports this model of lunar accretion. On this basis it appears that a fast-spinning post-impact Earth is more likely.

Starting from a fast-spinning Earth, the excess angular momentum should be drained in the subsequent history through orbital dynamics mechanisms, or the two scenarios would fail even though they succeed in producing an Earthlike proto-lunar disk composition. In this sense, the study of orbital dynamics mechanisms through which the system can lose angular momentum is critical for understanding the type of the Moon-forming giant impact.

The evection resonance was taken by Cuk and Stewart (2012) as the mechanism to drain angular momentum from the system. The evection resonance was first briefly suggested by Yoder in private communication (1976) with Peale and Cassen (1978), but simply dismissed by them because they accepted the capture hypothesis for the lunar origin and in addition this resonance can only occur when the Moon is close to the Earth (4.3-6.3 Earth radii), which is not allowed by the capture hypothesis. Touma and Wisdom (1998) explicitly described the resonance and developed a simplified model that nicely describes the system's behavior in the resonance. In simple words, this resonance occurs when the motion of the lunar orbit's pericenter is "resonant" with the Sun's motion around the Earth, both with the period being 1 year. The angle between the direction to the Sun from Earth and the direction to the lunar orbit's pericenter (the evection

angle, σ in Fig. 3) stays near a constant value of ±½π. The most prominent phenomenon of the resonance is the strongly elevated lunar orbital eccentricities (to 0.2, 0.3, and higher). The semi-major axis decreases, and the Earth despins, therefore the system's angular momentum decreases.

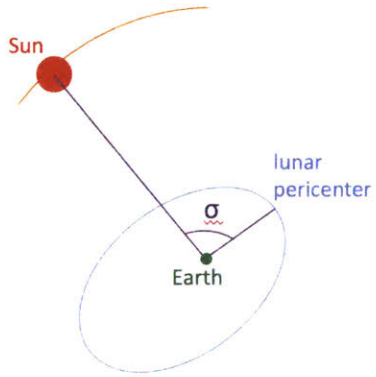

Fig. 3. The definition of the evection angle, σ.

However, Wisdom and Tian (2015) pointed out that the evection resonance is not a likely to have drained the angular momentum. This is simply because the severe tidal heating as a result of the high eccentricities over long periods of time reported by Cuk and Stewart (2012) would be so strong as to have vaporized the Moon.

In chapter 2, we propose an alternative orbital mechanism that can reduce the Earth-Moon system's angular momentum. This mechanism is related to the evection resonance, but is a limit cycle instead of a resonance. When the system is in the limit cycle, the evection angle circulates from 0 to 2π, and the eccentricity vibrates between a lower bound and an upper bound (Fig. 4), with a period the same as that for the circulation of the evection angle. With Q_e set at 400, the limit cycle lasts for more than 500 thousand years, and drains the system's angular momentum to a value close to the current value.

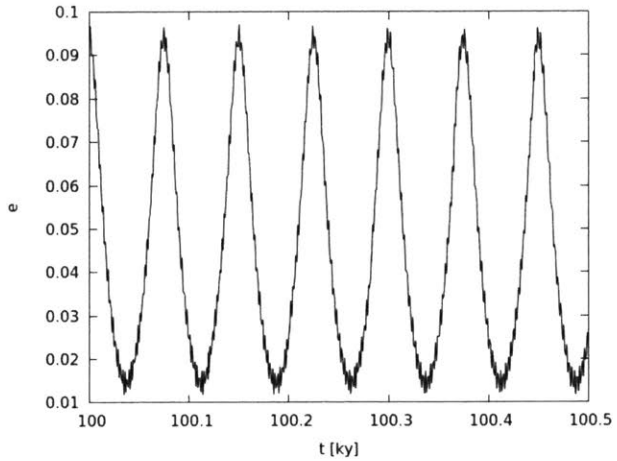

Fig. 4. The vibration of lunar orbital eccentricity in a typical limit cycle.

Compared with the evection resonance, the limit cycle raises the eccentricity only moderately. The lower and upper bounds of the eccentricity depend on the tidal parameters of the Earth and Moon (Q_e, Q_m, k_{2e}, k_{2m}), but for most cases the upper bound does not exceed 0.1. Therefore, the limit cycle does not cause severe tidal heating in the Moon and is expected to work more stably and robustly than the evection resonance.

Another advantage of the limit cycle is that it works over a much wider range of parameters than the evection resonance. This property not only makes the limit cycle a more probable mechanism to have drained the excessive angular momentum, but also keeps the limit cycle mechanism more robust to changes in disturbances and temporal changes in the Earth and Moon's thermal states and tidal properties.

In chapter 3, we couple the orbital evolution with the lunar magma ocean evolution to investigate the mutual effects of the orbital mechanisms and the Moon's thermal state on each other. Since the crystallization of the lunar magma ocean before the formation of a conductive plagioclase lid only takes several thousand years (Elkins-Tanton *et al.*, 2011), we start the magma ocean with a plagioclase lid of 5 km in thickness. In addition to the orbital processes, we also evolve the magma ocean liquid's volume, the thickness, temperatures and tidal properties of the lid. We simulate thermal conduction, tidal heating, partial melting and melt migration in the lid. The orbital system evolution affects the magma ocean processes by updating the lunar orbital

semimajor axis and eccentricity, which determine the tidal heating rate in the lid. The lunar magma ocean processes affect the orbital evolution by changing the Moon's tidal properties, which determine the orbital accelerations related with the lunar tidal deformation.

With the two systems coupled, we find that the evection resonance is unstable and does not reduce the system's angular momentum. When the system is captured in the evection resonance, the rapid increase in eccentricity causes violent changes in the Moon's tidal properties and soon brings the system out of the parameter range of the resonance. So the system exits the resonance shortly after it gets into the resonance, and the angular momentum loss is negligible.

In contrast, the limit cycle works robustly to drain the system's angular momentum as much as in the non-thermally coupled model. This is mainly because the moderate increases in eccentricity enhance tidal heating in the lid only mildly and slowly, and the changes in the lunar tidal properties are much smaller and more gradual than in the evection resonance. In addition, the wide parameter range for the occurrence and maintenance of the limit cycle also helps to guarantee that the changes in lunar tidal properties do not easily bring the system out of the limit cycle.

Therefore, we conclude that the limit cycle is the most viable mechanism to have drained the Earth-Moon system's excess angular momentum if the Earth started spinning fast.

4

Why is the "man in the Moon" on the lunar nearside? Did tidal heating play a role in determining its location?

The Moon exhibits a hemispheric asymmetry in the distribution of mare basalts. The overwhelming majority of the volume of the maria is on the lunar nearside. At first glance, it appeared that the mare basalts occur at the topographically low regions (e.g. Kaula, 1974). However, after the acquisition of the global topographic data (Zuber *et al.*, 1994; Smith *et al.*,

2016), it is recognized that many topographically low regions, most noticeably the South Pole-Aitken basin, do not contain abundant basalt emplacements. It is then more likely that the asymmetric distribution of maria indicates a fundamental asymmetry in lunar mantle activity. The nearside mantle has experienced relatively elevated partial melting during the lunar history, expressed in the form of mare distribution on the surface. Then why is this asymmetry hemispheric in scale, and why is the melting activity centered on the nearside?

Previous models (Hess & Parmentier, 1995, Zhong *et al.*, 2000) proposed scenarios to explain the formation of spherical harmonic degree-1 pattern of the mare asymmetry. At the end of the lunar magma ocean solidification, the dense ilmenite ($FeTiO_3$)-rich cumulates (IC), which are the last cumulates in the crystallization sequence, lie beneath the latest liquids that are highly concentrated in heat-producing elements (urKREEP). The IC layer, together with the iron rich mafic cumulates, overlie the magnesium rich, first crystallized minerals which are then at the base of the mantle. This gravitationally unstable density profile soon leads to a large-scale overturn in the mantle, bringing the IC and the iron rich silicates to the bottom of the mantle. Some of the late stage, radioactive element rich liquid is entrained with the IC and also sinks. Then the mixed ilmenite cumulates (MIC) either form a lunar core or a dense, radioactive element rich layer surrounding the core. According to Rayleigh-Taylor instability analysis, the overturn occurs rapidly, on the order of several thousand years.

As a result of this global-scale overturn, a substantial fraction of the Moon's heat-producing elements is concentrated in the deepest regions of the lunar mantle. As time proceeds, radiogenic heat accumulates in or around the core, and the outward thermal conduction is slow due to the great depth. The growing temperature and the resulting gravitational buoyancy of the MIC finally drives its ascent through the mantle to relatively shallow depths. Decompression melting of the ascending MIC creates the mare volcanism in 200~600 My. In this scenario, a single, large diapir is likely, since the spherical harmonic degree-1 pattern has the most rapidly growing instability under a wide range of parameter space, as given by both Rayleigh-Taylor instability analysis and numerical simulations (Hess & Parmentier, 1995, Zhong *et al.*, 2000). Therefore, the hemispheric asymmetry of the mare basalt distribution can be simply the result of spherical harmonic degree-1 diapir ascension of the deep MIC, radioactive element rich material.

However, the second question remains not completely answered. Why did the diapir rise in the nearside of the lunar mantle? Laneuville *et al.* (2013) proposed that the concentration of mare volcanism on the nearside of the Moon could be a natural consequence of the mantle thermal evolution, provided that the Moon's bulk KREEPy material is concentrated in the nearside crust and upper mantle in the first place. However, they did not provide an explanation for the concentration of the KREEPy material.

In chapter 4, we explore the feasibility of laterally heterogeneous tidal heating leading to the ascending diapir's occurrence in the nearside mantle. We expect the possibility that tidal deformation preferentially dissipates energy in the nearside mantle, raises the mantle temperatures, reduces the viscosity, and thus facilitates the mantle flow and diapir ascension.

We follow Peale and Cassen's (1978) approach for analyzing the distribution of tidal heating in a spherical body with a solid exterior layer overlying a liquid interior. We re-derive the formalism, correct errors, and extend the analysis to include both degree-2 and degree-3 tidal heating. We find that the pattern of degree-2 tidal heating does not preferentially heat the mantle regions on the Earth-Moon line in any case. For the degree-3 case, even though the mantle regions on the Earth-Moon line get the most tidally heated in some cases, the magnitude of heating is too small to have any effect when compared with the degree-2 heating.

We conclude that either tidal heating does not play a role in determining the location of the diapir ascension, or the spherically symmetric model's deformation scheme is not applicable to the Moon.

Chapter 1

Magnetic field modeling for Mercury using dynamo models with a stable layer and laterally variable heat flux

ZhenLiang Tian, Maria T. Zuber, Sabine Stanley

Abstract

Mercury's surface magnetic field is unique among planetary magnetic fields for its weak intensity, spin-aligned axisymmetry, and large dipole offset. An Earth-like dynamo setup applied to Mercury does not reproduce these features. Here we explain the magnetic field observations by a combination of two effects: (1) a stably stratified layer at the top of the outer core, and (2) a degree-1 north-south asymmetric spherical harmonic heat flux variation at the core-mantle boundary (CMB). We vary the stable layer thickness and size of the inner core, and find models that can produce surface magnetic fields possessing the observed features of Mercury.

Introduction

Mercury's magnetic field is a weak, offset dipole-dominated, spin-aligned axisymmetric field (Anderson *et al.*, 2011, 2012; Winslow *et al.*, 2014). It is unique among all active dynamo-generated magnetic fields in the solar system because of the following combination of properties:
(A) its magnetic moment is as weak as $\sim 190\text{nT}\cdot r_{planet}^3$, less than 1/100 that of the Earth (Anderson *et al.*, 2012);
(B) its dipole axis is aligned with Mercury's rotation axis to within 0.8° (Anderson *et al.*, 2012). In a Gauss expansion of the magnetic field, this fact corresponds to small g_{11}/g_{10} and h_{11}/g_{10} ratios, where g_{lm} and h_{lm} correspond to the degree-l, order-m Gauss coefficients.
(C) its dipole offset, which is the distance between the magnetic dipole equator and Mercury's geographic equator, is ~480 km ($0.2*r_{planet}$). This offset corresponds to $g_{20}/g_{10} = 0.40$ at the planetary surface.

According to magnetostrophic balance and energetics arguments, and assuming an Earth-like partitioning of the core magnetic field between poloidal and toroidal components, Mercury's dipole moment is expected to be in the range 4×10^3 - 4×10^6 nT$\cdot r_{planet}^3$ (Stanley & Glatzmaier, 2010). The observed weak field intensity alone poses a challenge to conventional Earth-like dynamo models.

Mercury's magnetic field is also anomalous for its morphology. Among axial dipole-dominated planetary magnetic fields, which include the magnetic fields of Mercury, Earth, Jupiter, Saturn and Ganymede, only Mercury and Saturn have confirmed dipole tilts less than 1° from the rotation axis (present data for Ganymede only provides an upper limit of 4° on the dipole tilt) (Smith *et al.*, 1980; Kivelson *et al.*, 2002; Anderson *et al.*, 2012). Saturn, however, has a dipole offset of $0.04\cdot r_{Saturn}$ (Smith *et al.*, 1980), which is much smaller than Mercury in the ratio to the planetary radius.

Prior to the MESSENGER spacecraft's measurements of the dipole tilt and offset of Mercury's magnetic field, several analytic and numerical studies tried to explain the weak intensity of the magnetic field: (**1**) A thermoelectric dynamo was proposed (Stevenson, 1987; Giampieri & Balogh, 2002) in which thermoelectric currents are driven by temperature differences on an irregular CMB. These currents would produce a toroidal magnetic field, and the helical motions in the fluid outer core would interact with the toroidal field to produce a weak poloidal field observable at Mercury's surface (10^2-10^3nT). (**2**) Stanley *et al.* (2005) used a thin shell dynamo model, in which fluid convection mainly operates outside the cylinder tangent to a very large inner core, to generate a non-Earth-like field partitioning between toroidal and poloidal components in the core. The core magnetic field is strong, but is dominated by toroidal components that do not penetrate outside the core, thus producing a weak surface field (10^3nT). Takahashi and Matsushima (2006) also used a thin shell geometry of outer core, and produced core magnetic fields that are dominated by high degree, multipole components which decrease to much lower intensities than the dipole on Mercury's surface. The surface magnetic field can be as small as 10^3nT. However, their model requires the inner core to be electrically insulating. Heimpel *et al.* (2005) investigated a very thick shell dynamo, which results in single-plume convection in the shell and produced relatively weak poloidal magnetic fields (10^4nT at

Mercury's surface). (**3**) The Vilim *et al.* (2010) model involves dissolution of Fe from S at some depth in the outer core, which results in two dynamo regions (the region above that depth, and the region below it) that can produce magnetic fields with opposite signs, thus weakening the observable surface magnetic field (160-1500nT). (**4**) Several studies (Glassmeier & Auster, 2007; Gomez-Perez & Solomon, 2010; Heyner *et al.*, 2010; Heyner *et al.*, 2011) investigated the feedback dynamo, in which there is a negative feedback between the dynamo-generated magnetic field and the magnetic field generated by the magnetospheric currents, where the magnetosphric currents result from the interaction between the internal planetary magnetic field and the solar wind. Mercury's magnetopause is close to the planet's surface as the weak dipole field is unable to push it farther away from the surface. This closeness of the magnetopause to the surface facilitates the magnetospheric field's substantial contribution to the overall field in Mercury's interior. The magnetospheric field is intrinsically anti-parallel to the internal dynamo field at the CMB, and lowers the saturation level of dynamo action in the core, therefore weakening the overall field in the core as well as on Mercury's surface (60nT in Heyner *et al.*, 2011, for example).

These dynamo models usually evoke some special geometry of the core dynamo region, and produce surface magnetic fields comparable in intensity to the observed magnetic field of Mercury. However, none of these models predict a surface magnetic field that is dominated by a highly axisymmetric and offset dipole.

It is difficult to generate a magnetic field that displays simultaneously a very small dipole tilt and a large dipole offset, *i.e.*, a field with both a large g_{20} and small g_{11} and h_{11}. This is because the g_{20} (axial quadrupole) and g_{11} and h_{11} (equatorial dipole) components belong to the same dynamo symmetry family (degree+order = even number). When fluid flows strongly excite one mode in the family, they typically excite other modes of similar wavelength in the same family (Bullard and Gellman, 1954). To numerically generate a magnetic field with these features, modifications to conventional dynamo models are needed.

To explain the weak intensity and axisymmetry of Saturn's magnetic field, Stevenson (1980,1982) proposed a structure that featured a stably stratified layer with differential rotation

at the top of the dynamo source region. The presence of the stable layer weakens the surface magnetic field by: (1) limiting the dynamo generation region to the deeper parts of the metallic H and He layer; and (2) attenuating the magnetic field, especially the rapidly varying, high multipole components, by the skin effect when the dynamo field passes through the stable layer. This stable layer, with differential rotation within it, can also act to "axisymmetrize" the surface magnetic field. Stevenson (1982) analytically determined that axisymmetrization should occur if the magnetic Reynolds number of dynamo action is sufficiently large. For Saturn, whose magnetic field is produced by the dynamo operating in the metallic hydrogen region, the stratified layer can be produced as helium rains out of the metallic hydrogen region of Saturn due to helium's immiscibility in metallic hydrogen in the molecular-metallic hydrogen transition region.
Later kinematic dynamo studies (Love, 2000; Schubert *et al.*, 2004) examined the effect of a stable layer surrounding the dynamo generation region in axisymmetrizing the magnetic field. These models prescribe the fluid flow in the stable layer, neglect the effects of the Lorentz force on the fluid flow and the interactions between the stable and unstable layers, and track the evolution of the magnetic field. Results showed that the stable layer can affect the symmetry of the surface magnetic field, but the magnetic field need not attain axisymmetry. The symmetry of the resulting magnetic field depends on the prescribed flows in the stable layer and the geometry of the magnetic field within the region of dynamo generation.

Recent dynamic dynamo studies (Christensen, 2006; Christensen & Wicht, 2008; Stanley & Mohammadi, 2008) investigated the role of a stable layer, without latitudinally variable thermal boundary conditions, in determining the geometry of the surface magnetic field. Christensen and Wicht (2008) incorporated a very thick, stably stratified layer surrounding the dynamo region, and found that a weak, axisymmetric field can be achieved for certain parameter regimes. However, they did not typically produce the combination of a small dipole tilt and a large dipole offset. Stanley and Mohammadi (2008) instead looked at the effects of thin stable layers. They found that a thin, stably stratified layer surrounding the dynamo region, by itself, does not act to axisymmetrize the surface magnetic field. Some patterns of zonal flows in the stable layer may disrupt the dynamo action through interaction between the stable and unstable layers.
For the case of Saturn, Stanley (2010) further investigated how a thin, stably stratified layer can affect the magnetic field with latitudinal heat flux variations (spherical harmonic degrees 2 and

3) imposed at its outer boundary. She discovered that only a stable layer with heat flux variations of certain patterns and signs can axisymmetrize the magnetic field. With a standard dynamo model, which has no stable layer or laterally variable thermal boundary conditions, thermal winds in the dynamo region can arise as a natural result of fluid convection. For the case of Saturn, when the thermal boundary condition (spherical harmonic degree-2) is applied at the top of the stable layer, the resultant thermal winds in the stable layer are in the same direction as those that would naturally arise from convection in the unstable layer. In this situation, the differential rotation in the stable layer shears out the non-axisymmetric components of the magnetic field in the dynamo region and produces an axisymmetric surface magnetic field. However, when the applied thermal boundary condition is of the opposite sign, or an octupole mode (spherical harmonic degree-3), the thermal winds produced in the stable layer would act to destabilize the flows in the dynamo region through interactions between stable and unstable layers, therefore producing more non-axisymmetric magnetic fields at the planetary surface. This study demonstrates the importance of the direction and equatorial symmetry of differential rotation in the stable layer in axisymmetrizing the surface field.

For Mercury, a stably stratified layer can also form at the top of the outer core, and a latitudinally heterogeneous heat flux is likely to be present at the top of this stable layer. The stable layer can form as a result of thermal and chemical stratification. According to thermal evolution models (for example, Hauck *et al.*, 2004), the heat flux at the CMB of Mercury is subadiabatic, which contributes to thermal stratification near the CMB. In addition, the high sulfur abundance and relatively low Fe content on the surface of Mercury (Nittler *et al.*, 2011) indicate a chemically reducing environment during Mercury's formation, which favors an enrichment of sulfur and silicon in the core. Earth-based (Margot *et al.*, 2007) and MESSENGER-derived (Smith *et al.*, 2012) geophysical measurements initially required the presence of a solid FeS-rich layer at the top of the outer core (Smith *et al.*, 2012) to explain the planet's radial density distribution. Subsequent refinement of the obliquity measurement (Margot *et al.*, 2012) dictates that this layer is still consistent with the observations but is no longer required (Hauck *et al.*, 2013). The presence of a solid FeS layer naturally requires an FeS-rich liquid layer to exist below it, which forms a stably stratified layer in the liquid core region.

Lateral variations in temperature within the mantle above the CMB are likely to occur in planets due to the pattern of mantle convection, the heterogeneous distribution of heat-producing elements in the mantle, or the effect of giant impacts. Stanley *et al.* (2008) applied a degree-1 spherical harmonic heat flux distribution at Mars' CMB to produce a single-hemisphere dynamo for ancient Mars that could account for the concentration of the planet's remanent crustal magnetic field in the southern hemisphere. For Mars, the heterogeneous heat flux distribution at the CMB can be produced as the result of the giant impact creating the Borealis basin (Andrews-Hanna *et al.*, 2008), or as the result of a hemispheric-scale pattern of mantle convection. Lateral variations in temperature at the Earth's CMB are evidenced by seismic tomography (van der Hilst *et al.*, 2007). Unfortunately Mercury lacks seismic observations needed for tomographic mapping, however, geological features, such as large volcanic plains (Head *et al.*, 2011), can be used to infer potential patterns of temperature variations at least in the era of formation of those features. In a dynamo model for Mercury's magnetic field, Cao *et al.* (2014) applied spherical harmonic degree-2 and degree-4 heat flux variations at the CMB with the highest heat flow at the equator. They did not provide a justification for these conditions, though the surface boundary condition does have degree-2 structure due to latitude-dependent insolation (cf. Aharonson *et al.*, 2003). Along with volumetric buoyancy applied in the core, they produced magnetic fields with large dipole offsets, an average dipole tilt of 3° (personal correspondence), and a magnitude somewhat weaker than that scaled from an Earth-like dynamo field, but still much larger than Mercury's observed field.

In this study, we assume a degree-1 heat flux distribution at the CMB. A degree-1, laterally variable mantle heat flux distribution is plausible in ancient Mercury. A laterally variable thermal structure in the mantle is consistent with geological observations (Head *et al.*, 2011) of extensive volcanic flooding at the surface in Mercury's northern high latitudes between the late stages of the late heavy bombardment ~ 3.7 to 3.8 Ga ago. The widespread volcanism indicates more vigorous mantle convection and heat transport in the northern hemisphere. More rapid mantle heat transport can result in cooler temperatures near the CMB, and thus a higher heat flux across the CMB. Even though the northern volcanic plains only occupy 6% of Mercury's surface area, it is quasi-centered on the pole and the inferred spherical heterogeneity in heat flux can be roughly represented by a degree-1, order-0 spherical harmonic pattern. This assumes the area of volcanic

flooding corresponds to the regions of higher rates of mantle convection, instead of an entire hemisphere of positive variable heat flux of the degree-1 spherical harmonic pattern.
The heterogeneous distribution of mantle convection rates can be attributed to either variations in concentration of heat-producing elements in the mantle or heterogeneous distribution of mantle viscosity. Mapping of the surface distribution of radioactive elements (Peplowski *et al.*, 2012) reveals higher concentration of K in the surface tens of centimeters in the northern high latitudes compared to the equatorial regions. This was initially explained by a thermal redistribution mechanism, where K is transported from hotter equatorial regions to the cooler pole regions. But later findings of correlation of K and Mg/Si ratio distributions suggest that the surface K variations result from the compositions of the intrinsic crustal material (Weider *et al.*, 2015). Currently a global map of surface concentration of radioactive elements is unavailable due to the high eccentricity of the MESSENGER spacecraft's orbit around Mercury, so we are not sure whether the southern high latitude regions also have higher than average concentrations of heat producing radioactive elements. If moderately elevated abundances of heat-producing elements are present in surface rocks, and thus the mantle source regions in the northern high latitudes but not in the southern regions, the resultant higher mantle temperature in the north would favor a higher heat flux at the CMB in the north. Even though a somewhat hotter mantle in the northern high latitudes lowers the rate of thermal conduction, the higher temperature makes the material less viscous and therefore increases the likelihood or vigor of mantle convection.

The surface K abundance in the northern high latitudes is on average (over the longitudes) 2-3 times higher than in the equatorial regions (Peplowski *et al.*, 2012), and suggests only moderate concentration of heat-producing elements in the crust and mantle there. This is very different from the case of Procellarum KREEP terrane (PKT) on the Moon, which concentrates the dominant majority of the heat-producing elements of the Moon. In the latter case, the surface Th distribution suggests significantly raised mantle temperatures in the PKT region, which leads to a thermal blanket (Stegman *et al.*, 2003) that prevents efficient heat transfer from the core to the surface. For Mercury, the surface K abundance variation is much more limited in magnitude, and the implied slightly raised mantle temperatures in the northern high latitudes should have a more effective impact on heat transfer through enhancing mantle convection. This is especially the case when the average mantle is just near the critical point for convection to occur, *i.e.*, when

the occurrence and maintenance of mantle convection is most sensitive to slight changes in viscosity. Thermal evolution studies (for example, Michel *et al.*, 2013) suggest that at a mantle thickness of about 400 km, the mantle is just unstable enough to be in the convective state, and in some cases the convection does not persist to the present. Therefore, even moderately stronger internal heating in the mantle in the northern high latitudes would substantially promote convection there, resulting in either increased vigor of convection than other regions, or the persistence of convection to the present when convection in the southern regions has already ceased. In either case, since heat transport via convection tends to be more efficient than by the diffusive process in conduction, the overall rate of heat transport from the core to the planetary surface would be higher in the northern high latitudes than in the southern regions, thus creating a north-south asymmetric heat flux across the CMB, with the strong values the north.

The assumption of heterogeneous heat flux can be tested by future missions to Mercury that (1) map the surface concentration of heat-producing elements in the southern hemisphere, to produce a global map combined with MESSENGER data in the northern hemisphere; and (2) measure the latitudinal variation of surface heat flux.

In this study, we carry out numerical dynamo simulations that feature an outer stratified layer in the core and a degree-1 heat flux at the CMB.

Model & Method

The essential mechanism of dynamo generation is the coupling of hydrodynamic and electromagnetic processes in a region of electrically-conductive fluid, which models the evolution of the magnetic, temperature and flow velocity fields. Our Boussinesq dynamo model is governed by the non-dimensional equations for:

magnetic induction

$$(\partial/\partial t - \nabla^2)\boldsymbol{B} = \boldsymbol{\nabla}\times(\boldsymbol{v}\times\boldsymbol{B}), \quad (1)$$

the non-existence of magnetic monopoles

$$\nabla\times\boldsymbol{B} = 0, \quad (2)$$

fluid flow (Navier-Stokes)

$$Ro_m \left(\partial/\partial t + \boldsymbol{v}\cdot\boldsymbol{\nabla}\right)\boldsymbol{v} + \boldsymbol{z}\times\boldsymbol{v} = Ra(1-r_{io})^{-2}\,\Theta\,\boldsymbol{r} + \boldsymbol{j}\times\boldsymbol{B} + E_k\,(1-r_{io})^2\,\nabla^2\boldsymbol{v} - \boldsymbol{\nabla}p, \qquad (3)$$

continuity in the Boussinesq approximation

$$\nabla\cdot\boldsymbol{v} = 0, \qquad (4)$$

and energy

$$\left(\partial/\partial t - q_k\nabla^2\right)\Theta = -\boldsymbol{v}\cdot\boldsymbol{\nabla}\left(T_0(r) + \Theta\right). \qquad (5)$$

In these expressions, $\boldsymbol{B}$ is the magnetic field, $\boldsymbol{v}$ is the flow velocity field, Θ is the superadiabatic temperature perturbation field (the difference between the total superadiabatic temperature field and $T_0(r)$, the conductive temperature solution), $\boldsymbol{j}$ is the electrical current density, p is the fluid pressure, and r_{io} is the ratio of the radii of the inner core to the outer core.

In the non-dimensionalization of these equations, r_o (the outer core radius) is used as the length scale, $\tau = r_o^2/\eta$, (the magnetic diffusion time, where η is the magnetic diffusivity) is used as the time scale, $B_{scale} = \mathrm{sqrt}(2\Omega\rho/\sigma)$ (the magnetostrophic balance value, where Ω is the rotation rate of the planet, ρ is the fluid density, and σ is the fluid's electrical conductivity) is used as the magnetic field scale, $T_{scale} = h_T r_o$ (where h_T is the negative of temperature gradient at inner core boundary) is used as the temperature scale. Assuming $\eta = 0.6$ m^2/s (or $\sigma = 1.3\times10^6$ S/m) (Pozzo *et al.*, 2012), the magnetic diffusion time would be $\tau = r_o^2/\eta \cong 2.1\times10^5$ years.

In the expressions above:

$Ro_m = \eta/(2\Omega r_o^2)$ is the magnetic Rossby number, the ratio of the inertia force to the Coriolis force;

$E_k = \nu/(2\Omega r_o^2)$ is the Ekman number, the ratio of the viscous force and the Coriolis force, where ν is the fluid's kinematic viscosity;

$q_k = \kappa/\eta$ is the Roberts number, the ratio of thermal diffusivity (κ) to magnetic diffusivity; and

$Ra = \alpha g_0 h_T r_o^2/(2\Omega\eta)$ (α is the thermal expansion coefficient of the fluid) is the modified Rayleigh number, a measure of the driving buoyancy force.

Our numerical scheme for dynamo simulations is based on the model of Kuang & Bloxham (1999) with the following modifications:

1) We pose a stably stratified layer in the upper region of Mercury's outer core (Fig. 1). This stratification may result from a subadiabatic heat flow at the CMB of Mercury. Christensen (2006) and Christensen and Wicht (2008) have shown that dynamo models with an outer stably

stratified layer can result in weak surface magnetic fields.

2) We implement fixed laterally heterogeneous heat flux boundary conditions at the CMB. This results in thermal winds in the stably stratified layer that can act to modify the field toward axisymmetry, as demonstrated by Stanley (2010).

We use viscous stress-free, non-penetrative boundary conditions on the velocity field and a freely rotating, finite conducting inner core with the same conductivity as the fluid outer core.

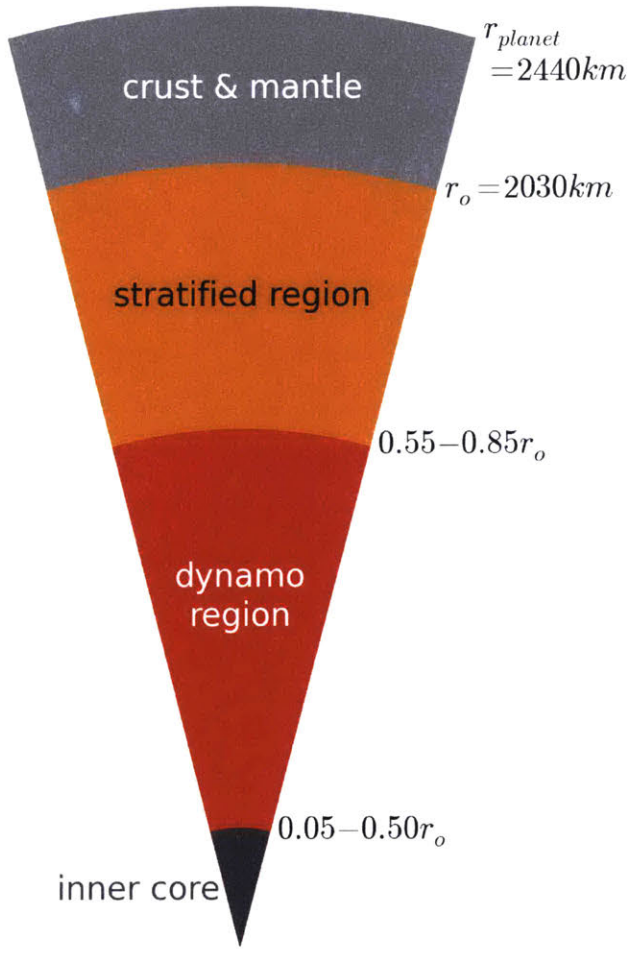

Fig. 1. Internal structure model of Mercury used in the numerical simulations. Sizes of regions are not to scale.

The model has 36 radial grid points in the solid inner core and 64 radial grid points in the fluid outer core. The spherical harmonics in the longitudinal and latitudinal directions reach a

maximum degree of 33 and maximum order of 21. We employ a very weak hyperdiffusion starting at spherical harmonic degree 20 of the form:

$\nu_t(l) = \nu_0 \, (1 + a(l - l_0)^n)/(1 + a(l_1 - l_0)^n)$ for $l > l_0$,

where ν_t represents either the kinematic, magnetic or thermal diffusivity, ν_0 refers to the constant value for $l < 20$, $l_0 = 20$, $l_1 = 20$, $n = 2$ and $a = 0.05$ for the kinematic diffusivity, and $a = 0.06$ for the magnetic and thermal diffusivities. Dharmaraj *et al.* (2014) demonstrated that such a hyperdiffusion does not significantly affect the solutions. Grote *et al.* (2000) and Zhang & Jones (1997) suggest that the use of hyperdiffusion leads to suspect results in dynamo models. However, these models use much stronger hyperdiffusion than our model. For example, Grote, Busse & Tilgner (2000) uses: $a = 0.075$, $l_0 = 0$, $l_1 = 4$, $n = 3$, while we use $a = 0.05$, $l_0 = 20$, $l_1 = 20$, $n = 2$ in this study. The values of viscosity as a function of spherical harmonic degree for several models are shown in the Fig. 2. It is clear that the Kuang & Bloxham (1999) and the current study have much weaker hyperdiffusion than the Grote *et al.* study. Furthur tests for a range of hyperdiffusion values suggest that our use of hyperdiffusion does not notably affect the large scale fields in this model.

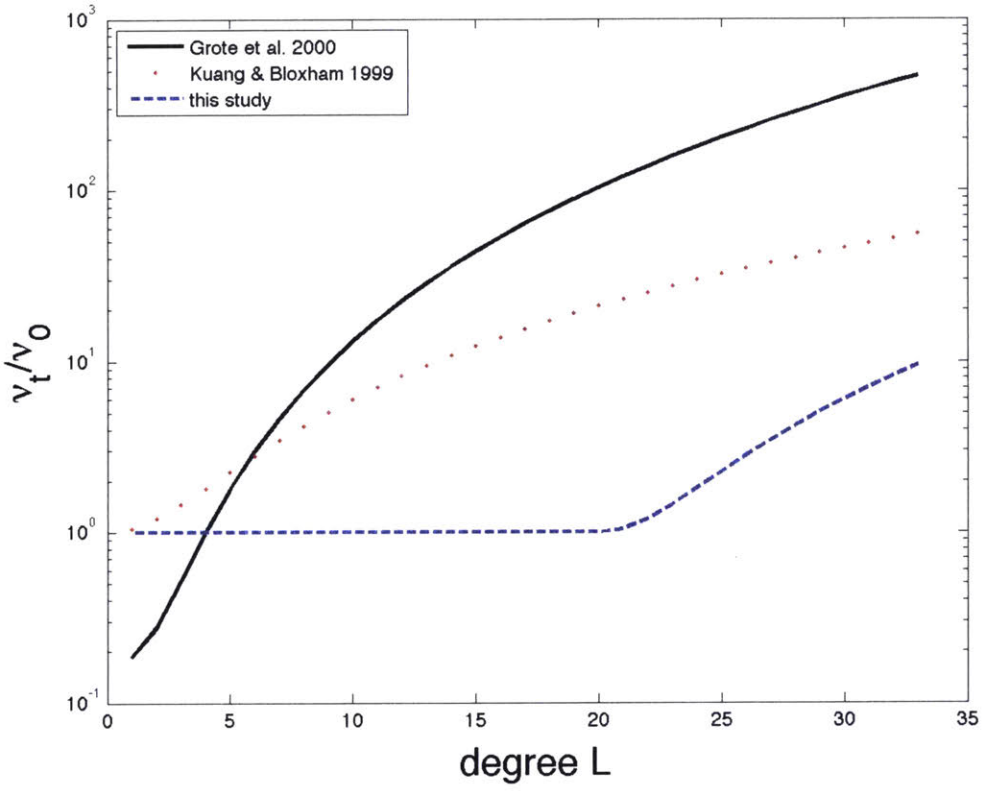

Fig. 2. Comparison of the values of viscosity as a function of spherical harmonic degree for Grote *et al.* (2000) model, Kuang & Bloxham (1999) model, and the model used in this study.

We investigate a plausible range of inner core sizes and stratified layer thicknesses. The inner core radius ranges from 5% to 50% of the core radius, and the thickness of the stratified layer ranges from 15% to 45% of the core radius. The stable stratification is implemented in our Boussinesq model via a co-density formalism similar in manner to previous work, where the background temperature profile is given a stable conductive profile (Stanley & Bloxham, 2004, 2006; Stanley & Mohammadi, 2008; Stanley, 2010). It is specified by a non-dimensional background co-density gradient dC_0/dr. Those cases producing average dipole tilts less than 5° are listed in Table 1. We apply a degree-1 spherical harmonic variable heat flux. In Table 1, variable heat flux is defined in terms of the ratio of the root mean square of perturbations in CMB heat flux to F_{mean}, the mean superadiabatic heat flux. $F_{mean} = \kappa h_T r_{io}^2$, where κ is the thermal conductivity.

Table 1. Inner core sizes, stable layer thicknesses (d_{stable}) and background co-density gradient (dC_0/dr), variable heat flux, and the resultant surface magnetic fields' g_{10}, dipole tilts, and offsets of the models that produce average dipole tilts less than 5°. Core radius (r_o) is 2030 km, the magnetic Rossby number (Ro_m) is 2×10^{-5}, the Ekman number (E_k) is 2×10^{-5}, and the modified Rayleigh number (Ra) is 5000.

Model number	r_{io}	d_{stable}/r_o	dC_0/dr	Variable heat flux	Avg. g_{10} (nT)	Avg. tilt (°)	Avg. offset (r_{planet})
1	0.05	0.30	1	0.127	194	0.58	0.08
2	0.10	0.35	1	0.084	97	0.53	0.17
3	0.10	0.30	1	0.070	198	1.34	0.17
4	0.15	0.40	1	0.070	515	0.70	0.21
5	0.15	0.35	2	0.070	236	0.51	0.17
6	0.20	0.45	1	0.084	79	0.59	0.22
7	0.20	0.40	1	0.084	249	1.30	0.20
8	0.20	0.35	3	0.141	124	2.96	0.23
9	0.30	0.35	5	0.141	284	2.51	0.12

Results

Results that have average dipole tilts less than 5° are summarized in Table 1. Assuming a degree-1, latitudinally varing heat flux at the CMB, and a range of inner core sizes and stable layer thicknesses, we obtain stable solutions for which the surface magnetic fields are weak, highly axisymmetric about the spin axis, and with a large dipole offset. An example is shown in Fig. 3. Fig. 3 shows the field analyses for a dynamo case whose inner core radius is 0.15 r_{CMB}, and whose stably stratified layer is between 0.65-1.0 r_{CMB} (model number 5). For most of the time, the planetary magnetic moment is about 200-300nT·r_{planet}^3, which is of similar magnitude as Mercury's observed value of 190nT·r_{planet}^3. The tilt of the dipole axis from the spin axis is mostly less than 1°, and the dipole offset of 0.17·r_{planet} agrees well with the observed value of 0.2·r_{planet}. In comparison, a dynamo case with the same stable layer but a homogeneous heat flux at the CMB typically produce magnetic fields with dipole tilts too large to match the observations, though sometimes with a weak field intensity at the surface.

For the magnetic field below the stably stratified layer, the strongest positive values are mostly distributed around the north pole, creating a strong low degree spherical harmonic component. Even though the strongest negative value is even larger than the strongest positive value in

absolute value, these strong negative values are in small-scale flux spots near the equator, and only contribute to higher degree multipole components, which are attenuated through the stable layer. The magnetic field below the stable layer already exhibits the north-south asymmetry, with stronger fields in the northern hemisphere. The stably stratified layer preferentially weakens the rapidly varying high degree components by the skin effect as the magnetic field diffuses through it, creating a dipole- and quadrupole-dominated magnetic field at the top of the stratified layer. The weak strength of the surface field is partly due to the size of stable layer that limits the dynamo region within 0.65 r_{CMB}. But since Mercury's core is so huge (r_{CMB} = 2030km, r_{planet} = 2440km), the weak strength is mainly attributed to the stable layer's skin effect.

Fluid velocity field plots show substantial differential rotation in the stratified layer. As predicted by Stevenson (1980), the differential rotation plays a major role in twisting the non-axisymmetric components of the magnetic field in the dynamo and producing a more axisymmetric surface field.

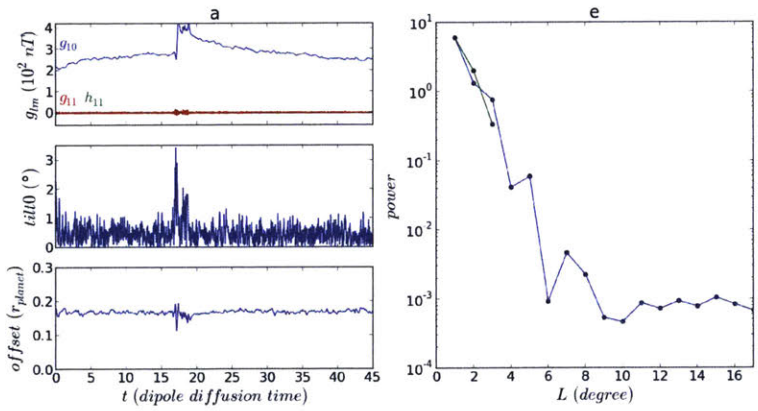
a
g_{lm} (10^2 nT)
g_{10}
g_{11} h_{11}
tilt0 (°)
offset (r_{planet})
t (dipole diffusion time)
e
power
L (degree)

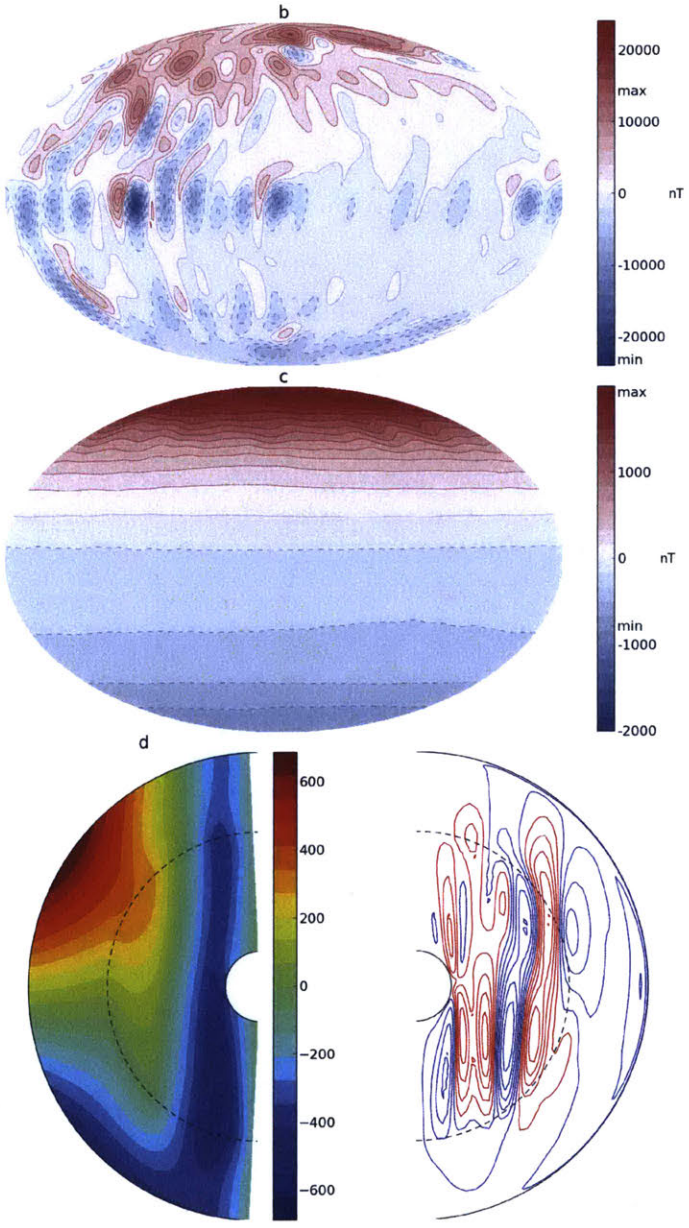
b
20000
max
10000
0
nT
-10000
-20000
min
c
max
1000
0
nT
min
-1000
-2000
d
600
400
200
0
−200
−400
−600

Fig. 3. (a) Surface field diagnostics, (b) radial component of magnetic field just below the stratified layer, (c) radial component of magnetic field at the top of the stratified layer, (d) fluid flow field, and (e) power spectrum, or Mauersberger-Lowes spectrum, as computed by $(l+1)(r_{planet}/r)^{2l+4}\Sigma_{m=0:l}(g_{lm}^2 + h_{lm}^2)$ at the CMB, for model number 5. In (a), the upper plot shows the g_{10}, g_{11}, h_{11} coefficients vs. time, the middle plot shows the angle between dipole axis and spin axis vs. time, and the lower plot shows the dipole offset vs. time. In (d), the left plot shows the longitudinally averaged toroidal flow in non-dimensional units, while the right plot shows contours of poloidal flow, in which red denotes counter-clockwise motion, and blue denotes clockwise motion. The dashed lines denote the boundary between stably stratified and unstable layers. In (e), the blue line denotes the power spectrum of the modeled magnetic field, and the green line denotes the observed values by the MESSENGER team (Anderson *et al.*, 2012). Both data are non-dimensionalized such that their respective dipole moment is $1 \cdot r_{planet}^3$.

Implications

Our results show that a mechanically stratified layer at the top of the liquid core can play an important role in producing a spin-aligned, dipole-dominated surface magnetic field with a large dipole offset to the equator. This conclusion is consistent with the results of thermal evolution modeling that the thermal gradient at the CMB is subadiabatic, which can lead to stable stratification at the CMB (Christensen, 2006). The emergence of a stratified layer can also be attributed to chemical stratification of liquid FeS at the top of the outer core. A solid FeS layer, which must overlie an FeS-rich liquid layer, was once thought to be required (Smith *et al.*, 2012) to explain Mercury's observed geophysical parameters (Margot *et al.*, 2007; Smith *et al.*, 2012). More recently, the refinement of Mercury's obliquity (Margot *et al.*, 2012) dictates that the existence of a solid FeS layer is still possible but not required (Margot *et al.*, 2012; Hauck *et al.*, 2013). Our simulations provide additional motivation for considering the existence of such a solid layer, which can form above a stratified FeS-rich liquid layer. We note that the enrichment of light alloying elements, such as S and Si, in the core, is consistent with the observed high abundances of volatile S contents on Mercury's surface detected by the MESSENGER spacecraft (Nittler *et al.*, 2011). The mixture property of the FeS liquid in the high-temperature, high pressure Fe-Ni-S-Si system is complex. If FeS were immiscible with the Fe and Ni core liquids under certain conditions, a stably stratified layer of FeS rich liquid would form at the top of the core. It is unclear under what conditions will the precipitated FeS solids stay at the top of the core to form a solid FeS layer, instead of sinking down to join the inner core. In either case, the existence of an FeS enriched liquid layer helps to produce a Mercury-like surface magnetic field.

Cao *et al.* (2014) used an equatorially symmetric (degree-2 and 4) heat flux variation at the CMB and volumetric buoyancy in the core to model the large offset of Mercury's magnetic field. They produced surface magnetic fields with the strongest parts in the northern hemisphere. The dipole tilt of the surface magnetic field in their model is 3° on average and 6° at maximum (personal correspondence), somewhat larger than the observed value of less than 0.8°. They produced magnetic fields somewhat weaker than what an Earth-like dynamo would produce, with an Elsasser number of 3×10^{-2} at the CMB. Assuming the core's density to be 6.5×10^{3} kg·m^{-3} (Hauck *et al.*, 2013) and the core's electrical conductivity to be 1.3×10^{6} S/m (Pozzo *et al.*, 2012), this is equivalent to a magnetic field strength of 1.4×10^{4} nT at the CMB, still much larger than what the observed surface field strength of 190 nT would allow. In comparison, the degree-1 heat flux pattern in our model has evidence from the distribution of volcanic plains on Mercury, and our models are able to produce not only large dipole offsets, but also typical dipole tilts less than or near 1°, and a field magnitude comparable to the Mercury observations.

Conclusion

We can produce Mercury-like magnetic fields with dynamo models that feature a partially stratified core and a degree-1, spherical harmonic, laterally heterogeneous heat flux applied at the CMB. The stably stratified layer acts to both weaken the surface magnetic field by limiting the dynamo convection region to the deeper regions of the core, and to attenuate higher multipole components of the magnetic field through the skin effect. The degree-1 CMB heat flux gives rise to differential rotation in the stratified layer, which further drives the surface magnetic field towards axisymmetry by damping the non-axisymmetric components. The presence of a stratified layer at the top of the outer core is consistent with either thermal stratification given by thermal evolution models of Mercury, or chemical stratification of liquid FeS below an overlying solid FeS layer consistent with the high abundance of volatiles on the surface of Mercury as well as geophysical measurements of low-degree gravity, the obliquity of the spin axis and the amplitude of the forced physical libration.

Acknowledgements: This work was supported by the NASA MESSENGER mission, under contract to the Carnegie Institution of Washington and Lamont-Doherty Earth Observatory of Columbia University.

Chapter 2

Early evolution of the Earth-Moon system with a fast-spinning Earth

Jack Wisdom, ZhenLiang Tian

Abstract

The isotopic similarity of the Earth and Moon has motivated a recent investigation of the formation of the Moon with a fast-spinning Earth (Cuk and Stewart, 2012). Angular momentum was found to be drained from the system through a resonance between the Moon and Sun. They found a narrow range of parameters that gave results consistent with the current angular momentum of the Earth-Moon system. However, a tidal model was used that was described as approximating a constant Q tidal model, but it was not a constant Q model. Here we use a conventional constant Q tidal model to explore the process. We find that there is still a narrow range of parameters in which angular momentum is withdrawn from the system that corresponds roughly to the range found earlier, but the final angular momentum is too low to be consistent with the Earth-Moon system. Exploring a broader range of parameters we find a new phenomenon, not found in the earlier work, that extracts angular momentum from the Earth-Moon system over a broader range of parameters. The final angular momentum is more consistent with the actual angular momentum of the Earth-Moon system. We develop a simple model that exhibits the phenomenon.

Introduction

An isotopic crisis (Melosh, 2009) has inspired a recent scenario for the formation of the Moon (Cuk and Stewart, 2012). Prior research (Canup, 2004, 2008) into the giant impact scenario for the formation of the Moon has assumed that when the Moon was formed the Earth-Moon system was left with the present angular momentum. Indeed, this was thought to be a virtue of the model. However, in these simulations the Moon is predominantly formed from the impactor. Recent isotopic measurements have shown that the Moon and Earth have essentially identical isotopic composition for chromium (Lugmair and Shukolyukov, 1998), oxygen (Wiechert *et al.*,

2001), tungsten (Touboul *et al.*, 2007), titanium (Zhang *et al.*, 2012). Thus to explain the isotopic similarity of the Earth and Moon one has to appeal to an accidentally similar impactor, or to some sort of reequilibration of the isotopic signature after the impact but before the Moon formed (Pahlevan and Stevenson, 2007). But reequilibration of isotopes in the protolunar disk seems less likely because refractory isotopes have been found to be similar for the Earth and Moon. The similarity of the Earth and Moon suggests that the Moon forming impact was more severe than previously investigated and that the Moon formed from material derived directly from the Earth's mantle (Cuk and Stewart, 2012; Canup, 2012; Lock *et al.*, 2016). The enrichment of heavy potassium isotopes in the Moon (Wang and Jacobsen, 2016) also supports a high-energy, high-angular momentum giant impact. The problem is that such an impact would leave the Earth spinning much more rapidly than previously assumed and some mechanism of removing the excess angular momentum must be found.

One such mechanism was recently proposed by Cuk and Stewart (2012). In this scenario, the Moon is formed by a hard impact by a smaller and faster impactor than previously considered, excavating material that forms the Moon that is largely derived from Earth's mantle. The Moon is initially formed with low eccentricity just outside the Roche radius, and evolves outwards due to the action of tides on the Earth. As it evolves it is captured into a resonance between the Moon and the Sun where the period of precession of the lunar pericenter is one year. This resonance is called the evection resonance (see Touma and Wisdom, 1998). After the system is captured into the evection resonance the eccentricity of the lunar orbit rises dramatically. Due to the eccentricity damping effect of tides raised in the Moon (Goldreich, 1963), an equilibrium eccentricity is reached. In cases where the evection resonance is stable, angular momentum is drained from the system and deposited in the Earth-Moon system's orbital motion about the Sun. The rotation rate of the Earth slows and the semimajor axis of the lunar orbit decreases until the angular orbital motion near pericenter matches the rotation rate of the Earth, at which point the evection resonance becomes unstable (Touma and Wisdom, 1998) and the system escapes from resonance. The angular momentum of the Earth-Moon system is left with a value close to the present angular momentum.

However, the tidal model used by Cuk and Stewart (2012) was described as approximating a "constant Q" tidal model, but in fact it had little to do with a conventional constant Q tidal model. In this paper we show that when a conventional constant Q tidal model is used we can reproduce the basic phenomenon reported by Cuk and Stewart (2012), but too much angular momentum is lost. However, we have found an alternate scenario that can drain an appropriate amount of angular momentum from the system over a wide range of parameters.

Methods

The physical model and numerical methods that we use are similar to those used in Touma and Wisdom (1994, 1998), and also similar to those used by Cuk and Stewart (2012). One difference between our model and that of Cuk and Stewart is that we studied the rotation of the Moon (for reasons explained below); for Cuk and Stewart the Moon was a point mass.

Our numerical model integrates the orbital evolution of the Earth, Moon, and Sun. We integrate the full rotational dynamics of an axisymmetric Earth and a triaxial Moon, with spin-orbit coupling of Earth and Moon. We include tides in the Earth and Moon, using the constant-Q Darwin-Kaula model. We add intrinsic wobble damping following Peale (1977).

The symplectic mapping method of Wisdom (1991) forms the framework for our numerical model. In this method, the Hamiltonian is split into parts that are separately efficiently solvable; the complete evolution is obtained by interleaving the pieces. We think of the splitting in terms of the introduction of delta functions into the Hamiltonian. The n-body Hamiltonian is split into Kepler Hamiltonians plus the interaction Hamiltonian using hierarchical Jacobi coordinates (see Sussman and Wisdom, 2015). During the "drift" step we evolve both the Kepler motion and the free rigid body motion of the Earth and Moon. During the "kick" step the spin-orbit interactions are evaluated, and the tides are introduced by a tidal kick.
We actually developed two versions of our code. In one version the rotational configuration of each rigid body was specified by the rotation matrix that takes the body from its reference orientation to its actual orientation by an active rotation. In the other version we specified the rotational configuration by a quaternion (Sussman and Wisdom, 2015). The torques and

accelerations are given by the expressions in Touma and Wisdom (1993). In the first code we evolved the free rigid body during the drift step using the Lie-Poisson algorithm specified in Touma and Wisdom (1993); in the second code we numerically integrated the quaternion equations of motion for a free rigid body (Sussman and Wisdom, 2001). We found that the two codes gave good agreement.

A key difference between our study and that of Cuk and Stewart is the tidal model. Cuk and Stewart used a tidal model that they described as approximating a constant Q tide, but it was not a constant Q tidal model; we actually used the conventional constant Q tidal model.

The Cuk and Stewart (2012) tidal model is as follows. The tidal torque on the Earth is

$$\mathbf{T} = -\frac{T_0 S(\omega,\dot{f})}{\omega r^6}\mathbf{M}, \qquad (1)$$

where $S(\omega,\dot{f}) = (\omega - \dot{f})/\sqrt{\omega|\omega - \dot{f}|}$, and $T_0 = 1.95\times10^{-5}$ in units where Gm_e and R_e are unity. The quantity **M** is the vector angular momentum of the Earth, ω is the rotation rate of the Earth, r is the Earth-Moon distance, and f is the true anomaly of the Moon's orbit. The numerical value was chosen so that the rate of evolution corresponded to $Q_e = 100$. Before we go on let's criticize this expression. First, it is simply not the case that in any real tidal model the tidal torque is always aligned with the angular momentum vector. The tidal torque should involve the orbital elements (or the position and velocity) of the Moon, and the tidal torque need not be aligned with the angular momentum of the Earth. Second, the fact that the factor T_0 is given numerically, rather than being given in terms of parameters of the system, is indicative of the fact that this expression is not derived from more basic physical principles. Third, the origin of the factor S is not clear; its form seems to be completely arbitrary. Next, Cuk and Stewart state that "the acceleration of the Moon corresponds to a torque that is equal and opposite in sign." Since a torque is derived from a force by a cross product, and information is lost in performing a cross product, it is not possible to uniquely determine the acceleration from the torque. Cuk and Stewart took the tidal acceleration to be perpendicular to the radius vector to resolve the ambiguity. Again, in conventional tidal models it is not necessarily the case that the tidal acceleration is perpendicular to the radius vector. Finally, the acceleration of the Moon due to tides raised in the Moon is given by the expression

$$\ddot{\mathbf{r}} = -A_0 v_r r^{-13/2} \hat{\mathbf{r}}, \qquad (2)$$

where $A_0 = 2.7 \times 10^{-3}$ in the same units as before, and v_r is the radial component of the velocity. This has the virtue (and sole purpose) of damping the orbital eccentricity. It is not clear whether the eccentricity dependence of this tidal acceleration corresponds to any conventional tidal model. The factor A_0 is, again, not given in terms of physical parameters.

To illustrate these criticisms, consider the expressions for the popular constant Δt tide (see Touma and Wisdom, 1994, for a pedagogical introduction). In this tide (sometimes called the Mignard-Hut tide, Mignard, 1979, Hut, 1981), the response of the planet to the tide raising potential is a coherent tidal bulge that is delayed in time by a constant time interval Δt. The force on the Moon due to tides that it raises on the Earth is

$$\mathbf{F} = -3k_2 G m_m^2 R_e^5 r^{-10} \{r^2 \mathbf{r} + \Delta t[2\mathbf{r}(\mathbf{r} \cdot \mathbf{v}) + r^2(\mathbf{r} \times \boldsymbol{\omega} + \mathbf{v})]\}, \qquad (3)$$

and the torque on the Moon's orbit (opposite to the torque on the Earth's figure) is

$$\mathbf{T} = \mathbf{r} \times \mathbf{F} = -3k_2 G m_m^2 R_e^5 r^{-8} \Delta t[(\mathbf{r} \cdot \boldsymbol{\omega})\mathbf{r} - r^2 \boldsymbol{\omega} + \mathbf{r} \times \mathbf{v}], \qquad (4)$$

where $\mathbf{r}$ is the vector from the Earth to the Moon, $\mathbf{v}$ is the velocity of the Moon relative to the Earth, r is the magnitude of $\mathbf{r}$, and $\boldsymbol{\omega}$ is the angular velocity vector. Note that the coefficients are given in terms of physical parameters of the system; this reflects the fact that the expressions are derived from more basic physical principles. Note that there are three terms in the torque, only one of which is proportional to the angular momentum (spin) of the Earth. There are two other terms that involve the relative position and velocity of the Earth and Moon. The Cuk and Stewart torque is simply proportional to the angular momentum of the Earth. Note that the torque is derived from the force (acceleration) by performing a cross product of the radius vector with the force. The force is derived first. Cuk and Stewart reverse this: they evaluate the torque first and deduce the force from it with an extra assumption that the force is perpendicular to the radius. Of the four terms in the force, only one of them is perpendicular to the radius vector (the third). In the Cuk and Stewart tide the force is taken to be strictly perpendicular to the radius vector.

The constant Δt tide has the characteristics required of a real tidal model, but it does a poor job of fitting the Lunar Laser Ranging results (Williams *et al.*, 2005, 2014). Thus it is not a good tidal model for the Moon. The Mignard-Hut model is reported here because the expressions for it are simple and by comparison it illustrates deficiencies in the Cuk and Stewart tidal model.

We used a Darwin-Kaula constant Q model (Kaula, 1964). The Darwin-Kaula tidal model Fourier expands the tide raising potential and considers the response of the body on which tides are raised term by term. Each term in the tidal potential raises a tidal bulge and the corresponding exterior potential of that tidal bulge is proportional to the Love number k_l; we keep only the second degree l=2 terms. The response to each Fourier component is delayed in phase to take account of the dissipative nature of the tides. The Darwin-Kaula model is fully general in that it can represent the tidal response of a body with any rheology by incorporating the appropriate frequency dependence of the phase delays and the Love numbers.

But there is actually scant knowledge of the frequency dependence of the tidal response of planets and satellites. Indeed, only for the Moon is there any hint of the frequency dependence of the tidal response, and there the response is measured for only two frequencies. The result is a weak dependence on frequency (Williams *et al.*, 2005, 2014). According to these Lunar Laser Ranging (LLR) results, the lunar Q at one month is 30, and the lunar Q at one year is 34. The expression for the Q as a power law is $30(\text{Period}/27.212\text{d})^{0.04}$. Thus the lunar Q is very nearly independent of frequency. Williams *et al.* (2014) state "The uncertainties at 1 month and 1 year are too large to assess whether dissipation increases or decreases with period." The frequency dependence of the tidal response of the early Moon and Earth are unknown. In view of this uncertainty, with the LLR results, we adopt the "constant Q" model, as proposed by Kaula (1964) and Goldreich (1966). Also, we adopt the constant Q model because this is the model the Cuk and Stewart model was intended to approximate. Note that the constant Δt tide has $Q \propto$ Period and so is not a good match to the LLR results (Williams *et al.*, 2014).

The general expression for the tidal potential is (Kaula, 1964}:

$$T(r, \phi, \lambda) = \sum_{lmpq} T_{lmpq}(r, \phi, \lambda) , \qquad (5)$$

where r is the radial distance from the center of the planet on which tides are raised, ϕ and λ are respectively, the latitude and longitude of the point of evaluation of the tidal potential. We restrict l to 2, m and p run from 0 to l, and q runs from -N to N. Note that higher $|q|$ terms are proportional to a higher power of eccentricity e. We chose N=10, to be intentionally excessive. The components of the tidal potential are:

$$T_{lmpq}(r, \phi, \lambda) = (R/r)^{l+1} k_l [U_{lmpq}(R)]_{\text{lag}} \quad (6)$$

$$= k_l R^{2l+1} r^{-l-1} B^*_{lm} C^*_{lmpq} P_{lm}(\sin\phi)$$

$$\times \begin{Bmatrix} \cos \\ \sin \end{Bmatrix}_{l-m \text{ odd}}^{l-m \text{ even}} (\nu^*_{lmpq} - \epsilon_{lmpq} - m(\lambda + \theta^*)) \quad (7)$$

where R is the radius of the planet on which tides are being raised, k_l is the potential Love number, U_{lmpq} is the $lmpq$ component of the tide raising potential, "lag" indicates that the phase of each term is lagged to take account of dissipation. In the subsequent expression, we have

$$B^*_{lm} = Gm^*(l-m)!/(l+m)!\,(2-\delta_{0m}), \quad (8)$$

$$C^*_{lmpq} = (a^*)^{-l-1} F_{lmp}(i^*) G_{lpq}(e), \quad (9)$$

$$\nu^*_{lmpq} = (l-2p)\omega^* + (l-2p+q)M^* + m\Omega^*, \quad (10)$$

where, in general, the asterisk marks quantities belonging to the tide raising body, and ω is argument of pericenter, M is the mean anomaly, Ω is the longitude of the ascending node, and θ is the angle from the inertial reference longitude to the origin of longitudes on the planet on which tides are raised. The Kaula inclination polynomials $F_{lmp}(i^*)$ for l=2 are tabulated in Kaula (1964); the eccentricity functions $G_{lpq}(e^*)$ may be written in terms of Hansen functions:

$$G_{lpq}(e^*) = X^{-(l+1),(l-2p)}_{l-2p+q}(e^*). \quad (11)$$

The Hansen functions, when written as a power series in the eccentricity, have the Newcomb coefficients as coefficients. The lowest order Hansen functions are listed in Kaula (1964). More generally, the Newcomb coefficients (and hence the Hansen functions) may be evaluated with a simple recurrence (Plummer, 1960). Because these are needed many times (each time the tidal potential is evaluated) we "memoized" the table of Newcomb coefficients, i.e. we computed only the coefficients that were needed, as needed, and the computed values were saved in a table for later use. We evaluated the Hansen functions up to order 10 in the eccentricity. The accelerations and torques are derived from this tidal potential.

The "constant Q" tide is a specialization of this general expression in which the phase lags ϵ_{lmpq} are taken to be all equal in magnitude ϵ with the sign of $(\dot{\nu}_{lmpq} - m\dot{\theta})$. The ϵ is related to Q by $tan\ \epsilon = 1/Q$. Note how little the Cuk and Stewart "constant Q" tidal model has in common with the actual constant Q tide.

There is a tidal torque on the Moon that tends to remove the Moon from synchronous rotation. But because the figure of the Moon is out-of-round the synchronous lock remains. What results,

in the simplest situation, in that there is an offset in the direction of the axis of minimum moment from the line pointing to the Earth. This offset results in additional forces on the Earth-Moon orbit. If the Moon's rotation remains simple, then these additional torques can be calculated and taken into account in the equations of tidal evolution (Yoder and Peale, 1981). But, more generally, they can be taken into account by actually integrating the rotation of the Moon and the resulting spin-orbit interactions. We chose the latter course because it is more general.

Evection Resonance Results

Figs. 1 and 2 show aspects of the evolution of the Earth-Moon system in a simulation with Q_e = 100 and A = 1.7376. The A parameter is a measure of the relative dissipation in the Earth and the Moon:

$$A = (k_{2m}/k_{2e})(Q_m/Q_e)^{-1}(m_e/m_m)^2(R_m/R_e)^5. \quad (12)$$

A small A implies relatively small dissipation in the Moon; a large A implies relatively large dissipation in the Moon. In this simulation the obliquity of the Earth and Moon, and inclination of the Moon's orbit are all zero. Because of the assumption of Cuk and Stewart (2012) that the tidal torque is proportional to the angular momentum the domain of applicability is restricted to zero inclination and obliquity. So we first compare our results for zero obliquities and lunar inclination to the results of Cuk and Stewart (2012). In this simulation the initial Earth-Moon separation is $5R_e$, with initial rotation period of 2.53 hours. This corresponds to an evolution from an initial Earth-Moon separation of $3.5R_e$ with an initial rotation period of 2.5 hours, we just saved time by starting the evolution a little further out.

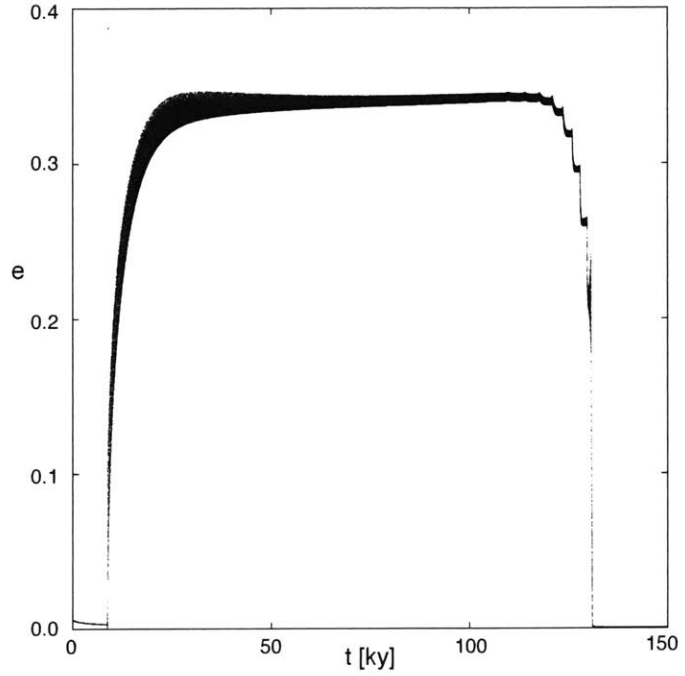

Fig. 1. The eccentricity e of the lunar orbit is plotted versus time t. For this run Q_e = 100 and A = 1.7376. The obliquity is zero.

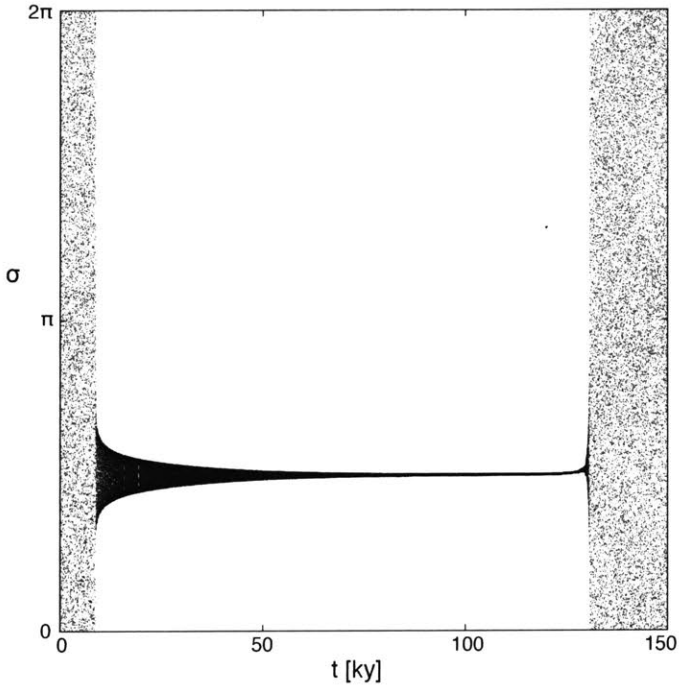

Fig. 2. The evection resonant argument σ is plotted versus time t. For this run Q_e = 100 and A = 1.7376. The obliquity is zero.

The orbital eccentricity (see Fig. 1) shows a sudden increase upon entering the evection resonance (see Touma and Wisdom, 1998, for analytic approximations to the evolution in the evection resonance). The eccentricity reaches an equilibrium in which the tendency to increase in the evection resonance is balanced by a tendency to decrease due to dissipation in the Moon. This is followed by an interval of approximately 130,000 years of nearly constant large eccentricity. Over this interval the semimajor axis and the rotation rate of the Earth decrease. Once the system escapes the evection resonance the eccentricity quickly gets small. The plot of the evection resonance angle (see Fig. 2) shows that once the system is captured, the resonance angle, $\sigma = \varpi - \lambda_\odot$, librates about, in this case, $\pi/2$, and the amplitude of the libration gradually decreases. Here, ϖ is the longitude of pericenter of the lunar orbit, and $\lambda_\odot$ is the longitude of the Earth in its orbit about the Sun. Whether the system is captured about $\pi/2$ or $3\pi/2$ is probabilistic. These results are all roughly consistent with those of Cuk and Stewart (2012), though the details differ.

An important difference with respect to Cuk and Stewart (2012) is the amount of angular momentum that is extracted from the system as a result of this temporary capture into the evection resonance. Fig. 3 shows the final angular momentum versus A from Cuk and Stewart (2012) and for our model, which uses a true constant Q tide. We see that with the full model too much angular momentum is withdrawn from the system to be consistent with the Earth-Moon system.

Evection Resonance Results with Inclination and Obliquity

Unlike the Cuk and Stewart tidal model, our model is fully general in that it can handle arbitrary obliquities and lunar inclination. It is known that to be consistent with today's inclination of the lunar orbit to the ecliptic the Moon had a 10° inclination to the equator of the Earth at about $10R_e$, and the obliquity of the Earth at this point had to be about 10° (see Touma and Wisdom, 1994, 1998). We have made some initial explorations of the process of passage through the evection resonance with nonzero initial obliquity and inclination.

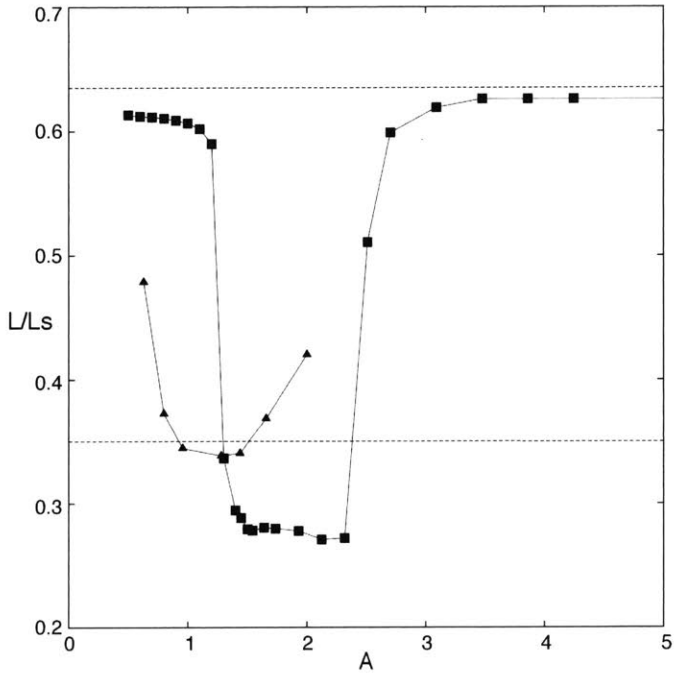

Fig. 3. This plot shows the scaled angular momentum of the Earth-Moon system L/L_s after the system escapes the evection resonance versus the A parameter. The angular momentum scale is $L_s = C \cdot \mathrm{sqrt}(G m_e R_e^{-3})$, where C is the largest moment of inertial of Earth. The filled triangles are the results of Cuk and Stewart (2012), who used their own tidal model. The filled squares are our results using the conventional constant Q model. For our results to be comparable to those of Cuk and Stewart we have taken the obliquities and inclination to be zero. The horizontal line near L/L_s = 0.35 indicates the current angular momentum of the Earth-Moon system; the line L/L_s =0.635 is the initial scaled angular momentum in our runs.

In this exploration we started the Moon with an inclination to the Earth's equatorial plane of 9.9°; the initial obliquity of the Earth is 10°. The initial rotation period of the Earth of 2.5 hours. The initial eccentricity of the lunar orbit is 0.001 and the semimajor axis is a=3.5R_e.

The plots of the orbital elements are similar to the zero obliquity plots, though naturally a little more complicated, and will not be shown in detail. One result is that we found that wobble of the Moon is significantly excited. There are two sources of wobble damping in the Moon. It turns out that tides on the Moon raised by the Earth damp wobble in the Moon (Peale, 1976). Another source of wobble damping is internal dissipation in the Moon (Peale, 1977). We include both of these mechanisms of wobble damping in our simulations.

We adopt a simple model for intrinsic wobble damping. In isolation, intrinsic wobble damping conserves angular momentum but damps body components of the angular velocity. Let $A \le B \le C$ be the principal moments of inertia, and ω^a, ω^b, and ω^c be the corresponding components of the angular velocity. The body components of the angular momentum are $L_a = A\omega^a$, $L_b = B\omega^b$, and $L_c = C\omega^c$. We then calculate $\omega'_a = \omega^a \exp(-\Delta t/\tau)$, and $\omega'_b = \omega^b \exp(-\Delta t/\tau)$, for time interval Δt and time constant τ. Then define $L'_a = A\omega'_a$, $L'_b = B\omega'_b$, and $L'_c = C\omega'_c = C\omega_c$. Let $L = \mathrm{sqrt}(L_a^2 + L_b^2 + L_c^2)$ and $L' = \mathrm{sqrt}((L'_a)^2 + (L'_b)^2 + (L'_c)^2)$, then $L''_a = L'_a(L/L')$, $L''_b = L'_b(L/L')$, $L''_c = L'_c(L/L')$. From this we can compute the new components of the angular velocity on the principal axes: $(\omega'')^a = L''_a/A$, $(\omega'')^b = L''_b/B$, $(\omega'')^c = L''_c/C$. But the principal axes need to be rotated to bring the new angular momentum components into alignment with the direction of the angular momentum in space, which does not change. Define $\mathbf{q} = (\mathbf{L}'' \times \mathbf{L})/(\mathrm{L\ L}'')$, where the boldface indicates vectors in the body frame. Let $\sin\alpha$ be the length of $\mathbf{q}$; α is the angle between the directions of $\mathbf{L}$ and $\mathbf{L}''$. Then let $\hat{\mathbf{q}} = \mathbf{q}/(\sin\alpha)$ be the unit vector about which we rotate the body in inertial space by the angle α to bring the new body components of the angular momentum into alignment with the original angular momentum. The net result is a body with the original angular momentum, but with smaller components of the angular velocity on the $\hat{a}$ and $\hat{b}$ axes. The timescale for wobble damping is {Peale, 1977}:

$$\tau = 3GCQ_m/(k_{2m}R_m^5\omega^3), \qquad (13)$$

where ω is the rotation rate.

We quantify wobble by the ratio of the magnitude of the component of the angular velocity on the $\hat{a}$ and $\hat{b}$ plane (where $\hat{a}$ and $\hat{b}$ are the axes of minimum and intermediate moments of inertia) divided by the total angular velocity. Let

$$\omega_{ab} = (\omega_a^2 + \omega_b^2)^{1/2}, \qquad (14)$$

and

$$\omega = (\omega_a^2 + \omega_b^2 + \omega_c^2)^{1/2}, \qquad (15)$$

then a dimensionless measure of the amount of wobble is ω_{ab}/ω. Fig. 4 shows a plot of this measure of the wobble versus time for a run with obliquities and lunar inclination.

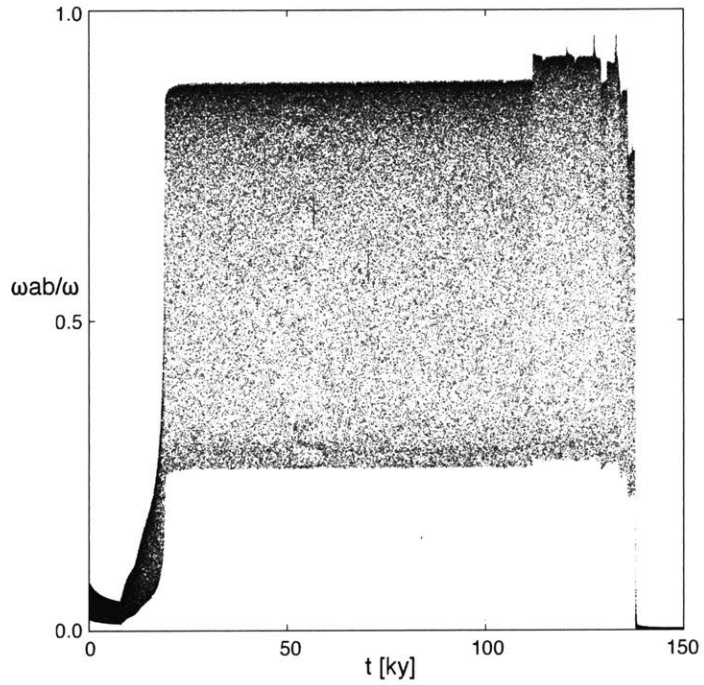

Fig. 4. The wobble ω_{ab} of the Moon is plotted versus time t. For this run Q_e = 100 and A = 2.319. The initial obliquity of the Earth is 10° and the inclination of the lunar orbit to the equator of the Earth is 9.9°.

We expect that the Moon will have a 200-400km deep magma ocean overlain by a 5-10km crust during the interval in which the evection resonance is encountered (Elkins-Tanton, 2008). The interior below the magma ocean is solid. It is not clear that the rigid body dynamics we have assumed is an adequate description of the dynamics of a body with such complicated structure. We might expect that it would be harder to maintain wobble in a body with a magma ocean. So we have carried out a series of runs with the rate of wobble damping enhanced by a factor of 10. This is enough to eliminate the wobble instabilities seen in the first set of runs. Note that Peale (1977) acknowledges that other estimates of the wobble damping timescale are as much as an order of magnitude smaller than his estimate.

Fig. 5 shows a summary of the final angular momentum in the runs in this interval of the A parameter, for Q_e = 100. The results with zero obliquity and inclination are shown with the results for the oblique, inclined case, with and without enhanced wobble damping. It is still the case that too much angular momentum is extracted when the system is captured by the evection resonance to be consistent with the Earth-Moon system. Of course, this is just one tidal model;

perhaps other tidal models would give a final angular momentum that is more consistent with the actual angular momentum of the Earth-Moon system.

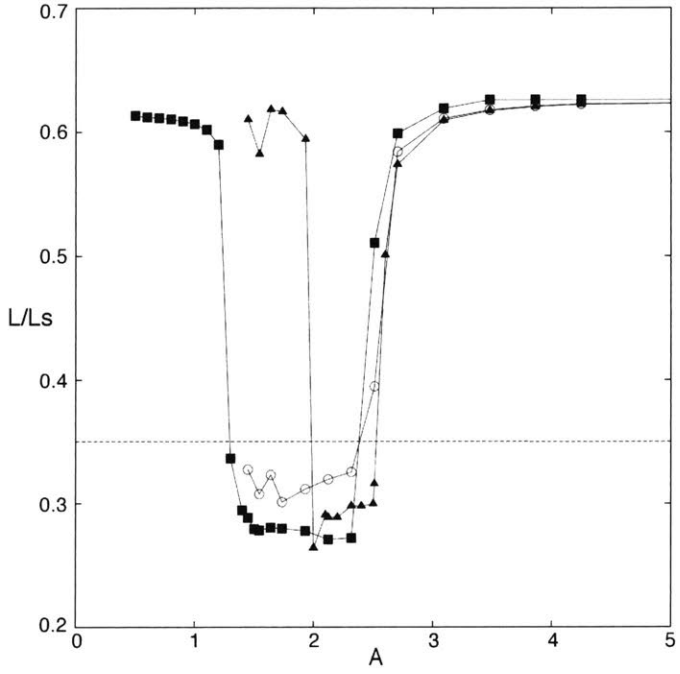

Fig. 5. This plot shows the scaled angular momentum of the Earth-Moon system L/L_s after the system escapes the evection resonance versus the A parameter. The filled squares are the zero obliquity results. The filled triangles are our results with initial Earth obliquity of 10° and initial lunar inclination to the equator plane of 9.9°. The open circles are our results with obliquity and inclination, but with enhanced wobble damping. The horizontal line near L/L_s = 0.35 indicates the current angular momentum of the Earth-Moon system.

A Limit Cycle

We have explored a wider range of parameters than were explored by Cuk and Stewart (2012), and we found a new dynamical phenomenon that may be more promising for the explanation of the Earth-Moon angular momentum than the scenario proposed by Cuk and Stewart. We found that for larger A and larger Q_e the system bypasses the evection resonance, and gets caught in what might best be called a limit cycle associated with the evection resonance. The system is not captured in the evection resonance, but instead the evection resonant argument circulates. The rate of evolution of the evection resonant argument is modulated by the phase of the resonant argument. In the phase plane ($e \cos \sigma$, $e \sin \sigma$), the system circulates around the libration islands

associated with the evection resonance. It appears to be an attracting cycle, thus the proposed name of "limit cycle".

The eccentricity e versus time t for the limit cycle is shown in Fig. 6. For this run we set the obliquities of the Earth and Moon, and the lunar inclination, to zero. We see that the eccentricity is caught in a cycle, and that both the maximum and minimum eccentricity of this cycle are much smaller than the equilibrium eccentricity when the system is caught in the evection resonance. The stroboscopic plot of the evection resonance angle σ versus time t (Fig. 7) shows that the resonance angle circulates (the system is not caught in the evection resonance), and that the rate of evolution is modulated by the phase of the evection resonance angle.

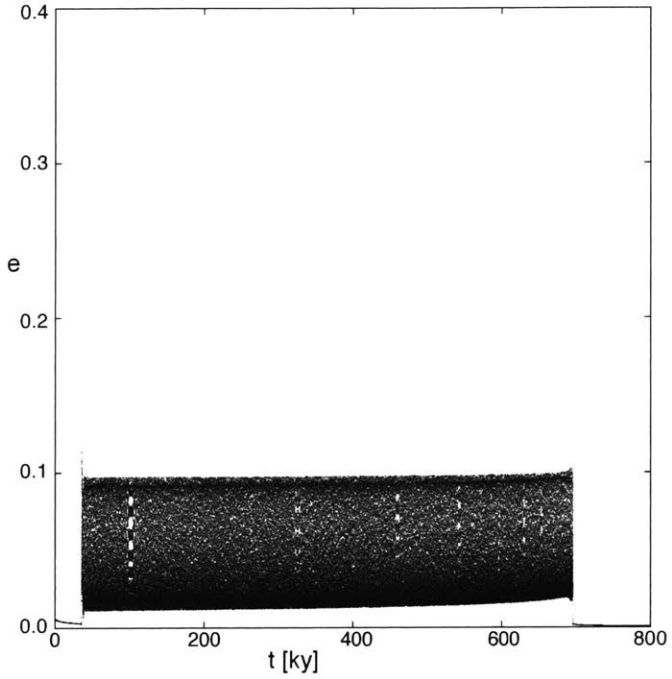

Fig. 6. The limit cycle is exhibited in this plot of eccentricity e versus time t. In this run the obliquities and lunar inclination are zero. This run uses the full model with Q_e=400 and A=13.0.

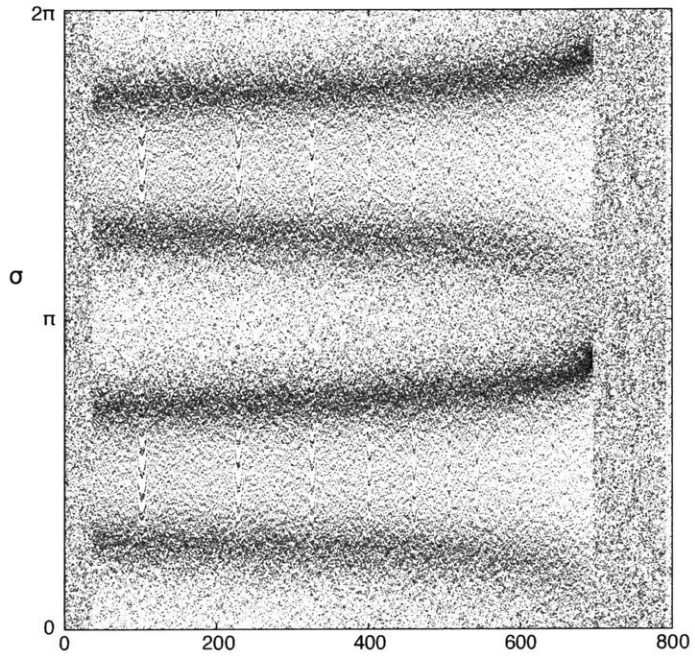

Fig. 7. The limit cycle is exhibited in this plot of resonant argument σ versus time t. The resonant argument circulates and is sampled at regular intervals. Concentrations of points occur at angles at which the evolution of the resonant argument is slower. In this run the obliquities and lunar inclination are zero. This run uses the full model with Q_e=400 and A=13.0.

Fig. 8 shows the angular momentum versus A after the limit cycle is passed. In these runs, the initial obliquities and lunar inclination were set to zero, and Q_e=400. For Q_e=100 we did not find the limit cycle behavior over this same range of A. We see that over a broad range of A, roughly $8 < A < 15$, significant angular momentum is extracted from the system. Recall that additional angular momentum is extracted from the system by solar tides as the system evolves from $10R_e$, where these simulations were terminated, to the present $60R_e$, though the extent of this additional angular momentum extraction surely depends on the tidal model. So it is appropriate that the limit cycle results lie above the Earth-Moon line.

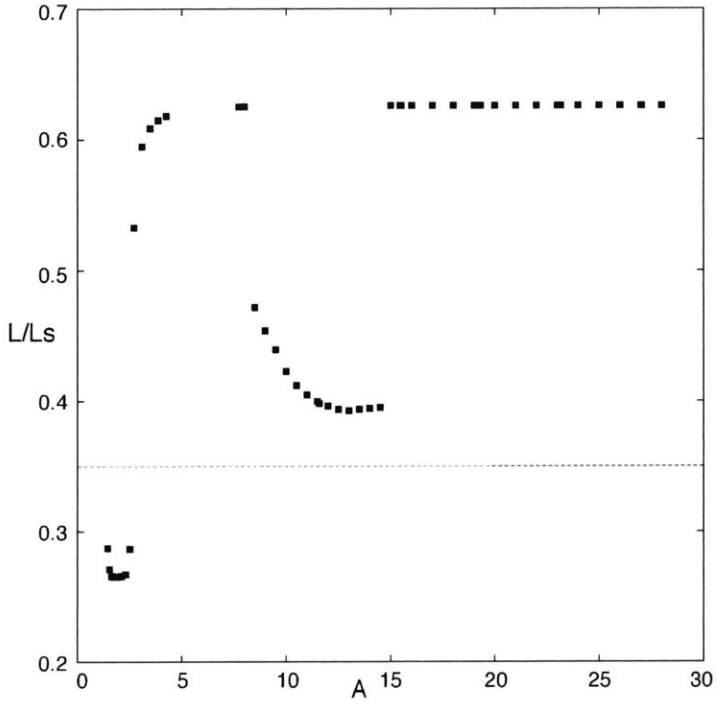

Fig. 8. This plot shows the scaled angular momentum after passage through the limit cycle versus the dissipation parameter A. In these runs with the full model, the obliquities and lunar inclination are set to zero, and Q_e = 400. We see a broad range of A in which significant angular momentum is extracted from the system. The horizontal line indicates the present angular momentum of the Earth-Moon system.

We have also found that the limit cycle behavior exists for Q_e=400 when the obliquities and lunar inclination are nonzero.

A Simplified Model of the Limit Cycle

The behavior in the limit cycle can be captured to some extent by a simplified model. In this simplified model, we take the obliquities of the Earth and Moon, and the inclination of the lunar orbit to the equator plane of the Earth all to be zero. The Hamiltonian governing the behavior near the evection resonance (see Touma and Wisdom, 1998) is then

$$H = n_2\Sigma - \tfrac{1}{2}n_1 J_2 (R_e/a_1)^2 L'(1-e^2)^{-3/2} - n_2^2/n_1 \cdot L' e^2 \cdot 15/8 \cdot \cos 2\sigma, \qquad (16)$$

where $\Sigma = L'(1 - (1 - e^2)^{1/2})$ is the momentum conjugate to the evection angle $\sigma = n_2 t - \varpi$, where ϖ is the longitude of the pericenter, and where $L' = (m_m \mu a_1)^{1/2}$, with $\mu = G m_m m_e$, n_2 is the mean

motion of the Earth about the Sun, n_1 is the mean motion of the Moon about the Earth, J_2 is the Earth oblatenesss factor. Note that

$$e^2 = \Sigma/L' (2 - \Sigma/L') . \quad (17)$$

We assume that $J_2 = J_{20}(\omega/\omega_0)^2$ where ω is angular rate of rotation of the Earth. We assume J_{20} = 0.001083 for ω_0 corresponding to a 24 hour rotation. We express the Hamiltonian in terms of the non-singular momentum ξ = sqrt(2Σ) cos σ and conjugate coordinate η = sqrt(2Σ) sin σ. The equations of motion are just Hamilton's equations.

To Hamilton's equations we add terms that reflect the tidal evolution. These are derived from the constant Q Darwin-Kaula model {Kaula1964}.

Based on the Kaula series, we might naively write

$$da/dt = 2/3\ Ka\ (1 - (19A - 51/4)e^2 + (1065/16 - 551/8\ A)e^4 + \cdots) , \quad (18)$$

$$de/dt = -1/3\ K\ ((7A - 19/4)e + (299/8\ A - 503/16)e^3 + \cdots) , \quad (19)$$

where

$$K = 9/2 \cdot k_{2e}/Q_e \cdot m_m/m_e \cdot \mathrm{sqrt}(G m_e R_e^{-3})\ (R_e/a)^{13/2} . \quad (20)$$

But tides on the Moon have a net torque on the Moon that tends to remove the Moon from synchronous rotation. If the Moon's minimum moment of inertia is not aligned with the Earth, then the Moon is subject to a gravity gradient torque because of its nonzero gravitational moment C_{22}. In the equilibrium orientation of the Moon these two torques balance. This orientation offset results in additional terms in the equations governing the evolution of the lunar orbit. These additional terms can either be taken into account by integrating the rotation of the Moon, as we did in the full model, or by modifying the expressions for the tidal evolution of the semimajor axis and eccentricity. Here we follow the latter course. Taking this effect into account, the total rate of change of the semimajor axis and eccentricity of the Moon are

$$da/dt = 2/3\ Ka\ (1 + c_2\ e^2 + c_4\ e^4 + c_6\ e^6 + \cdots) , \quad (21)$$

$$de/dt = -1/3\ K\ (d_1\ e + d_3\ e^3 + d_5\ e^5 + \cdots). \quad (22)$$

For $(5/2)n < \omega$, the coefficients are:

$$c_2 = 51/4 - 7A, \quad (23)$$

$$c_4 = 1065/16 - 403/8\ A, \quad (24)$$

$$c_6 = 29229/128 - 1207/6\ A, \quad (25)$$

and

$d_1 = 7A - 19/4,$ (26)

$d_3 = 347/8\,A - 503/16,$ (27)

$d_5 = 3619/24\,A + 14117/128.$ (28)

For $2n < \omega < (5/2)n$, the coefficients are:

$c_2 = 51/4 - 7A,$ (29)

$c_4 = 1065/16 - 403/8\,A,$ (30)

$c_6 = -3044003/2304 - 1207/6\,A,$ (31)

and

$d_1 = 7A - 19/4,$ (32)

$d_3 = 347/8\,A - 503/16,$ (33)

$d_5 = 3619/24\,A + 629323/768.$ (34)

For $(3/2)n < \omega < 2n$, the coefficients are:

$c_2 = 51/4 - 7A,$ (35)

$c_4 = -3559/16 - 403/8\,A,$ (36)

$c_6 = -41123/2304 - 1207/6\,A,$ (37)

and

$d_1 = 7A - 19/4,$ (38)

$d_3 = 347/8\,A + 1809/16,$ (39)

$d_5 = 3619/24\,A - 37621/768.$ (40)

These results generalize the result used in Yoder and Peale (1981).

Though we have reported these expressions for various conditions on the rotation rate relative to the lunar mean motion, it turns out that these were not needed. For the evolution in the limit cycle the condition $(5/2)n < \omega$ is always maintained; there are no changes in the values of the tidal constants during the evolution.

To these tidal orbital equations we must add an equation for the tidal slowing of the rotation of the Earth. We find

$$d\omega/dt = -L/(\lambda\, m_e\, R_e^2)\cdot(\tfrac{1}{2}a^{-1}\cdot da/dt - e/(1-e^2)\cdot de/dt), \quad (41)$$

where $\lambda = C/(m_e R_e^2) = 0.3308$, with polar moment of inertia C, and $L = L'(1 - e^2)^{1/2}$.

The simple model captures the evolution into the limit cycle. This demonstrates that the limit cycle is not an artifact of the rather complicated full model. But the agreement with full model is not as good as one would have hoped. First, the range of eccentricity variation is shifted to larger values in the simplified model. The eccentricity reaches values near 0.16 for the simplified model, but only values near 0.1 for the full model. Also, the range of the A parameter in which the limit cycle phenomenon occurs is different for the simplified model and the full model. Fig. 9 shows the summary plot of scaled angular momentum versus the A parameter for the simplified model. We do not yet understand why there is this disagreement. Presumably, the full model captures some physical effect that we have not identified for inclusion in the simple model. But the fact that the simple model exhibits the limit cycle is important, nevertheless.

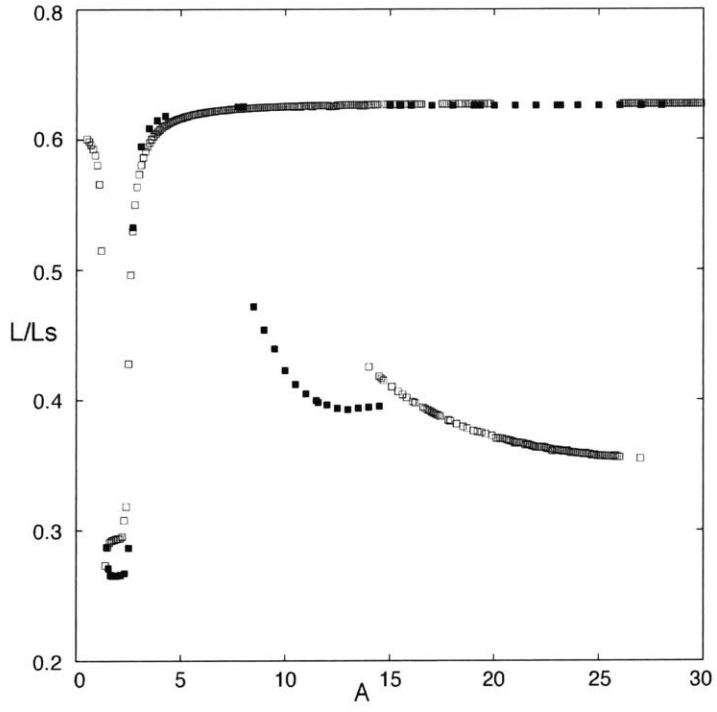

Fig. 9. Results of the simplified model with $Q_e = 400$. The open squares mark the results using the simplified model; the filled squares mark the results of the full model. The limit cycle is found with the simplified model, though the results do not match the full model exactly. Note that capture by the limit cycle is probabilistic for some values of A.

Discussion

We are concerned that the high eccentricities obtained during the temporary capture in the evection resonance (e of order 0.35) would lead to large tidal heating, which in turn would change the parameters of the Moon and the consequent orbital evolution. Recall that the formula for tidal heating (Peale and Cassen, 1979) is proportional to the square of the orbital eccentricity and inversely proportional to sixth power of the semimajor axis. During the temporary capture in the evection resonance the eccentricity is high and the semimajor axis is small, so we can expect large tidal heating. Of course, the Moon is expected to have a thin (5-10km) lid underlain by a magma ocean (200-400km) during the interval in which the system is captured by the evection resonance. This configuration may be expected to actually increase the tidal heating, as heating in a thin lid can actually be larger than in a corresponding solid body (Peale *et al.*, 1979). To properly address the consequences of this tidal heating on the orbital evolution requires examining a coupled thermal-orbital model, which we plan to do in a subsequent work.

Note however that the limit cycle behavior that we have discovered has an advantage in this regard. The typical eccentricity is less than of order 0.1. So according to the tidal heating formula, the rate of tidal heating, all other factors remaining the same, would be less by a factor of about 10. So the concern about tidal heating affecting the orbital evolution is mitigated, to some extent. The problem should still be addressed in a coupled thermal-orbital model.

Conclusion

The tidal model of Cuk and Stewart (2012) was described as approximating a constant Q tide, but, in fact, had little to do with a constant Q tide. We have explored the early evolution of the Earth-Moon system through the evection resonance with a true constant Q tide. We found that we can reproduce the basic phenomenon discovered by Cuk and Stewart (2012), which is that significant angular momentum can be extracted form the system. However, we find that the evection resonance actually extracts too much angular momentum to be consistent with the current Earth-Moon system. Exploring a broader range of parameters than explored by Cuk and Stewart (2012), we found a new phenomenon, which we describe as a limit cycle of the evection resonance. The resonant argument of the evection resonance is not oscillating, but rather is circulating in a manner that is modulated by the phase of the evection resonant argument.

Angular momentum is also extracted from the Earth-Moon system if the system is captured by the limit cycle. We find that after the system escapes the limit cycle the angular momentum is a little larger than the current angular momentum of the Earth-Moon system, but this is good as during the subsequent evolution to the present configuration solar tides continue to extract a small amount of angular momentum. The range of parameters that give an appropriate reduction of angular momentum is broader than the range of parameters for which the evection resonance reduces the angular momentum. Of course, other tidal models should be explored. We feel that the limit cycle holds promise for explaining the angular momentum of the Earth-Moon system, in the context of the new scenarios for harder Moon-forming impacts.

Acknowledgements: We thank M. Cuk, S. Stewart, J. Meyer, and W. Ward for interesting and helpful discussions.

Chapter 3

Coupled orbital-thermal evolution of the early Earth-Moon system with a fast-spinning Earth

ZhenLiang Tian, Jack Wisdom, Linda Elkins-Tanton

Abstract

Several new scenarios of the Moon-forming giant impact have been proposed to reconcile the giant impact theory with the recent recognition of the volatile and refractory isotopic similarities between Moon and Earth. Two scenarios leave the post-impact Earth spinning much faster than what is inferred from the present Earth-Moon system's angular momentum. The evection resonance has been proposed to drain the excess angular momentum, but the lunar orbit stays at high orbital eccentricities for long periods in the resonance, which would cause large tidal heating in the Moon. A limit cycle related to the evection resonance has also been suggested as an alternative mechanism to reduce the angular momentum, which keeps the lunar orbit at much lower eccentricities, and operates in a wider range of parameters. In this study we use a coupled thermal-orbital model to determine the effect of the change of the Moon's thermal state on the Earth-Moon system's dynamical history. The evection resonance no longer drains angular momentum from the Earth-Moon system since the system rapidly exits the resonance. Whereas the limit cycle works robustly to drain as much angular momentum as in the non-thermally-coupled model, though the Moon's tidal properties change throughout the evolution.

Introduction

The giant impact theory for lunar formation (Hartman and Davis, 1975, Cameron and Ward, 1976) can account for the large angular momentum of the Earth-Moon system, the late formation of the Moon, the Moon's deficiency of iron and volatiles, and the presence of a magma ocean in the early lunar history. Simulations of the impact and accretion processes led to a well accepted standard model of lunar formation (Canup and Asphaug, 2001, Canup, 2004, 2008), in which a Mars-sized body collided with the proto-Earth, forming an Earth-Moon system with the angular

momentum equal to the present value. This model fit well with multiple lines of observations, until the relatively recent recognition of the isotopic similarities of the elements oxygen (Wiechert *et al.*, 2001), chromium (Lugmair and Shukolyukov, 1998), tungsten (Touboul *et al.*, 2007) and titanium (Zhang *et al.*, 2012) between lunar samples and the terrestrial mantle. These isotopic similarities, especially of highly refractory elements like Ti, which is not likely to have equilibrated during a post-impact equilibration phase (Pahlevan and Stevenson, 2007), are evidence that the lunar material was predominantly derived from the proto-Earth, unless the impacting planet had isotopic signatures very close to those of the proto-Earth (Mastrobuono-Battisti, Perets, and Raymond, 2015, Kaib and Cowan, 2015). However, the standard model indicates that the Moon should have mostly been derived from the impactor, given the dynamical constraint that the angular momentum of the Earth-Moon system at the time of lunar formation should be close to the present value. Lock *et al.* (2016) proposed that a fast-spinning post-impact Earth could explain the depletion of volatiles in the Moon. After a high-energy, high-angular momentum giant impact, the Earth can be in a post hot spin stability limit state. In this state, the Earth's mantle, atmosphere, and the circumplanetary disk form a well-mixed continuous structure of BSE vapor that extends beyond the Roche limit. The volatile depletion in the Moon and the isotopic similarities between the Earth and Moon are natural results of the equilibration between the condensing Moon and the BSE vapor. The enrichment of the heavy potassium isotopes in the Moon (Wang and Jacobsen, 2016) supports this accretion model. So the case for a fast-spinning post-impact Earth gets stronger.

Several new impact scenarios (Cuk and Stewart, 2012, Canup, 2012, Reufer *et al.*, 2012) have been proposed to reconcile this contradiction. While these models can produce a Moon with essentially the same materials that make up the terrestrial mantle, they all assume impact angular momenta much higher than the current angular momentum of the Earth-Moon system. The Reufer *et al.* scenario assumes that the excess angular momentum is removed through the escape of a portion of the impactor mass from the system just after the impact. The other two assume an Earth-Moon system with an initial angular momentum much higher than the current value.

With dynamical simulations that begin with a fast-spinning Earth, it was suggested (Cuk and Stewart, 2012) that the excess angular momentum can be transferred to the Earth's orbit around the Sun through an orbital resonance between the precession of the lunar pericenter and the Earth's orbit around the Sun. Upon the system's entry into this resonance, called the evection resonance, the period of precession of the lunar pericenter is locked to one year, the angle between the direction of the lunar pericenter and the direction of the Sun from the Earth (the evection angle, see Fig. 3. in the introduction of the thesis) begins to oscillate about either $\pi/2$ rad or $3\pi/2$ rad, and the eccentricity of the lunar orbit is raised. While the system is captured in the evection resonance, the eccentricity is maintained at a high value, the semi-major axis of the lunar orbit decreases, and the Earth despins, all contributing to the loss of angular momentum from the Earth-Moon system. With this orbital mechanism to remove the excess angular momentum, the two giant impact scenarios work well to produce an Earth-Moon system that could meet both the chemical and angular momentum constraints.

However, passage through the evection resonance would cause large tidal heating in the Moon. To illustrate the problem, consider the heating in the Moon with fixed parameters. The resonance excites the eccentricity of the lunar orbit to as high as 0.5, and keeps the system trapped in it for a period of ~100,000 years, when the Moon is just about 4-7R_e from the Earth. Take the rate of tidal heating of the Moon to be $\frac{21}{2}\frac{Gm_e^2 e^2 {R_m}^5 n}{a^6}\frac{k_{2m}}{Q_m}$ (Peale and Cassen, 1978), where e, n, a are the lunar orbit's eccentricity, mean motion, and semi-major axis. Approximate k_{2m} with $\frac{3\rho g R_m}{19\mu}$, where μ, ρ, g are the Moon's rigidity, density and surface acceleration. Taking the time spent in the resonance to be 100,000 years, e = 0.5, Q = 100, $\rho = 3.34\times10^3$ kg m^{-3}, $\mu = 6.5\times10^{10}$ N m^{-2}, g = 1.62 m s^{-2}, the Earth-Moon distance to be 6.5 R_e, the Moon's specific heat capacity to be 1256 J kg^{-1} °C^{-1}, and the lunar mass to be 7.438×10^{22} kg, the temperature of the Moon will be raised by ~10,000 °C after the system's passage through the evection resonance. Such an increase in temperature would have completely vaporized the Moon! So the assumption of fixed parameters is inadequate. It is necessary to take into account how the large tidal heating in the Moon changes the parameters and consequently the dynamical evolution.

With new orbital simulations that use a more complete tidal model, and are run over a greater range of parameters, an alternative mechanism was found to be capable of removing the Earth-Moon system's angular momentum while avoiding the drawbacks of the evection resonance (Wisdom and Tian, 2015). In this mechanism, which is a limit cycle related to the evection resonance, the lunar eccentricity oscillates in a range with an upper bound typically near 0.1, and the evection angle circulates from 0 to 2π rad with the same period as the oscillation of eccentricity. During the system's capture in the limit cycle, the semi-major axis of the lunar orbit decreases, and the Earth despins, so the angular momentum of the Earth-Moon system is also reduced, as in the evection resonance. Compared with the evection resonance, this mechanism excites the system to orbital eccentricities smaller by a factor of 3-5, even using the upper bound of eccentricity oscillation. Since the rate of tidal heating is proportional to the square of eccentricity, the Moon is therefore much less seriously heated by tides through the limit cycle. The limit cycle has an additional and significant advantage that it occurs over a much wider range of tidal parameter than the evection resonance.

How well do these two mechanisms (the evection resonance and the evection limit cycle) work when considering the consequences of tidal heating? Heating of a body must induce changes in the body's tidal properties, and thus affect the orbital evolution by changing the tidal accelerations. The purpose of this study is to determine the manner and extent of the effect of the thermal evolution of the Moon on the orbital evolution that starts with a fast-spinning Earth, and to evaluate the effectiveness of the limit cycle and the evection resonance in removing the Earth-Moon system's excess angular momentum.

Model

The computational scheme is composed of two interacting subsystems, the thermal evolution of the Moon and the orbital evolution of the Earth, Moon, and Sun. The thermal system tracks the changes of the Moon's thermal profile, structure, and tidal properties over time. The orbital system tracks the locations and velocities of the Earth, Moon, and Sun, as well as the Earth and Moon's rotational state.

At every time step, the thermal system reads the values of lunar orbital eccentricity and semi-major axis from the orbital system, because they are needed to calculate the heating of the Moon. The thermal system determines the values of k_{2m} and Q_m, which are then used by the orbital system for calculating the tidal accelerations.

In the thermal model, we begin with a lunar structure that is suggested by magma ocean solidification studies: a thin (5 km), solid anorthositic flotation lid overlies a liquid magma ocean of ~100 km in depth, which overlies a solid interior. According to some solidification models (for example, Elkins-Tanton *et al.*, 2011), an original magma ocean as deep as 1000 km, without a lid on the surface, can solidify 80% in just several thousand years, as heat efficiently escapes the magma ocean to space by radiation. After this point, plagioclase begins to crystalize and buoyantly segregates from the magma to form a lid at the surface. The presence of the lid switches the heat loss regime from radiation from a free liquid surface to the significantly less efficient thermal conduction through the solid lid. Then it takes tens of millions of years (My) to solidify the remaining magma. During the first several thousand years, tidal dissipation in the Earth dominates the orbital evolution of the Earth-Moon system, since the dissipation in the Moon without a solid lid overlying the magma ocean would be very small. The orbital change is mainly an increase in the lunar orbit's semi-major axis, with little change in eccentricity and the system's angular momentum. Since several thousand years is short compared to the ~100,000 years the system spends in the evection resonance or limit cycle, and nothing significant happens during this period, we choose to start the evolution assuming 80% of the magma ocean has already solidified and that a thin plagioclase lid has been formed.

For radiogenic heating in the Moon, we assume that all the heat-generating isotopes are retained in the magma during magma ocean solidification. We infer the amount of heating according to chondritic abundances of radiogenic isotopes, assuming the simulated evolution begins 60 My after the formation of calcium-aluminum-rich inclusions, as suggested by tungsten isotope chronologies (Touboul *et al.*, 2007). We find that radiogenic heating is not a significant contribution to the energy budget.

The orbital system's set-up and evolution are the same as in Wisdom and Tian (2015), and we briefly outline it here. We evolve the locations and velocities of the Earth, Moon, and Sun using the N-body symplectic mapping method (Wisdom and Holman, 1991). In the N-body symplectic map, we integrate the system alternatively with the Kepler Hamiltonians (which are directly integrable) for a time step and then the interaction Hamiltonian (also easily solvable) for the same step length. As long as the time step length is short compared with the shortest period of the system (here the lunar orbital period), this solution approximates the solution of the complex real Hamiltonian (the sum of the Kepler Hamiltonians and the interaction Hamiltonian) with satisfaction. We also evolve the rigid body rotational states of the Earth and Moon, and include the spin-orbit interactions of the Earth with the lunar orbit and the Earth's orbit around the Sun, and the Moon's spin-orbit interactions with the lunar orbit around the Earth. In Wisdom and Tian (2015) we used both the quaternion equations of motion (Sussman and Wisdom, 2015) and the Lie-Poisson algorithm (Touma and Wisdom, 1993) for the rigid body dynamics, and the two approaches produced the same results. In this study we use the Lie-Poisson integrator.

The full form of the Darwin-Kaula tide (Kaula 1964) is used for computing the tidal accelerations of the Earth and Moon. The tidal potential is expanded to a sum of terms of different frequencies. Each frequency component of the tidal potential, V_{lmpq}, is specified by the combination of numbers (l,m,p,q), as is the phase lag for each frequency, which is denoted as ϵ_{lmpq}. We adopt a constant-Q model (Q being frequency-independent rather than time-independent) with $\epsilon_{lmpq} = Q_m^{-1} \cdot \mathrm{sign}(m(\dot{\Omega} - \dot{\theta}) + (l-2p)\dot{\omega} + (l-2p+q)n)$, where $\dot{\Omega}$ and $\dot{\omega}$ denote the rate of change of the perturber's longitude of ascending node and argument of pericenter, n denotes the orbital mean motion, $\dot{\theta}$ denotes the rotation rate of the deforming body. The constant Q model is consistent with what is known about the frequency dependence of the Q of the present day Moon (Williams *et al.*, 2005, 2014). A disadvantage of the constant Q model is that the tidal phase lags exhibit discontinuities near commensurabilities, which presumably only approximate the actual behavior. An alternate choice could have been the popular Mignard tidal model (Mignard, 1979), but in this model the frequency dependence of the Q is not consistent with what is observed. We feel the advantages of the constant Q model outweigh its disadvantages.

The evolution of the thermal system is governed by a set of processes including tidal heating and thermal diffusion in the lid, partial melting and melt migration in the lid, crystallization and release of latent heat and radiogenic heating in the magma ocean, and exchange of heat between the magma ocean and the lid. We illustrate each of them below.

(1) Tidal heating and thermal diffusion in the lid

The contribution of tidal heating and conduction of heat to the lid's temperature evolution is described by

$$\frac{\partial T}{\partial t} = \frac{2\kappa}{r}\frac{\partial T}{\partial r} + \frac{\partial}{\partial r}\left(\kappa\frac{\partial T}{\partial r}\right) + \frac{H}{\rho_l C_p}, \quad (1)$$

where T is the local temperature, r is the radius, t is the time, κ is the thermal diffusivity, ρ_l is the density, C_p is the specific heat capacity, H is the local volumetric tidal heating rate. We use C_p = 1256 J kg^{-1} °C^{-1} and $\kappa = 10^{-6}$ m^2 s^{-1}. We take ρ_l = 2927 kg m^{-3}, the average grain density of the crust (Wieczorek *et al.*, 2013). The current actual crustal density with porosity is 2550 kg m^{-3}, but the porosity is the result of billions of years of accumulative impact cratering, which was not the case for the earliest period of the Moon. We also made simulations using the current density (2550 kg m^{-3}) and find that the results are insensitive of the choice between the two densities. The first two terms on the right side constitute Fourier's law written in spherical coordinates, with the approximation that the heating and temperature are azimuthally homogeneous.

In the computation, first we parameterize the depth of each layer using y, which varies from 0 (at the surface) to 1 (at the bottom of the lid). So

$$r = R_m - \delta_l \cdot y, \quad (2)$$

where δ_l is the thicknesses of the lid. Let $T'(t, y) = T(t, r)$, and note that δ_l is varying with time, equation (1) becomes

$$\frac{\partial T'}{\partial t} = \left(\frac{y\dot{\delta}_l}{\delta_l} - \frac{2\kappa}{r\delta_l}\right)\frac{\partial T'}{\partial y} + \frac{\kappa}{{\delta_l}^2}\frac{\partial^2 T'}{\partial y^2} + \frac{H}{\rho_l C_p}. \quad (3)$$

Then we discretize the lid to 100 layers of thickness $\Delta r = \delta_l \Delta y$ (Δy = 1/100). Denote the temperature of the i^{th} layer to be T^i, equation (3) becomes

$$\frac{dT^i}{dt} = \left(\frac{y\dot{\delta}_l}{\delta_l} - \frac{2\kappa}{r\delta_l}\right)\left(\frac{T^{i+1} - T^{i-1}}{2\Delta y}\right) + \frac{\kappa}{{\delta_l}^2}\left(\frac{T^{i+1} - 2T^i + T^{i-1}}{\Delta y^2}\right) + \frac{H}{\rho_l C_p}. \quad (4)$$

We evolve the lid temperatures according to equation (4). Note that this equation does not include the thermal effects of partial melting and melt migration, which is treated separately and will be elaborated later.

The expression for the azimuthally averaged rate of volumetric tidal heating in the lid is derived based on Peale and Cassen(1978), and we correct and outline it in the appendix. It is

$$H = \mu G^2 m_E^2 n R_M^2 a^{-6} Q^{-1} g^{-2} k_{2m}^2 (21/5 \cdot \alpha_0^2 + 42/5 \cdot \alpha_1^2 - 252/5 \cdot \alpha_1 \alpha_2 + 126 \alpha_2^2 + 252/5 \cdot \alpha_3^2) \times (e^2 + 403/56\, e^4 + 1207/42\, e^6 + 336953/4032\, e^8 + \cdots), \quad (5)$$

where g = 1.62 m s^{-2} is the surface acceleration, and the α_i are functions of the layer's position and the lid thickness, which are presented in the appendix. In this expression, a, Q, k_{2m}, e and α_i all evolve over time.

The dissipation factor, Q, for a layer at temperature T is given by the Ojakangas and Stevenson (1986) formula

$$\frac{1}{Q}(T) = \frac{1}{Q_{mmax}} + \left[\frac{1}{Q_{mmin}} - \frac{1}{Q_{mmax}}\right]\left(\frac{T}{T_p}\right)^n, \quad (6)$$

where T_p is the melting temperature of plagioclase. We take T_p = 1550 °C. We set Q_{mmin} = 20, and let Q_{mmax} vary with the runs. Experimentally, the parameter n ranges from 20 to 30 (Ojakangas and Stevenson, 1986); we use 25. The choice of Q_{mmin} = 20 is somewhat arbitrary. The current Q of the Moon is approximately 20 (Williams *et al.*, 2005, 2014).

We take an effective $1/Q_m$ of the Moon for use in the orbital system to be the average of the $1/Q$ of the individual lid layers.

k_{2m} as a function of the lid thickness is given in the appendix. The rigidity of the shell is taken to be μ = 6.5×10^9 N m^{-2}. This is an order of magnitude smaller than the rigidity used by Peale and Cassen (1978) based on seismic velocities in today's cold Moon. We use a lower rigidity because of the high temperatures in the lid during the early epoch, though we do not explicitly take into account the temperature dependence of the rigidity. To some extent the choice of rigidity is arbitrary and offset by the uncertainty in the values of the tidal Qs of the early Moon and Earth.

(2) partial melting and melt migration in the lid

Tidal heating strongly affects the solid lid, and in these models raises parts of the lid above its melting temperature. Melting portions of the lid creates plagioclase melt migration upward in the lid, and can result in plagioclase melt eruption and re-solidification on the surface. This process has the critical effect of changing the relationship of age of the plagioclase with depth in the lid: Originally, the youngest plagioclase is at the bottom of the lid where it has floated from the remaining magma ocean, but if remelted and erupted, then the youngest plagioclase is on the surface.

Whenever some part of the lid is heated to T_p, the plagioclase there begins to melt. The melt fraction depends on the amount of heating after the temperature reaches T_p. For example, after the lid has been subjected to tidal heating and thermal diffusion for some time, a particular lid layer could reach a temperature that exceeds T_p by a positive value, ΔT, according to equation (4). But physically, after the layer temperature reaches T_p, the further amount of heating, ΔE, would result in melting of layer rather than further raising the layer temperature. Let V_{layer} is the volume of the layer, L_p is the latent heat in melting and crystallization of plagioclase, then $\Delta E = V_{layer}\rho_l C_p \Delta T$. The volume of the melted solid is $V_{melt} = \Delta E/(L_p\rho_l)$, so the melt fraction is

$$f_{melt} = V_{melt}/V_{layer} = (C_p/L_p)\Delta T. \quad (7)$$

We start the computation of melting in the bottom layer. Once some melt is produced, it begins to rise through the lid to the surface, thermally interacting with the lid layers that it travels through. When the melt meets a layer that is also heated to T_p and melted to some fraction, the two bodies of melt join and migrate upward together. When the melt meets a cold layer, or a layer with a negative ΔT, some fraction crystallizes there, releasing the latent heat and increasing the layer's temperature. Meyer *et al.* (2010) found that the change in this fraction value from 0 to 1 does not affect the results qualitatively. We take the fraction to be 1 in this study. One exception is when the cold layer is very near T_p. In this situation, the full amount of crystallization will raise the layer temperature above T_p. Therefore, in this case we take the volume of melt crystallization to be the amount that is just enough to raise the layer temperature to T_p.

When the body of melt reaches the surface, it is instantly quenched and assumes the equilibrium surface temperature. Then any hollow in each layer caused by melting and migration is filled with material from the neighboring overlying layer or layers, with the heat content of the filling material mixed with that of the layer to be filled, thus updating the temperatures of each layer.

We take the latent heat in the melting and crystallization of plagioclase to be 4.187×10^5 J kg^{-1}, and the equilibrium surface temperature to be 280 °K.

(3) magma ocean model

The magma ocean is assumed to be convecting and follows an adiabatic temperature profile; for the Moon this adiabatic temperature varies little with pressure and we approximate the temperature as constant with depth. Therefore, instead of tracking the full temperature profile of the magma ocean, we only track this constant temperature, T_f, and the thicknesses of the lid (δ_l), the magma ocean(δ_f), and the radius of the solid interior (δ_s), which are related to T_f in the process of magma ocean solidification.

The thermal evolution of the magma ocean is described by

$$\dot{E}_r - \dot{E}_c - L\rho_f \dot{V}_f = C_p \rho_f V_f \dot{T}_f \,, \qquad (8)$$

where $\dot{E}_r$ is the rate of radiogenic heating of the magma ocean, $\dot{E}_c$ is the rate at which heat is conducted from the magma ocean to the lid at the base of the lid, the third term on the left hand side is the rate of production of latent heat of solidification as the volume of the magma ocean (V_f) decreases, and the right hand side is the rate of change of the heat content of the magma ocean due to its changing temperature. If the bottom of the lid is heated above the magma ocean temperature, thermal conduction will reverse direction to inwards, and V_f will increase (As we will see in Fig. 4). We take ρ_f = 3000 kg m^{-3}. Meyer *et al.* (2010) included an additional $\dot{V}_f$ related term on the right hand side to represent the change of the magma ocean's heat content due to volume decrease during solidification. However, this is compensated by the increase in heat content of the crystals settling out as their volume increases. Here we correct this error.

We compute the radiogenic heating by extrapolating the chondritic abundances of ^{235}U, ^{238}U, ^{40}K, and ^{232}Th back to the time of formation of the Moon. We then multiply by the heat production per mass, the density, and the volume of the magma ocean and sum over the four isotopes. The half-lives, current abundances, and specific heat productions are given by Turcotte and Schubert (2002).

The solidus of the magma ocean is parameterized to fit the bulk lunar mantle solidus of Longhi (2003). We use

$$T_s(r) = 2134 - 0.1724r - 1.3714\times10^{-4}r^2, \quad (9)$$

where T_s is the solidus in Kelvin and r is the radius in km. $T_f = T_s(\delta_s)$, so $\dot{T}_f$ can be related to $\dot{\delta}_s$:

$$\dot{T}_f = DT_s(\delta_s) \cdot \dot{\delta}_s . \quad (10)$$

Note that the solidus temperature of the magma ocean at the base of the lid, $T_s(\delta_s)$, is lower than T_p. This is because the pure mineral has a higher melting temperature than the multiphase melt has.

As the magma ocean solidifies, both plagioclase and mafic minerals crystallize from the magma. We assume constant fractional crystallization such that the volume of the crystallized plagioclase is of a fixed proportion, f, of the volume of all crystallized solids. Upon crystallization, the plagioclase floats to join the lid, while the mafic crystals precipitate on the solid interior. Let $V_l(\delta_l) = 4\pi/3(R_m^3 - (R_m - \delta_l)^3)$ denote the volume of the lid, $V_s(\delta_s) = 4\pi/3\ \delta_s^3$ denote the volume of the solid interior, $\dot{V}_l$ and $\dot{V}_s$ denote the rates of change of the volumes, we have

$$\dot{V}_f = -(\dot{V}_l + \dot{V}_s), \quad (11)$$

$$\dot{V}_l = f(\dot{V}_l + \dot{V}_s), \quad (12)$$

$$\dot{V}_l = 4\pi(R_m - \delta_l)^2\dot{\delta}_l , \quad (13)$$

$$\dot{V}_s = 4\pi\delta_s^2\dot{\delta}_s , \quad (14)$$

Putting these equations together, we find

$$\dot{\delta}_l = -(\dot{E}_r - \dot{E}_c)S_1 f/D, \quad (15)$$

$$\dot{\delta}_s = -(\dot{E}_r - \dot{E}_c)S_2(1-f)/D, \quad (16)$$

$$\dot{T}_f = -DT_s(\delta_s)(\dot{E}_r - \dot{E}_c)S_2(1-f)/D, \quad (17)$$

where $S_1 = 4\pi\delta_s^2$, $S_2 = 4\pi(R_m - \delta_l)^2$, $D = -C_p\rho_f S_2 V_f(\delta_l, \delta_s)DT_s(\delta_s)\cdot(1\text{-}f) + L\rho_f S_1 S_2$, the volume of the magma ocean is $V_f(\delta_l, \delta_s) = 4\pi/3((R_m-\delta_l)^3 - \delta_s^3)$. And δ_f can always be specified by $\delta_f = R_m - \delta_l - \delta_s$.

We tabulate the parameter values in table 1.

Table 1. Parameter values.

orbital constants		initial orbital conditions	
m_e/m_{Sun}	3.0034398×10^{-6}	*semi-major axis*	$5R_E$ [c]
m_m/m_{Sun}	3.6949711×10^{-8}	*day length*	2.53 hr [c]
R_e	6371km	*Earth's obliquity*	0
R_m	1737 km	*Moon's obliquity*	0
$C_p/(m_e\cdot R_e^2)$	0.3308	*lunar inclination*	0
ω_p	2π rad·day^{-1}	*lunar eccentricity*	0.001
J_{2p}	0.00108263		
thermal constants		initial thermal conditions	
T_p	1550 °C	δ_l	5 km
C_p	1256 J kg^{-1} °K^{-1}	δ_f	110 km
L_p	4.187×10^5 J kg^{-1}	tidal parameters	
κ	1.0×10^{-6} m^2 s^{-1}	k_{2e}	0.299
ρ_l	2927 kg m^{-3}	Q_e	400
ρ_f	3000 kg m^{-3}	k_{2m}	Updated by δ_l.
f [a]	0.4	Q_m	Updated by lid thermal profile, Q_{mmin}, and Q_{mmax}.
μ_{lid} [b]	6.5×10^9 Pa		
Moon gravity	1.62 m s^{-2}	Q_{mmin}	20
Moon surface temperature	280 °K	Q_{mmax}	Fit to give the initial A value.

[a] f is the plagioclase crystal proportion in magma ocean solidification.
[b] μ_{lid} is the rigidity of the lid.
[c] The combination of $5R_e$ and 2.53 hr is equivalent to the combination of $3.5R_e$ and 2.5 hr. We use $5R_e$ and 2.53 hr in order to save some computation time.

Results

We made simulations over a range of parameters. The variation of tidal parameters can be characterized by the A parameter

$$A = (k_{2m}/k_{2e})(Q_m/Q_e)^{-1}(m_e/m_m)^2(R_m/R_e)^5, \quad (18)$$

which is a measure of the relative dissipation in the Earth and in the Moon.

Fig. 1 shows the angular momentum of the Earth-Moon system when the Earth-Moon distance reaches 8.5 R_e, at which point the system would have exited the limit cycle or the evection resonance if previously captured by either, versus the initial A parameter of the system. It also shows the maximum eccentricity reached in each run. For comparison, we also show the results for a non-thermally-coupled orbital model on the same figure. When the system is set such that

the A parameter computed from the initial thermal state is small, in the range for evection resonance in the non-thermally-coupled model, the system does not lose angular momentum to a noticeable amount. The maximum eccentricity is 1.5-2 times smaller than that of the non-thermally-coupled counterpart, which indicates that the system does not stay long enough in the evection resonance for the eccentricity to be fully raised. On the other hand, when the initial A parameter falls in the range for the occurrence of the limit cycle, almost the same angular momentum is lost in the thermally coupled model as in the non-thermally-coupled model, and the maximum eccentricity is also similar. Even though the all final angular momenta for the limit cycle runs are larger than the current value by some difference, we will see that the difference grows progressively smaller if we use larger Q_e values (Fig. 5).

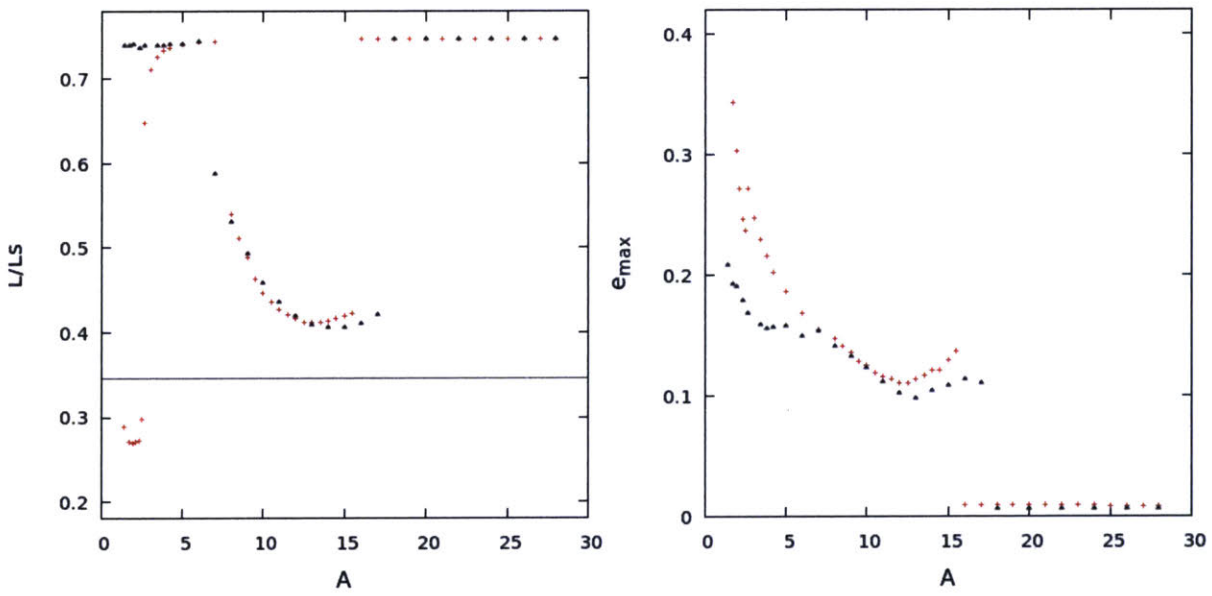

Fig. 1. Angular momentum of the Earth-Moon system when the Earth-Moon distance reaches $8.5R_e$ (left) and the maximum eccentricity in each run (right) versus: (black points) the initial A parameter, for thermal-orbital coupled simulations; (red crosses) the A parameter, for non-thermally-coupled simulations. The unit of angular momentum is $L_s = C(Gm_eR_e^{-3})^{1/2}$, where C is Earth's largest moment of inertia (current value). The black line is the current value of the system's angular momentum.

First consider a case where the system is captured into the evection resonance. Fig. 2 shows the details of evolution for a run with the initial $A = 1.74$. The system gets captured in the evection resonance at $t = 38$ thousand years (ky). Then the evection angle starts to oscillate around $\pi/2$

rad, and the lunar orbital eccentricity rises rapidly. As tidal heating gets elevated, lid temperatures gradually increase, Q of the Moon decreases, and the A parameter grows gradually. After a time lag of ~12 ky, during which the excess heat builds up in the Moon, the increase of lid temperatures is accelerated, and the A parameter grows rapidly from less than 5 to ~110. The increase of A is mainly due to the decrease in Q_m, though k_{2m} also changes. Some layers' temperatures reach T_p, so partial melting and melt migration occur. At the same time of this rapid growth of the lid temperatures and the A parameter, the system escapes the evection resonance, and the eccentricity plunges to zero. The system's exit from the resonance is due to the A parameter growing out of the range suitable for the occurrence of the resonance as observed in the non-thermally-coupled model (Fig. 1). Then as A decreases to within the range of evection resonance (~5), the system enters the evection resonance a second time. The eccentricity growth is less rapid this time, and the duration is short (~20 ky), which are consistent with the non-thermally coupled model when A is near 5 (Fig. 1, right panel, red crosses). Compared to the corresponding run with the non-thermally-coupled model, in which the system stays in the evection resonance for ~600 ky and maintains an eccentricity of ~0.34 throughout the resonance, the system in this run attains a maximum eccentricity of just 0.2, and stays in the evection resonance for only 30 ky. Therefore, the amount of angular momentum loss is negligible.

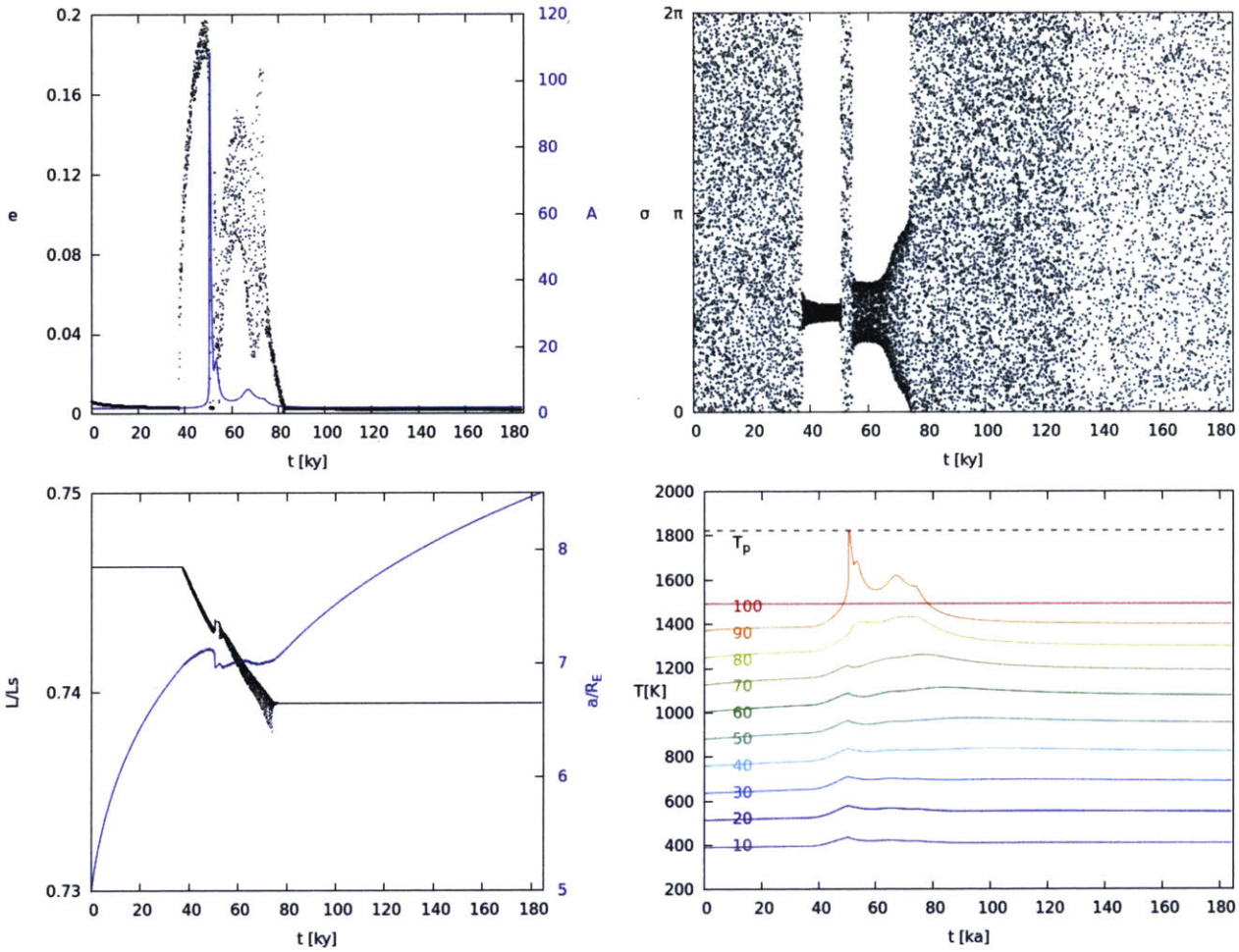

Fig. 2. The evolution of the system's A parameter (blue in upper left plot), the lunar orbit's eccentricity (black in upper left plot), the evection angle (upper right plot), the semi-major axis (blue in lower left plot), the system's angular momentum (black in lower left plot), and the temperatures of selected (the 10th, 20th, ... 100th) lid layers (lower right plot) for a thermal-orbital coupled simulation with an initial A parameter being 1.74.

The orbital and thermal processes in this run, such as the quick termination of the evection resonance and brief periods of partial melting and melt migration in the lid, are typical among the cases in which the system encounters the evection resonance.

Now consider a case where the system is captured into the limit cycle. Fig. 3 shows the details of evolution for a run with the initial A = 14. The system not only enters the limit cycle, but remains in the limit cycle for a long time and a significant amount of angular momentum is drained. Upon entry into the limit cycle at t = 37 ky, the lunar orbital eccentricity rapidly grows, as in the

evection resonance. But the eccentricity oscillates between ~0.01 and ~0.09, a range whose upper bound is considerably smaller than what would be achieved in the evection resonance (0.3-0.5 in the non-thermally coupled model). Since the rate of tidal heating is approximately proportional to e^2, heating in the Moon is significantly less severe, and the growth of the A parameter is limited. As the A parameter increases, the system is still retained in the limit cycle, and the upper bound of eccentricity is lowered, which is in agreement with the trend observed in the non-thermally-coupled simulations. Then the A parameter reaches a peak value and this is when the upper bound of eccentricity stops decreasing. After that, the A parameter begins to decrease, and both bounds of the eccentricity shift upward with the change of A parameter. In the later half of the limit cycle, though the eccentricity gets as large as when the limit cycle begins, the A parameter does not increase. This is because the lid is getting increasingly more efficient at emitting heat, both to space and to the magma ocean, after the short initial phase of A increase. The detailed behavior of A is explained below.

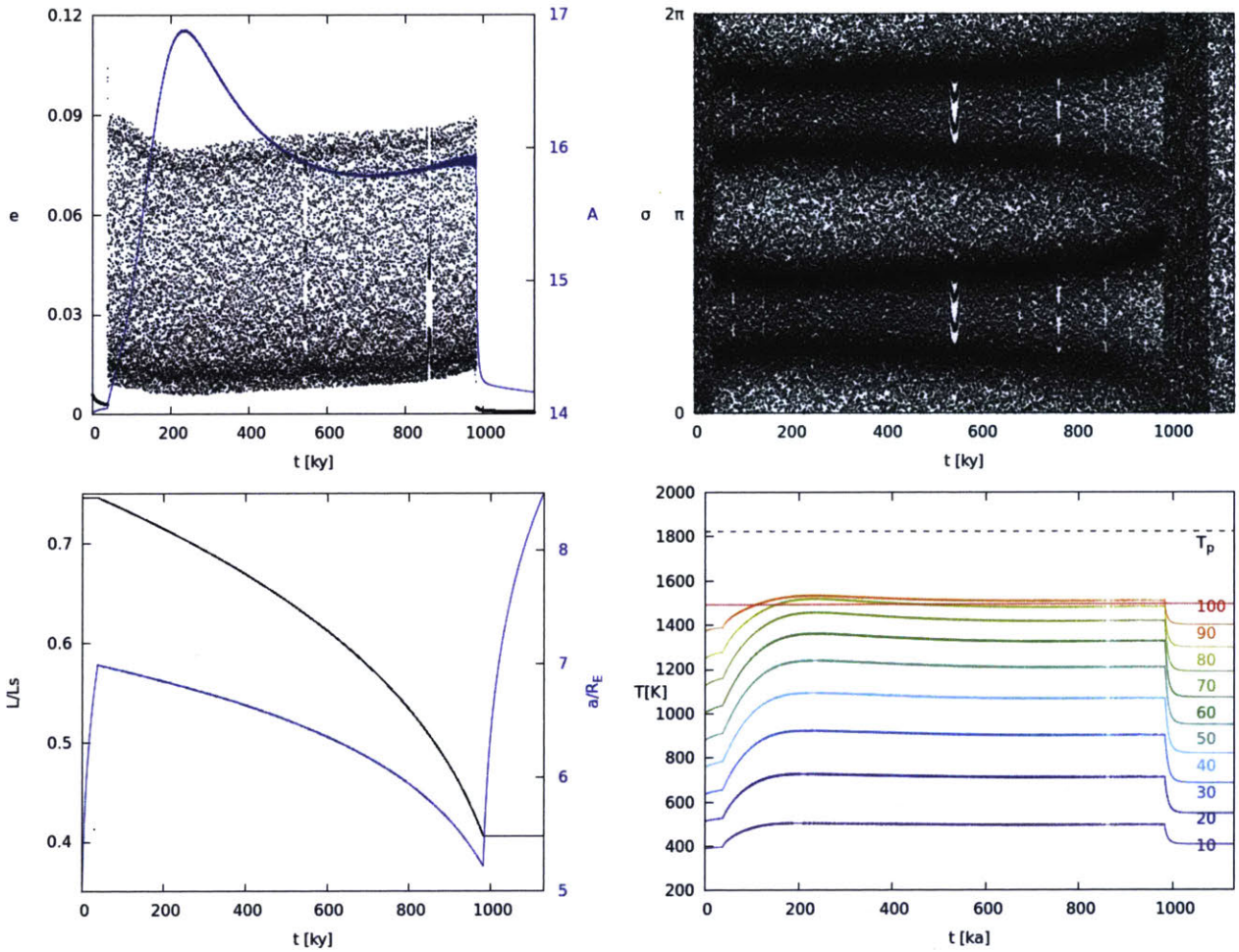

Fig. 3. The evolution of the same parameters as in Fig. 2, for a thermal-orbital coupled simulation with an initial *A* parameter being 14.

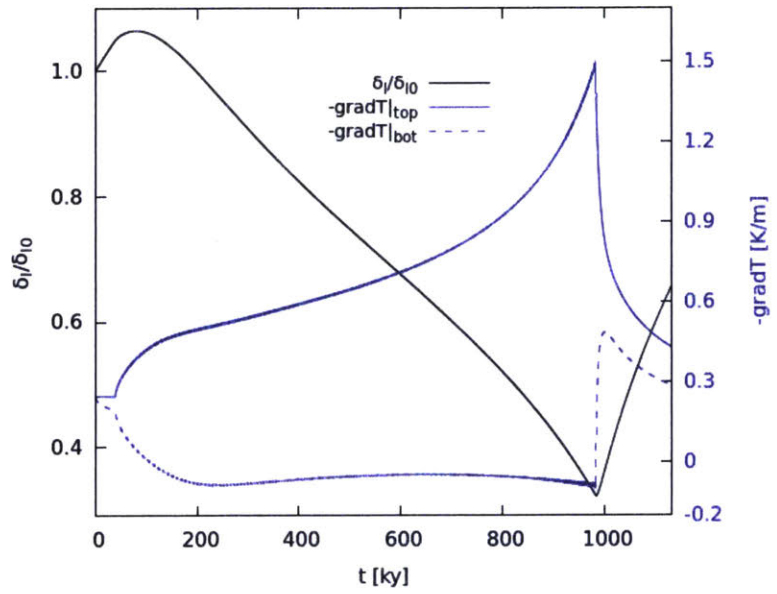

Fig. 4. The evolution of the lid thickness (black curve, left scale) and temperature gradients at the top (blue solid curve, right scale) and the bottom (blue dashed curve, right scale) of the lid, for the same simulation as in Fig. 3. The lid thickness is normalized with the initial thickness.

In detail, in the beginning of the limit cycle, the large eccentricities cause elevated tidal heating in the lid, decreasing Q_m and thus increasing the A parameter. But soon a maximum A value is reached, as the result of the combination of four negative feedbacks: (a) as A increases, both bounds of the eccentricity's oscillation decrease, leading to less rapid deposit of tidal heat in the lid; (b) as the temperatures of lid layers near the surface increase while the surface temperature stays constant at the equilibrium temperature, the negative temperature gradient at the surface and thus the heat flux to space increase; (c) as the temperatures of the bottom layers rise above the magma ocean temperature, heat flux switches direction so that now the lid loses some heat to the magma ocean; (d) as the heat flux at the lid base switches direction, according to equation (15), the lid begins to thin, while the temperatures of each layer continues to increase, so the effects of (b) and (c) get strengthened.

After A reaches the maximum, the lid continues to thin as the bottom layers continue to be hotter than the magma ocean. So even though the lid temperatures have stopped increasing, (d) continues at work, strengthening (b). Then the rate of heat loss from the lid, now dominated by (d) and (b), exceeds the rate of heat deposit in the lid, and the lid temperatures begin to decrease,

causing the A parameter to decrease, too. But as A decreases, the range of eccentricity oscillation gets to higher values, thus slowing down the rate of decrease of A.

In the later half the limit cycle, two opposing mechanisms work simultaneously: (i) the thinning of the lid leads to an increasing rate of heat loss from the lid mainly through (d) and (b), and (ii) the resultant decrease of A leads to an increasing rate of tidal heating in the lid (through increase eccentricities) which slows down the decrease of A, acting as a negative feedback on (i). The result is that A approaches an asymptotic value, as shown in Fig. 3.

The system remains in the limit cycle in the whole process even though the A parameter changes, allowing the continued draining of angular momentum from the Earth-Moon system. This robustness is partly attributed to the range of A parameter that allows the occurrence and maintenance of the limit cycle being much wider than that for the evection resonance.

Discussion and Conclusion

We also carried out simulations with Q_e being 200, 300 and 500, and other parameters kept the same. Results are shown in Fig. 5 as angular momentum versus the initial A parameter. We see that at all Q_e values there is no significant angular momentum decrease in the evection resonance region (A in 1-3), consistent with what we observed for the Q_e = 400 case. The results also show that when a smaller Q_e (300) is used, the limit cycle is still encountered, but over a smaller range of parameters. When Q_e is further decreased to 200, no observable angular momentum decrease occurs, indicating the absence of the system's capture in the limit cycle. This trend illustrates the importance of Q_e in the Earth-Moon system's early evolution: Q_e controls the rate of Earth-Moon separation, and the limit cycle, as well as resonances, capture the system with a higher chance when the Moon is separating from the Earth at a lower rate. A small Q_e means larger tidal disturbing forces to the system, which makes it harder for the limit cycle to occur and to be maintained. Zahnle *et al.* (2007) preferred a large Q_e, which can better facilitate angular momentum loss in our model.

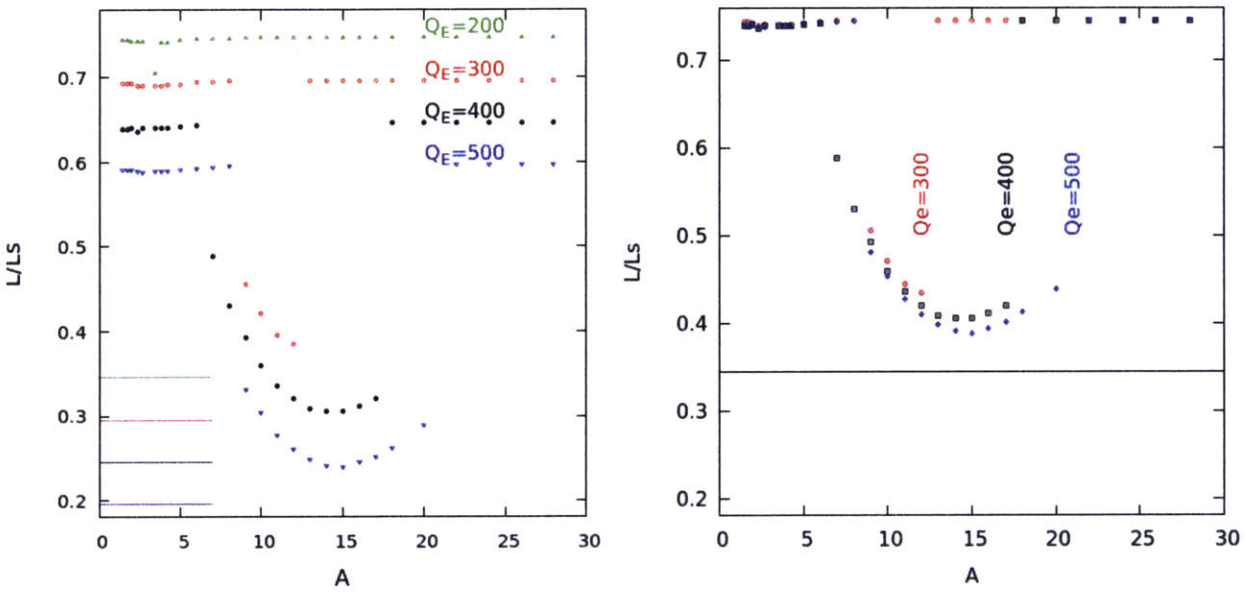

Fig. 5. The system's angular momentum when the Earth-Moon distance reaches 8.5 R_E, versus the initial A parameter, for the cases of Q_e=200 (green), Q_e=300 (red), Q_e=400 (black), Q_e=500 (blue). In the left panel, the Q_e=300, Q_e=400 and Q_e=500 points are offset by -0.05, -0.10 and -0.15 on the y-axis respectively to improve clarity, and the lines of current angular momentum are also offset accordingly. The right panel plots the same data without offset, and shows the tendency of smaller minimum final angular momentum achieved with increasing Q_e.

These results also demonstrate the importance of the A parameter in the early evolution of the Earth-Moon system. As long as the Earth-Moon separation is sufficiently slow (by assuming a sufficiently large Q_e), the system enters the limit cycle at the same A parameter values. Thus the detailed values of Q and k_2 are less important.

With the orbital evolution of the Earth-Moon system being coupled with the thermal evolution of the Moon, and beginning with a fast spinning Earth, the system can not lose its excess angular momentum through the evection resonance. When the system encounters the evection resonance, the eccentricity tends to be excited to large values (0.3-0.5), tidal heating in the lid becomes too intense to be efficiently conducted out, and partial melting and melt migration occur. The severe heating during the resonance induces rapid changes in the Moon's tidal properties and thus in the tidal accelerations, forcing the system to exit the resonance soon after it enters the resonance. In contrast, due to the lower eccentricities and the effects of feedback mechanisms that reduce the net heating in the lid, the limit cycle mechanism works stably over

extended periods of time, and successfully reduces the Earth-Moon system's angular momentum to a value that is near the current value over a wide range of parameters. Therefore, we conclude that if the Moon formed in a giant impact scenario that leaves the early Earth spinning much faster than is deduced from the current Earth-Moon's angular momentum, the limit cycle is a viable mechanism to have removed the excess angular momentum.

Chapter 4

The role of tidal heating on the development of the magmatic asymmetry of the Moon

ZhenLiang Tian, Maria T. Zuber

Abstract

The majority of lunar mare basalts have been emplaced on the nearside of the Moon. Previous studies proposed that this hemispheric asymmetric magmatic distribution could be a result of cumulative radiogenic heating in the deep lunar interior and later the ascension of a spherical harmonic degree-1 diapir in the mantle. However, why the diapir occurred on the nearside of the Moon remains unexplained. In this study we assess the possible role of tidal heating in producing the magmatic asymmetry. We approximate the Moon assuming a solid mantle overlying a liquid interior, and analyze the lateral distribution of degree-2 and degree-3 tidal heating in the lunar mantle. From the calculations, we conclude that either tidal heating could not have contributed to the occurrence of the diapir on the nearside, or the spherically symmetric shape assumed in the derivation of tidal heating does not correctly represent the Moon.

Introduction

The Moon exhibits a hemispheric asymmetry in the distribution of mare basalts. The overwhelming majority of the volume of the maria is on the lunar nearside. At first glance, it appeared that the mare basalts occur at the topographically low regions (e.g. Kaula, 1974). However, after the acquisition of the global topographic data (Zuber *et al.*, 1994; Smith *et al.*, 2016), it is recognized that many topographically low regions, most noticeably the South Pole-Aitken basin, do not contain abundant basalt emplacements. It is then more likely that the asymmetric distribution of maria indicates a fundamental asymmetry in lunar mantle activity. The nearside mantle has experienced relatively elevated partial melting during the lunar history, expressed in the form of mare distribution on the surface. Then why is this asymmetry hemispheric in scale, and why is the melting activity centered on the nearside?

Previous models (Hess & Parmentier, 1995, Zhong *et al.*, 2000) proposed scenarios to explain the formation of spherical harmonic degree-1 pattern of the mare asymmetry. At the end of the lunar magma ocean solidification, the dense ilmenite ($FeTiO_3$)-rich cumulates (IC), which are the last cumulates in the crystallization sequence, lie beneath the latest liquids that are highly concentrated in heat-producing elements (urKREEP). The IC layer, together with the iron rich mafic cumulates, overlie the magnesium rich, first crystallized minerals which are then at the base of the mantle. This gravitationally unstable density profile soon leads to a large-scale overturn in the mantle, bringing the IC and the iron rich silicates to the bottom of the mantle. Some of the late stage, radioactive element rich liquid is entrained with the IC and also sinks. Then the mixed ilmenite cumulates (MIC) either form a lunar core or a dense, radioactive element rich layer surrounding the core. According to Rayleigh-Taylor instability analysis, the overturn occurs rapidly, on the order of several thousand years.

As a result of this global-scale overturn, a substantial fraction of the Moon's heat-producing elements is concentrated in the deepest regions of the lunar mantle. As time proceeds, radiogenic heat accumulates in or around the core, and the outward thermal conduction is slow due to the great depth. The growing temperature and the resulting gravitational buoyancy of the MIC finally drives its ascent through the mantle to relatively shallow depths. Decompression melting of the ascending MIC creates the mare volcanism in 200~600 My. In this scenario, a single, large diapir is likely, since the spherical harmonic degree-1 pattern has the most rapidly growing instability under a wide range of parameter space, as given by both Rayleigh-Taylor instability analysis and numerical simulations (Hess & Parmentier, 1995, Zhong *et al.*, 2000). Therefore, the hemispheric asymmetry of the mare basalt distribution can be simply the result of spherical harmonic degree-1 diapir ascension of the deep MIC, radioactive element rich material.

However, the second question remains not completely answered. Why did the diapir rise in the nearside of the lunar mantle? Laneuville *et al.* (2013) proposed that the concentration of mare volcanism on the nearside of the Moon could be a natural consequence of the mantle thermal evolution, provided that the Moon's bulk KREEPy material is concentrated in the nearside crust and upper mantle in the first place. However, they did not provide an explanation for the concentration of the KREEPy material.

In this study, we explore the feasibility of laterally heterogeneous tidal heating leading to the ascending diapir's occurrence in the nearside mantle. We expect the possibility that tidal deformation preferentially dissipates energy in the nearside mantle, raises the mantle temperatures, reduces the viscosity, and thus facilitates the mantle flow and diapir ascension. We follow Peale and Cassen's (1978) approach of analyzing the equilibrium strain and stress distribution in a synchronously rotating, layered spherically symmetric body in response to the tide-raising potential. With the strain rate derived from the rate of change of tidal potential, we calculate the distribution of the rate of energy dissipation. We automate the derivation process, and expand the analysis to spherical harmonic degree-3. Then we consider the scheme in the context of recent scenarios of lunar orbital evolution, and assess the importance of the contribution of tidal heating to the heterogeneity of lunar mantle thermal states in various situations.

Strain and dissipation analysis

In this section we solve the equilibrium displacement, strain and tidal dissipation distribution of a spherically symmetric layered body in response to tidal potentials. The Moon is modeled as a solid elastic mantle overlying a liquid core (Fig. 1). Both layers are assumed to be homogeneous, incompressible, and have the same density. The solid exterior layer has much higher shear rigidity than the interior ($\mu^E \gg \mu^l$). The elastic assumption is used for the purpose of deriving the equilibrium strain. Dissipation will be treated later by the introduction of a phase delay in the Moon's equilibrium elastic deformation. The derivation for the case of spherical harmonic degree-2 deformation and degree-2 tide-raising potential is given in the appendix. Here we only present the degree-3 case.

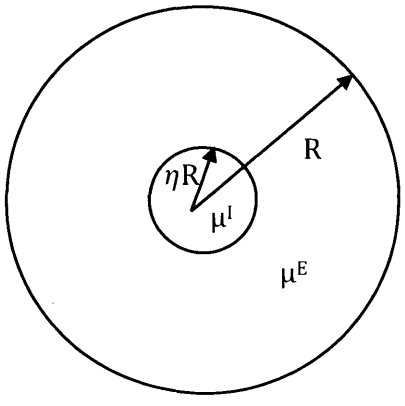

Fig. 1. Profile of the model Moon.

The Earth's tide-raising potential V can be expanded in spherical harmonics as:

$V = Gm_e/|\mathbf{r'}-\mathbf{r}| = Gm_e/r' \Sigma_n (r/r')^n P_n(\cos S)$,

where S is the angle between the direction of the Earth from the center of the Moon and the direction to the point of evaluation, r is the radius of the point of evaluation, r' is the distance between Earth and Moon. The geometry is illustrated in Fig. 2. With R as a shorthand for R_m, we define

$V_n = Gm_e/r' (r/r')^n P_n(\cos S)$,

$V_n^0 = Gm_e r'^{-n-1} R_m^n$,

and then

$V = \Sigma_n V_n^0 \cdot (r/R)^n P_n(\cos S)$.

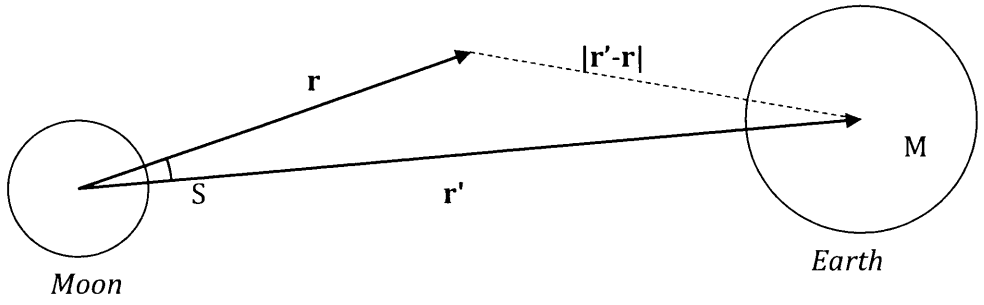

Fig. 2. Geometric relationships in the formulation of the tide-raising potential.

The deformation of the Moon also produces a potential. The total disturbing potential, U, is the sum of V and the potential produced by the Moon's distortion.

According to Love (1944; pp.257, eq.22),

$U = \Sigma_n U_n$

$= \Sigma_n [V_n + 3g/(2n+1) \cdot \Delta_n \cdot (r/R)^n]$,

where Δ_n is the degree-*n* radial displacement at the satellite's surface, g is the surface gravitational acceleration. The expression $\Delta_n = \Delta_n^0 P_n(\cos S)$. Then

$U_n = [V_n^0 + 3g/(2n+1) \cdot \Delta_n^0] \times (r/R)^n P_n(\cos S)$. (1)

Since the definition of the degree-*n* potential Love number k_n as $U_n = V_n + k_n \cdot V_n$ ($r \le R$), we have

$k_n = 3g/(2n+1)\ \Delta_n^0/V_n^0$. (2)

To establish the equation of equilibrium displacement, we need to analyze the forces in the satellite in the presence of a gravitational perturbation. The forces are:

(i) hydrostatic pressure ($-p_0$, p_0 is positive when the pressure is compressive);

(ii) satellite's self gravitational acceleration when unperturbed ($-g_r \hat{r}$);

(iii) stress caused by tidal distortion ($\overline{\overline{X}}$);

(iv) forces from the total disturbing potential (∇U).

Forces (i) and (ii) satisfy (as when the satellite is unperturbed):

$-\nabla p_0 - \rho g_r \hat{r} = 0$

Forces (i), (ii), (iii) and (iv) satisfy the equilibrium equation (Love 1944, pp.257, eq.23):

$-\nabla p_0 + \nabla \cdot \overline{\overline{X}} - \rho g_r \hat{r} + \rho \nabla U = 0$

and the two equations yield

$\nabla \cdot \overline{\overline{X}} + \rho \nabla U = 0$.

In Cartesian coordinates, the *x* component is:

$\partial_x X_{xx} + \partial_y X_{xy} + \partial_z X_{xz} + \rho \cdot \partial_x U = 0$. (3)

Since $X_{ij} = -p\delta_{ij} + 2\mu e_{ij}$, where p is the mean pressure due to tidal distortion, and in rectangular coordinates,

$e_{ij} = \frac{1}{2} (\partial_i u_j + \partial_j u_i)$, (4)

we can rewrite (1) as

$-\partial_x(p-\rho U) + \mu(\partial_x\partial_x + \partial_y\partial_y + \partial_z\partial_z)u_x + \mu\partial_x(\partial_x u_x + \partial_y u_y + \partial_z u_z) = 0$. (5)

The assumption of incompressibility gives

$\nabla \cdot \vec{u} = 0$ (6)

We define

$P = p - \rho U$, (7)

and then (5) and (6) give

$-\nabla P + \mu \nabla^2 \vec{u} = 0$. (8)

Since μ is constant in each layer, (1), (6) and (7) imply that P is a harmonic function (*i.e.*, $\nabla^2 P = 0$). Then (8) can be expanded as:

$-\nabla P_{n\pm} + \mu \nabla^2 \overrightarrow{u_{n\pm}} = 0$, (9)

where

$P_{n+} = P^0_{n+}(r/R)^n P_n(\cos S) = p_{n+} - \rho U_n$,

$P_{n-} = P^0_{n-}(r/R)^{-n-1} P_n(\cos S) = p_{n-}$

in the outer layer, and

$P_{n+} = P^0_{In}(r/R)^n P_n(\cos S)$,

$P_{n-} = 0$

in the inner layer. Equation (9) is the expression for equilibrium displacement.

A particular solution is given by Love (1944; pp. 258):

$\overrightarrow{u_{P3\pm}} = A_{3\pm} r^2 \nabla P_{3\pm} + B_{3\pm} \vec{r} P_{3\pm}$

where $A_{3+} = 1/12\ \mu^{-1}$, $B_{3+} = -1/12\ \mu^{-1}$, $A_{3-} = -1/30\ \mu^{-1}$, $B_{3-} = 4/15\ \mu^{-1}$,

where μ is the rigidity of whichever zone is under consideration. We use μ^E to denote the rigidity of the outer layer and μ^I for the inner layer.

Following Peale and Cassen 1978, we take the homogeneous solution to be

$\overrightarrow{u_{H3\pm}} = \nabla \times (\vec{r} \times \nabla \Phi_{3\pm})$

where $\Phi_{3\pm}$ is any harmonic function. The harmonic coefficients Φ^0_{3+}, Φ^0_{3-} and Φ^0_{I3} are defined similarly to those for $P_{3\pm}$.

The complete degree-3 solution is

$\overrightarrow{u_3} = \overrightarrow{u_{3+}} + \overrightarrow{u_{3-}}$

$\overrightarrow{u_{3\pm}} = A_{3\pm} r^2 \nabla^2 P_{3\pm} + B_{3\pm} \vec{r} P_{3\pm} - \nabla(\Phi_{3\pm} + \vec{r} \cdot \nabla \Phi_{3\pm})$. (10)

The boundary conditions are: (i) the total traction vanishes at the satellite's deformed surface; (ii) the total traction is continuous at the boundary between the two layers; and (iii) the displacement components are also continuous at the boundary. Expressing these conditions on traction and displacement using the coefficients $\Phi_{3\pm}{}^0$, $\Phi_{I3}{}^0$, $P_{3\pm}{}^0$, $P_{I3}{}^0$, $\Delta_3{}^0$ as defined above, we obtain a system of linear equations in terms of these coefficients. Solving the equilibrium displacement and strain is then equivalent to solving for these coefficients. The matrix representation of the equations for $\mu^F \Phi_{3+}{}^0$, $\mu^E \Phi_{3-}{}^0$, $R^2 P_{3+}{}^0$, $R^2 P_{3-}{}^0$, $\mu^I \Phi_{I3}{}^0$, $R^2 P_{I3}{}^0$, and $\mu^E R \Delta_3{}^0$ is:

-48	120	1/3	-17/5	0	0	$\frac{4}{7}\frac{\rho g R}{\mu^E}$	$\rho R^2 V_2^0$
-16	-30	5/12	8/15	0	0	0	0
$-12\eta^3$	$-12\eta^{-4}$	$\frac{1}{6}\eta^5$	$\frac{2}{5}\eta^{-2}$	$12\eta^3\beta$	$\frac{-1}{6}\eta^5\beta$	0	0
$-4\eta^3$	$3\eta^{-4}$	$\eta^5/12$	$-\eta^{-2}/30$	$4\eta^3\beta$	$\frac{-1}{12}\eta^5\beta$	0	0
$-16\eta^3$	$-30\eta^{-4}$	$\frac{5}{12}\eta^5$	$\frac{8}{15}\eta^{-2}$	$16\eta^3$	$-\frac{5}{12}\eta^5$	0	0
$-48\eta^3$	$120\eta^{-4}$	$\eta^5/3$	$\frac{-17}{5}\eta^{-2}$	$48\eta^3$	$-\eta^5/3$	0	0
-12	-12	1/6	2/5	0	0	-1	0

(11)

where $\eta=b/R$, b is the radius of the boundary between two layers, and $\beta=\mu^E/\mu^I$. Since the inner layer is liquid, we take the limit $\beta\to\infty$. Then the two rows in (11) dominated by β terms imply that $\mu^I\Phi_{I3}^0 = R^2P_{I3}^0 = 0$. So we ignore these two variables, and hereafter use μ to refer to μ^E since μ^I does not appear. The solutions are:

$$\mu\Phi_{2+}^0 = \mu R\Delta_3^0 (7/4\ \xi)^{-1} \cdot (-475\eta_{0to4} - 475\eta_{56} - 1435\eta_{78})/16,$$

$$\mu\Phi_{2-}^0 = \mu R\Delta_3^0 (7/4\ \xi)^{-1} \cdot (375\eta_{78} + 88\ \eta_{9to13})/6,$$

$$R^2P_{2+}^0 = \mu R\Delta_3^0 (7/4\ \xi)^{-1} \cdot (-1140\eta_{0to4} - 4500\eta_{56}),$$

$$R^2P_{2-}^0 = \mu R\Delta_3^0 (7/4\ \xi)^{-1} \cdot (2625\eta_{56} + 825\eta_{78} + 825\eta_{9to13}), \quad (12)$$

and

$$\mu R\Delta_2^0 = \rho R^2 V_3^0 (7/4\ \xi)/[\xi \cdot \rho g R/\mu + 5\lambda], \quad (13)$$

where

$$\xi = 95\eta_{0to4} + 375\eta_{56} + 375\eta_{78} + 88\eta_{9to13},$$

$$\lambda = 209\eta_{0to4} - 1800\eta_{56} + 1800\eta_{78} - 209\eta_{9to13},$$

$$\eta_{0to4} = 1+\eta+\eta^2+\eta^3+\eta^4,$$

$$\eta_{56} = \eta^5+\eta^6,$$

$$\eta_{78} = \eta^7+\eta^8,$$

$$\eta_{9to13} = \eta^9+\eta^{10}+\eta^{11}+\eta^{12}+\eta^{13}.$$

Substituting these results into (10), we obtain the equilibrium displacement. Then using (4) we obtain the equilibrium strain and stress. Both the stress and the equilibrium strain depend on r' and S (the angle between the line to the planet and the line to the point of evaluation). At a given fixed point in the satellite, r' and S change over time due to the planet's orbital motion and the satellite's rotation, so the stress and strain vary, too. Dissipation occurs due to the anelastic

flexing of the satellite, which is equivalent to a phase delay applied to the elastic deformation. We denote the phase-delayed strain as e^*_{ij}. The rate of energy dissipation per unit volume is

$$\dot{W} = X_{ij}\dot{e}^*_{ij} = -p\delta_{ij}\dot{e}^*_{ij} + 2\mu e_{ij}\dot{e}^*_{ij} \quad (14)$$

$$= -p\partial_t(\nabla\cdot\vec{u}^*) + 2\mu e_{ij}\dot{e}^*_{ij}$$

$$= 2\mu e_{ij}\dot{e}^*_{ij}.$$

This is the distribution of volumetric tidal heating. The expansion of this expression into different tidal frequencies and the evaluation of the phase lag at each frequency is similar to the appendix and we don't repeat that part of the derivation here.

Results

For spherical harmonic degree-2 tidal heating, with various assumptions regarding the liquid core size, orbital eccentricity, and the Moon's inclination, the lateral distributions of tidal heating at different depths do not show a concentration on the nearside. Actually, the distribution is symmetric about the 0° meridian, 90° meridian, and the equator.

As an example for eccentricity dominated tidal heating, we show the results for the case when the Earth-Moon separation is $5R_e$, the core radius is 0.1R, the orbital eccentricity is 0.1, and the inclination is 0, in Fig. 3. At all depths of the mantle, the maximum heating is near the polar region. At depths near the core (r=0.15R), there is a local maximum at the 90° longitude of the equatorial region. None of the depths shows concentrated heating in the sub-Earth point.

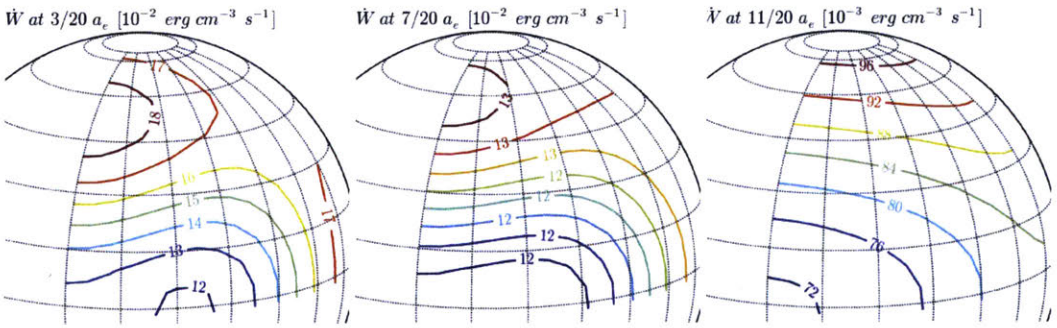

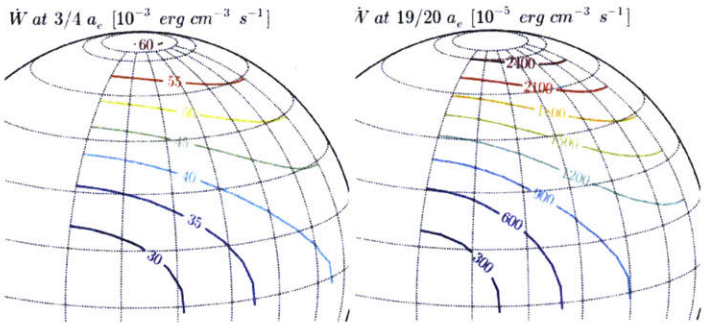

Fig. 3. The lateral distribution of degree-2 tidal heating at r=0.15R, 0.35R, 0.55R, 0.75R, 0.95R. η=0.1, e=0.1, *i*=0, a=5R_e. Since the distribution is symmetrical about the equator, 0° and 90° meridians, only one quadrant is plotted.

We also show an example for the inclination dominated tidal heating. Fig. 4 shows the results for the case when the Earth-Moon separation is 5R_e, the core radius is 0.1R, the orbital eccentricity is 0, and the inclination is 30°. At all depths, the maximum heating is at the 90° longitude of the equatorial region. This pattern does not favor the diapir to ascend in the nearside mantle, either.

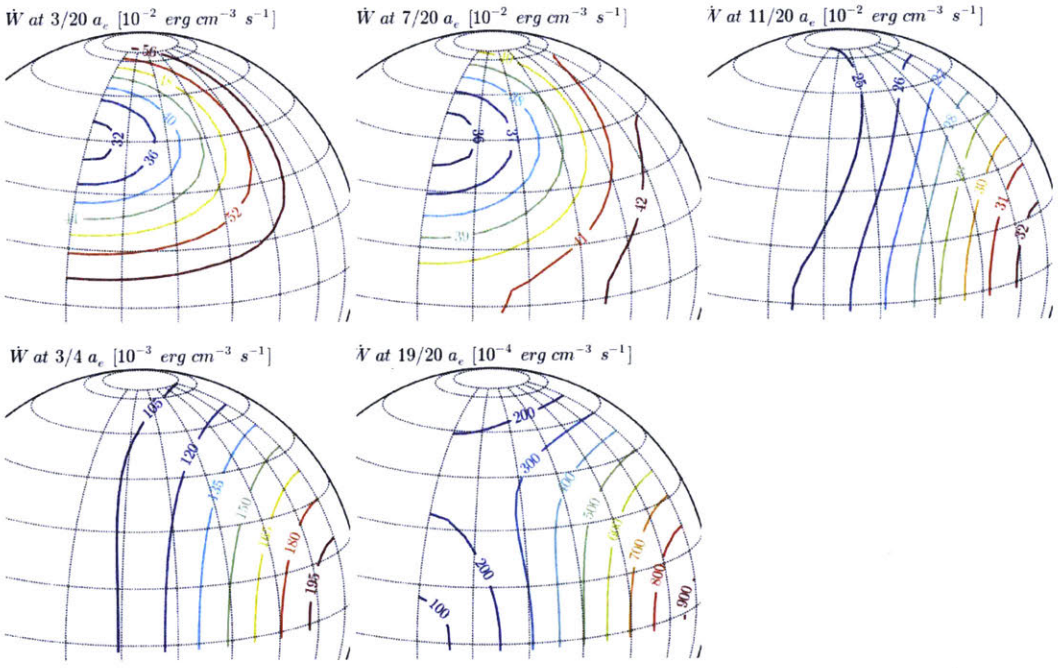

Fig. 4. The lateral distribution of degree-2 tidal heating at r=0.15R, 0.35R, 0.55R, 0.75R, 0.95R. η=0.1, e=0, *i*=30°, a=5R_e.

For the degree-3 tidal heating, the eccentricity dominated heating is concentrated on the nearside at most of the depths. However, the magnitude of the heating is ~3 orders of magnitude smaller than the degree-2 heating. This is simply because the degree-*n* heating rate $\dot{W}_n$ has the factor $R^{2n} \cdot r'^{-2n-2}$, as dictated by the $R^n \cdot r'^{-n-1}$ factor in V_n^0 in both X_{ij} and $\dot{e}^*_{ij}$. $(R/r')^2 = (1737\text{km}/(5*6371))^2 = 3e^{-3}$. Therefore $\dot{W}_{n+1}$ is $\sim 10^{-3}$ that of $\dot{W}_n$. The well-developed degree-3 pattern of concentrated tidal heating in the nearside would not have any effect on the location of the diapir because of its small magnitude.

Fig. 5 and 6 show the eccentricity dominated (e=0.1, *i*=0) and inclination dominated (e=0, *i*=30°) degree-3 tidal heating distribution when the Earth-Moon separation is $5R_e$ and the core radius is 0.1R.

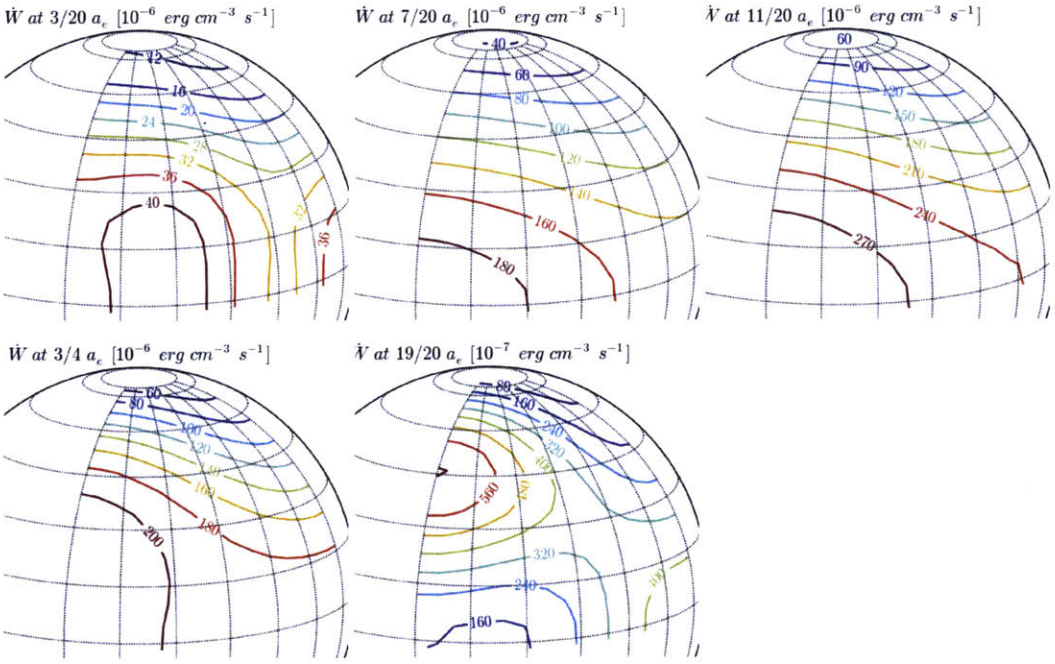

Fig. 5. The lateral distribution of degree-3 tidal heating at r=0.15R, 0.35R, 0.55R, 0.75R, 0.95R. η=0.1, e=0.1, *i*=0, a=5R_e.

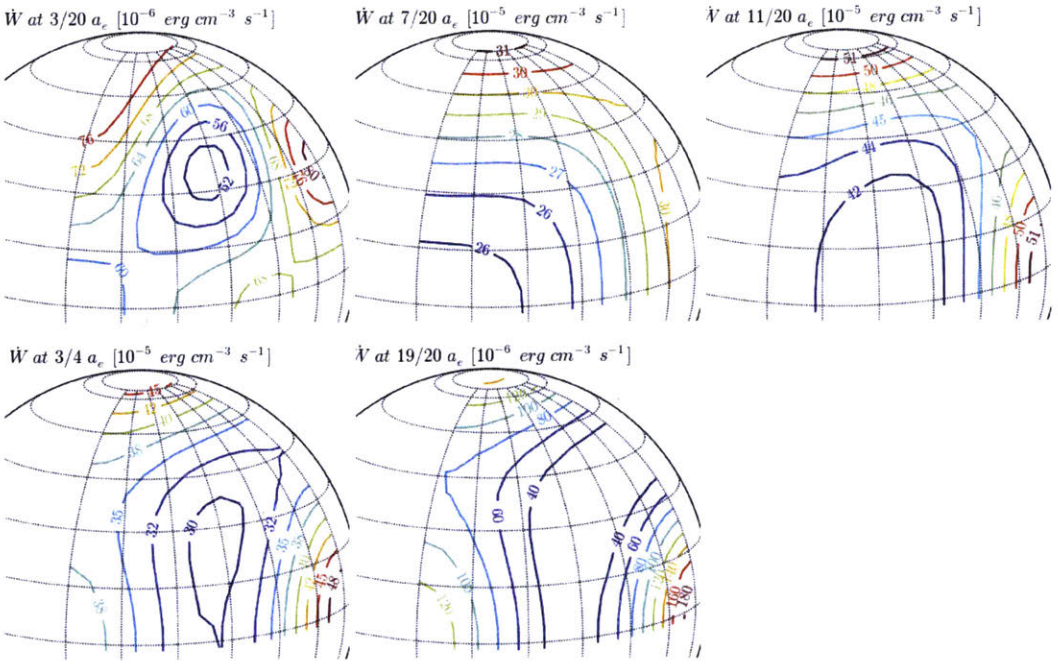

Fig. 6. The lateral distribution of degree-3 tidal heating at r=0.15R, 0.35R, 0.55R, 0.75R, 0.95R. η=0.1, e=0, *i*=30°, a=5R_e.

Discussion and conclusion

With the spherically symmetric geometry assumed for the Moon, it is not possible that heterogeneous tidal heating in the lunar mantle would favor and trigger the proposed degree-1 diapir ascension in the lunar nearside. Tidal heating in the Moon has always been dominated by the degree-2 component. The degree-2 tidal heating, under various assumptions of core radii, orbital eccentricities and inclinations, does not work to concentrate energy dissipation on the nearside or around the sub-Earth point mantle.

We conclude that either lunar tidal heating does not play a role in determining the location of the diapir ascension proposed by Zhong *et al.* (2000), or the spherically symmetric model's deformation scheme does not apply to the Moon.

Conclusions and Implications

This thesis makes the following conclusions:

1. The weak, axisymmetric, and offset magnetic field of Mercury can be produced by a dynamo with (i) a stably stratified layer (chemical or thermal) at the top of Mercury's large core, and (ii) a spherical harmonic degree-1 north-south asymmetric heat flux at the core-mantle boundary, which is consistent with the ancient large expanse of northern volcanic plains.
2. In Moon-forming giant impact scenarios that left the Earth spinning much faster than allowed by the current angular momentum of the Earth-Moon system, the evection resonance cannot work stably to reduce the system's angular momentum for the high eccentricities would have soon changed the Moon's tidal parameters and destabilize the resonance.
3. The limit cycle related to the evection resonance is the most viable mechanism for draining the Earth-Moon system angular momentum. It raises the orbital eccentricities only to limited values, so does not substantially change the lunar plagioclase lid's temperatures nor the Moon's tidal properties.
4. The limit cycle can be met and maintained over a wide range of parameters. A larger Q of the Earth will result in a wider range for the occurrence of the limit cycle. Therefore, a large Q of the Earth in the system's early history facilitates the system's angular momentum loss.
5. Assuming a spherically symmetric geometry of the Moon, tidal heating does not facilitate the occurrence of the degree-1 diapir ascension in the mantle and the concentration of mare basalts on the nearside of the Moon. This means that either tidal heating has never been an important factor in determining the Moon's asymmetry, or the spherically symmetric geometry fails to represent the Moon in the tidal heating analysis.

These conclusions have the following implications:

1. The Mercury dynamo results favor either a chemical or a thermal stratified layer. A possible liquid FeS stratification on the top of the core is consistent with a solid FeS layer at the bottom of Mercury's silicate mantle. The solid FeS layer was once proposed to explain the high bulk density of the solid shell of Mercury, but later proven to be possible but not required. Our results provide additional motivation for considering the existence of such a layer. A high core sulfur concentration, along with the unexpected high sulfur content detected on Mercury's

surface, strongly supports a reducing environment for Mercury's formation, and indicates the lack of strong heating and little volatile loss during the process.

2. The Mercury dynamo results favor a higher core-mantle boundary heat flux in the northern hemisphere than in the southern hemisphere. Such a pattern of heat flux is consistent with more rapid mantle convection and heat transfer in the northern hemisphere. Together with the ancient northern volcanic plains, which indicates more vigorous partial melting in the northern high latitudes then, the dynamo results imply a lower viscosity or higher average temperature in the northern hemisphere mantle. This north-south mantle thermal asymmetry can be a result of higher concentration of heat-producing elements in the northern hemisphere. It is interesting to see this asymmetry's effect on the planet's thermal history and more specifically, the history of Mercury's heat budget and core cooling.

3. The orbital-thermal evolution results of the early Moon suggest the existence of a non-negligible period of moderately elevated orbital eccentricity in early lunar orbital history, when a fast-spinning Earth is assumed at the beginning. With an Q_E set at 400, this period is about 1 My. But with a larger Q_E assumed (for e.g., Zahnle *et al.* (2007) proposed that the Q_E could be 100-1000 times larger than the commonly used value), this period will be proportionally longer. This opens up a new possibility for future lunar magma ocean solidification simulations. Long periods of moderately elevated eccentricity will effectively slow down the lid growth and elongate the complete solidification of the magma ocean. This possibility can help reconcile the disagreement between the modeled solidification time (~20 My) and the much broader range of measured anorthosite samples (~200 My) (Elkins-Tanton *et al.*, 2011).

Appendix

tidal heating in a synchronously rotating, two-layered satellite

The issue of tidal heating in a shell has been studies by previous investigators (Peale and Cassen, 1978, Peale *et al.*, 1979, Wahr *et al.*, 2006, Meyer *et al.*, 2010, Beuthe, 2013). For convenience, we derive the expression of degree-2 tidal heating in synchronously rotating, two-layered satellite. The solid exterior layer of the satellite has a much higher shear rigidity than the liquid interior layer ($\mu^E \gg \mu^I$). Both layers are incompressible and have the same density. We use the constant-Q Darwin-Kaula formulation to model the tide. In part 1, we derive the equations of the equilibrium displacement in the satellite and the boundary conditions. In part 2, we solve the displacement field and derive the equilibrium strain. In part 3, we derive tidal heating as a function of position in the satellite, the angle-averaged heating at a given radius, and the total heating in the outer solid layer of the satellite.

1: equation of displacement, boundary conditions

To establish the equation of the equilibrium displacement, we need to analyze the forces in the satellite in the presence of a gravitational perturber. The forces are:
(i) hydrostatic pressure ($-p_0$, p_0 is positive when the pressure is compressive);
(ii) satellite's self gravitational acceleration when unperturbed ($-g_r \hat{r}$);
(iii) stress caused by tidal distortion ($\overline{\overline{X}}$);
(iv) forces from the total disturbing potential (∇U, U is defined after equation (a1)).

(i), (ii) satisfy (as when the satellite is unperturbed):

$-\nabla p_0 - \rho g_r \hat{r} = 0$

(i), (ii), (iii), (iv) satisfy the equilibrium equation (Love 1944, pp.257, eq.23):

$-\nabla p_0 + \nabla \cdot \overline{\overline{X}} - \rho g_r \hat{r} + \rho \nabla U = 0$

the two equations give

$\nabla \cdot \overline{\overline{X}} + \rho \nabla U = 0.$

In Cartesian coordinates, the *x* component is:

$$\partial_x X_{xx} + \partial_y X_{xy} + \partial_z X_{xz} + \rho \cdot \partial_x U = 0 \qquad \text{(a1)}$$

U, the total disturbing potential, is the sum of the perturber's disturbing potential and the potential associated with the satellite's distortion. It can be spherical harmonically expanded. According to Love (1944; pp.257, eq.22),

$U = \Sigma_n U_n$

$= \Sigma_n [\, V_n + 3g/(2n+1) \cdot \Delta_n \cdot (r/R)^n \,],$

where Δ_n is the degree-*n* radial displacement at the satellite's surface, g is the surface gravitational acceleration, r is the radius of the point of evaluation, and R is the satellite's radius.

$V_n = GM(r/r')^n P_n(\cos S),$

where M is the mass of the planet, S is the angle between the direction of the perturber from the center of the satellite and the direction to the point of evaluation, r' is the distance between the satellite and the planet. Define

$V_n^0 = GMr'^{-n-1}R^n$, then

$V_n = V_n^0 \cdot (r/R)^n P_n(\cos S)$, and the corresponding surface radial displacement takes the form

$\Delta_n = \Delta_n^0 P_n(\cos S)$. So

$U_n = [V_n^0 + 3g/(2n+1)\cdot\Delta_n^0]$

$\times(r/R)^n P_n(\cos S)$. (a2)

With the definition of the degree *n* potential Love number k_n as

$U_n = V_n + k_n \cdot V_n$ (where $r \le R$),

we have

$k_n = 3g/(2n+1)\,\Delta_n^0/V_n^0$. (a3)

Now we relate (1) to the displacement field. Since

$X_{ij} = -p\delta_{ij} + 2\mu e_{ij}$, (a4)

where p is the mean pressure due to tidal distortion, and in rectangular coordinates,

$e_{ij} = \frac{1}{2}(\partial_i u_j + \partial_j u_i)$,

we can rewrite (1) as

$-\partial_x(p-\rho U) + \mu(\partial_x\partial_x+\partial_y\partial_y+\partial_z\partial_z)u_x + \mu\partial_x(\partial_x u_x+\partial_y u_y+\partial_z u_z) = 0.$ (a5)

The incompressible assumption gives

$\nabla \cdot \vec{u} = 0$ (a6)

Define $P = p-\rho U$, (a7)

then (5) and (6) give

$-\nabla P + \mu\nabla^2\vec{u} = 0.$ (a8)

Since μ is constant in each layer, (a2), (a6) and (a8) imply that P is a harmonic function (*i.e.*, $\nabla^2 P = 0$). Then (a8) can be expanded as:

$-\nabla P_{n\pm} + \mu\nabla^2\overrightarrow{u_{n\pm}} = 0$, (a9)

where

$P_{n+} = P^0_{n+}(r/R)^n P_n(\cos S) = p_{n+} - \rho U_n$,

$P_{n-} = P^0_{n-}(r/R)^{-n-1} P_n(\cos S) = p_{n-}$

in the outer layer, and

$P_{n+} = P^0_{In}(r/R)^n P_n(\cos S)$,

$P_{n-} = 0$

in the inner layer.

A particular solution is given by Love (1944; p. 258):

$\overrightarrow{u_{Pn\pm}} = A_{n\pm} r^2 \nabla P_{n\pm} + B_{n\pm}\vec{r}\, P_{n\pm}$

where $A_{n\pm}$, $B_{n\pm}$ satisfy

$(4k_\pm+2)A_{n\pm} + 2B_{n\pm} = \mu^{-1}$,

$2k_\pm A_{n\pm} + (k_\pm+3)B_{n\pm} = 0$,

$k_+ = n$, $k_- = -(n+1)$,

$(A_{2+} = 5/42\ \mu^{-1}, B_{2+} = -2/21\ \mu^{-1}$,

$A_{2-} = 0, B_{2-} = 1/2\ \mu^{-1})$,

where μ is the rigidity of whichever zone is under consideration. We use μ^E to denote the rigidity of the outer layer and μ^I for the inner layer.

Following Peale and Cassen 1978, we take the homogeneous solution to be

$\overrightarrow{u_{Hn\pm}} = \nabla\times(\vec{r}\times\nabla\Phi_{n\pm})$

where $\Phi_{n\pm}$ is any harmonic function. The harmonic coefficients Φ^0_{n+}, Φ^0_{n-} and Φ^0_{1n} are defined similarly to those for $P_{n\pm}$.

The complete solution is

$$\vec{u_n} = \vec{u_{n+}} + \vec{u_{n-}}$$

$$\vec{u_{n\pm}} = A_{n\pm} r^2 \nabla^2 P_{n\pm} + B_{n\pm} \vec{r} P_{n\pm} - \nabla(\Phi_{n\pm} + \vec{r}\cdot\nabla\Phi_{n\pm}) \qquad \text{(a10)}$$

Now we specify the boundary conditions.
At the satellite's deformed surface, total traction vanishes:

$$(X_{rr} - p_0)|_{r=R} + \Delta\cdot[\partial_r(X_{rr} - p_0)]|_{r=R} = 0,$$

$$X_{r\theta}|_{r=R} + \Delta\cdot\partial_r X_{r\theta}|_{r=R} = 0,$$

$$X_{r\phi}|_{r=R} + \Delta\cdot\partial_r X_{r\phi}|_{r=R} = 0,$$

where Δ is the sum of Δ_n. Note that $p_0|_{r=R} = 0$, $\partial_r p_0 = -\rho g$. $X_{ri} = -p\delta_{ri} + 2\mu e_{ri}$, $p = O(\mu\cdot\Delta/R)$, $e_{ri} = O(\Delta/R)$, so $X_{ri} = O(\Delta/R)$, $\Delta\cdot\partial_r X_{ri}|_{r=R} = O(\Delta/R)^2$. Neglect terms of $O(\Delta R/R)^2$ and higher, we get

$$X_{rr}|_{r=R} + \rho g\Delta = 0, \qquad \text{(a11)}$$

$$X_{r\theta}|_{r=R} = 0. \qquad \text{(a12)}$$

The $X_{r\phi}$ equation is neglected because it gives the same constraint as the $X_{r\theta}$ equation.
The total traction is continuous at the boundary between the two layers:

$$(X_{rr} - p_0)|_{r=R} + \Delta\cdot[\partial_r(X_{rr} - p_0)]|_{r=b-} = (X_{rr} - p_0)|_{r=R} + \Delta\cdot[\partial_r(X_{rr} - p_0)]|_{r=b+},$$

$$X_{r\theta}|_{r=b-} + \Delta\cdot\partial_r X_{r\theta}|_{r=b-} = X_{r\theta}|_{r=b+} + \Delta\cdot\partial_r X_{r\theta}|_{r=b+}.$$

We assume the two layers have the same density, so $\partial_r p_0|_{r=b-} = \partial_r p_0|_{r=b+} = -\rho g$. Neglect of $O(\Delta R/R)^2$ and higher terms gives:

$$X_{rr}|_{r=b-} = X_{rr}|_{r=b+}, \qquad \text{(a13)}$$

$$X_{r\theta}|_{r=b-} = X_{r\theta}|_{r=b+}. \qquad \text{(a14)}$$

The displacement components are also continuous at the boundary:

$$u_r|_{r=b-} = u_r|_{r=b+}, \qquad \text{(a15)}$$

$$u_\theta|_{r=b-} = u_\theta|_{r=b+}. \qquad \text{(a16)}$$

We also have Δ being the radial displacement at r=R:

$$u_r|_{r=R} = \Delta. \qquad \text{(a17)}$$

2: solution of displacement and strain

We can transform the conditions on the traction to conditions on the displacement using the relation:

$$\mu^{-1} r\vec{X_r} = -\mu^{-1}(P+\rho U)\vec{r} + \nabla(\vec{r}\cdot\vec{u}) + (\vec{r}\cdot\nabla)\vec{u} - \vec{u}, \qquad \text{(a18)}\ [1]$$

---

[1] Proof: From (a25), (a26), (a4) and (a7), we have

$$X_{rr} = -(P+\rho U) + 2\mu\partial_r u_r,$$
$$X_{r\theta} = \mu(r\cdot\partial_r(r^{-1}u_\theta) + r^{-1}\partial_\theta u_r),$$
$$X_{r\phi} = \mu(r^{-1}\sin^{-1}\theta\cdot\partial_\phi u_r + r\cdot\partial_r(r^{-1}u_\phi)).$$

Since $\vec{X_r} = X_{rr}\hat{r} + X_{r\theta}\hat{\theta} + X_{r\phi}\hat{\phi}$, we get

$$\vec{X_r} + (P+\rho U)\hat{r} = 2\mu\partial_r u_r\hat{r} + \mu[r\partial_r(r^{-1}u_\theta) + r^{-1}\partial_\theta u_r]\hat{\theta} + \mu[r^{-1}\sin^{-1}\theta\cdot\partial_\phi u_r + r\partial_r(r^{-1}u_\phi)]\hat{\phi}.$$

where $\overrightarrow{X_r}=\overline{\overline{X}}\cdot\hat{r}$. Use of (a2), (a10) and (18) in boundary conditions (a11)~(a17) leads to a set of linear equations for $\mu^E\Phi_{2+}^0$, $\mu^E\Phi_{2-}^0$, $R^2P_{2+}^0$, $R^2P_{2-}^0$, $\mu^I\Phi_{I2}^0$, $R^2P_{I2}^0$, and $\mu^ER\Delta_2^0$. The matrix of coefficients is

-12	48	-1/7	-3	0	0	$\frac{2}{5}\frac{\rho gR}{\mu^E}$	$\rho R^2V_2^0$
-6	-16	8/21	½	0	0	0	0
$-12\eta^2$	$48\eta^{-3}$	$-\eta^4/7$	$-3\eta^{-1}$	$12\eta^2$	$\frac{1}{7}\eta^4$	0	0
$-6\eta^2$	$-16\eta^{-3}$	$\frac{8}{21}\eta^4$	$\frac{1}{2}\eta^{-1}$	$6\eta^2$	$\frac{-8}{21}\eta^4$	0	0
$-6\eta^2$	$-6\eta^3$	$\eta^4/7$	$\frac{1}{2}\eta^{-1}$	$6\eta^2\beta$	$\frac{-1}{7}\eta^4\beta$	0	0
$-3\eta^2$	$2\eta^{-3}$	$\frac{5}{42}\eta^4$	0	$3\eta^2\beta$	$\frac{-5}{42}\eta^4\beta$	0	0
-6	-6	1/7	½	0	0	-1	0

(a19)

where $\eta=b/R$, b is the radius of the boundary between two layers, and $\beta=\mu^E/\mu^I$. Since the inner layer is liquid, we take the limit $\beta\to\infty$. Then the two lines in (a19) dominated by β terms imply that $\mu^I\Phi_{I2}^0=R^2P_{I2}^0=0$. So we ignore these two variables, and hereafter use μ to refer to μ^E since μ^I does not appear. The solutions of the other variables are:

$$\mu\Phi_{2+}^0 = \mu R\Delta_2^0\,(5\xi)^{-1}\cdot(-32\eta_{012}-32\eta_{34}-60\eta_{56}),$$
$$\mu\Phi_{2-}^0 = \mu R\Delta_2^0\,(5\xi)^{-1}\cdot(32\eta_{56}+19/2\,\eta_{789}),$$
$$R^2P_{2+}^0 = \mu R\Delta_2^0\,(5\xi)^{-1}\cdot(-504\eta_{012}-1344\eta_{34}),$$
$$R^2P_{2-}^0 = \mu R\Delta_2^0\,(5\xi)^{-1}\cdot(640\eta_{34}+304\eta_{56}+304\eta_{789}),\qquad (a20)$$

and

$$\mu R\Delta_2^0 = \rho R^2V_2^0\,(5\xi)/[2\xi\cdot\rho gR/\mu+24\lambda],\qquad (a21)$$

where

$\xi = 24\eta_{012}+64\eta_{34}+64\eta_{56}+19\eta_{789}$,
$\lambda = 19\eta_{012}-56\eta_{34}+56\eta_{56}-19\eta_{789}$,
$\eta_{012} = 1+\eta+\eta^2$,
$\eta_{34} = \eta^3+\eta^4$,
$\eta_{56} = \eta^5+\eta^6$,
$\eta_{789} = \eta^7+\eta^8+\eta^9$.

From (a3) and (a21)

$$k_2 = 3g/5\,\Delta_2^0/V_2^0 = \frac{\frac{3}{2}\xi}{\xi+12\lambda\,\mu/(\rho gR)}.\qquad (a22)^2$$

Apply the relation: $r\partial_r(r^{-1}u_r) = -r^{-1}u_r+\partial_r u_r$, and multiply both sides with $\mu^{-1}r$, we get:

$\mu^{-1}r\overrightarrow{X_r}+\mu^{-1}(P+\rho U)\vec{r}$
$= r[\partial_r u_r\hat{r}+r^{-1}\partial_\theta u_r\hat{\theta}+r^{-1}\sin^{-1}\theta\cdot\partial_\phi u_r\hat{\phi}]$
$\quad +r\cdot u_r\hat{r}+r^2[\partial_r(r^{-1}u_r)\hat{r}+\partial_r(r^{-1}u_\theta)\hat{\theta}+\partial_r(r^{-1}u_\phi)\hat{\phi}]$
$= r(\nabla u_r+u_r\nabla r)+r^2\partial_r(r^{-1}\vec{u})$
$= \nabla(r\cdot u_r)-\vec{u}+r\partial_r\vec{u}$
$=\nabla(\vec{r}\cdot\vec{u})-\vec{u}+(\vec{r}\cdot\nabla)\vec{u}$.

(18) is proven.

[2] When $\eta=0$, we get $\xi=24$, $\lambda=19$, $k_2=\frac{3/2}{1+(19/2)\,\mu/(\rho gR)}$.

We note that $\mu R\Delta_2{}^0 = 5/3\ (g^{-1}\mu R k_2 V_2{}^0)$. Since $\mu\Phi_{2+}{}^0$, $\mu\Phi_{2-}{}^0$, $R^2P_{2+}{}^0$, $R^2P_{2-}{}^0$ are all ratios of $\mu R\Delta_2{}^0$, they are also ratios of $(g^{-1}\mu R k_2 V_2{}^0)$, and the ratios are functions of η, as shown in (a20).

Substitution of these coefficients into (a10) gives the displacement solution:

$$
\begin{aligned}
u_r &= Rg^{-1} k_2\alpha_1\ (r^{-1} V_2),\\
u_\theta &= Rg^{-1} k_2\alpha_2\ (r^{-1} \partial_\theta V_2),\\
u_\phi &= Rg^{-1} k_2\alpha_2\ (r^{-1} \sin^{-1}\theta\cdot\partial_\phi V_2),
\end{aligned}
\qquad \text{(a23)}
$$

where

$$
\begin{aligned}
\alpha_1 = 2/3\ \xi^{-1}\ [&(-96\eta_{56} - 57/2\ \eta_{789}) r_1{}^{-5}\\
&+(160\eta_{34} + 76\eta_{56} + 76\eta_{789}) r_1{}^{-3}\\
&+(96\eta_{012} + 96\eta_{34} + 180\eta_{56})\\
&+(-36\eta_{012} - 96\eta_{34}) r_1{}^2],\\
\alpha_2 = 2/3\ \xi^{-1}\ [&(32\eta_{56} + 19/2\ \eta_{789}) r_1{}^{-5}\\
&+(48\eta_{012} + 48\eta_{34} + 90\eta_{56})\\
&+(-30\eta_{012} - 80\eta_{34}) r_1{}^2\ ].
\end{aligned}
\qquad \text{(a24)}[3]
$$

The equilibrium strain is the spatial derivative of the equilibrium displacement. In Cartesian coordinates, $e_{ij} = \frac{1}{2}(\partial_i u_j + \partial_j u_i)$. In arbitrary curvilinear coordinates (α, β, γ), the relation between strain and displacement is

$$
\begin{aligned}
e_{\alpha\alpha} &= h_\alpha\partial_\alpha u_\alpha + h_\alpha h_\beta u_\beta\partial_\beta(1/h_\alpha) + h_\gamma h_\alpha u_\gamma\partial_\gamma(1/h_\alpha)\\
e_{\beta\beta} &= h_\beta\partial_\beta u_\beta + h_\beta h_\gamma u_\gamma\partial_\gamma(1/h_\beta) + h_\alpha h_\beta u_\alpha\partial_\alpha(1/h_\beta)\\
e_{\gamma\gamma} &= h_\gamma\partial_\gamma u_\gamma + h_\gamma h_\alpha u_\alpha\partial_\alpha(1/h_\gamma) + h_\beta h_\gamma u_\beta\partial_\beta(1/h_\gamma)\\
e_{\alpha\beta} &= \tfrac{1}{2}\ [h_\alpha/h_\beta\cdot\partial_\alpha(h_\beta u_\beta) + h_\beta/h_\alpha\cdot\partial_\beta(h_\alpha u_\alpha)]\\
e_{\beta\gamma} &= \tfrac{1}{2}\ [h_\beta/h_\gamma\cdot\partial_\beta(h_\gamma u_\gamma) + h_\gamma/h_\beta\cdot\partial_\gamma(h_\beta u_\beta)]\\
e_{\gamma\alpha} &= \tfrac{1}{2}\ [h_\gamma/h_\alpha\cdot\partial_\gamma(h_\alpha u_\alpha) + h_\alpha/h_\gamma\cdot\partial_\alpha(h_\gamma u_\gamma)]
\end{aligned}
\qquad \text{(a25)}
$$

where $h_\alpha = |\nabla\alpha|$, $h_\beta = |\nabla\beta|$, $h_\gamma = |\nabla\gamma|$.

In spherical coordinates (r, θ, ϕ),

$$h_r = 1,\ \ h_\theta = r^{-1},\ h_\phi = r^{-1}\sin^{-1}\theta. \qquad \text{(a26)}$$

Substitution of (a23) and (a26) in (a25) gives

$$
\begin{aligned}
e_{rr} &= Rg^{-1}k_2\cdot A\alpha_0\ ,\\
e_{\theta\theta} &= Rg^{-1}k_2\cdot (A\alpha_1 + B\alpha_2),\\
e_{\phi\phi} &= Rg^{-1}k_2\cdot (A\alpha_1 + C\alpha_2),\\
e_{r\theta} &= Rg^{-1}k_2\cdot D\alpha_3\ ,\\
e_{\theta\phi} &= Rg^{-1}k_2\cdot E\alpha_2\ ,\\
e_{r\phi} &= Rg^{-1}k_2\cdot H\alpha_3\ ,
\end{aligned}
\qquad \text{(a27)}
$$

where

$$
\begin{aligned}
A &= r^{-2} V_2 = GMr'^{-3} P_2(\cos S),\\
B &= \partial_\theta\partial_\theta A,\\
C &= \sin^{-2}\theta\cdot\partial_\phi\partial_\phi A + \cot\theta\cdot\partial_\theta A,\\
D &= \partial_\theta A,\\
E &= \sin^{-1}\theta\cdot\partial_\phi(\partial_\theta A - \cot\theta\cdot A),\\
H &= \sin^{-1}\theta\cdot\partial_\phi A,
\end{aligned}
\qquad \text{(a28)}
$$

which are all independent of r, and

$$
\begin{aligned}
\alpha_0 &= \partial_r(r\cdot\alpha_1)\\
&= 2/3\ \xi^{-1}\ [(384\eta_{56} + 114\eta_{789}) r_1{}^{-5}\\
&\quad +(-320\eta_{34} - 152\eta_{56} - 152\eta_{789}) r_1{}^{-3}\\
&\quad +(96\eta_{012} + 96\eta_{34} + 180\eta_{56})
\end{aligned}
$$

---

[3] When $\eta=0$, $\alpha_1 = 8/3 - r_1{}^2$, $\alpha_2 = 4/3 - 5/6\ r_1{}^2$. Note that $k_2\cdot\alpha_1$ is equivalent to $k_2'\cdot\alpha_2$ in Peale & Casen (1978) and Meyer (2010), and that $k_2\cdot\alpha_2$ is equivalent to their $k_2'\cdot\alpha_1$.

$$+(-108\eta_{012} -288\eta_{34})r_1^2],$$

$$\alpha_3 = \tfrac{1}{2}\,(r\partial_r\alpha_2 +\alpha_1)$$
$$= 2/3\ \xi^{-1}\,[(-128\eta_{56} -38\eta_{789})r_1^{-5}$$
$$+(80\eta_{34} +38\eta_{56} +38\eta_{789})r_1^{-3}$$
$$+(48\eta_{012} +48\eta_{34} +90\eta_{56})$$
$$+(-48\eta_{012} -128\eta_{34})r_1^2]. \quad (a29)^{4,5}$$

3: tidal heating distribution, total heating

As seen in (a27) and (a4), both the stress and the equilibrium strain depend on r' and S (the angle between the line to the planet and the line to the point of evaluation). At a given fixed point in the satellite, r' and S change over time due to the planet's orbital motion and the satellite's rotation, so the stress and strain vary, too. Dissipation occurs due to the anelastic flexation of the satellite, which is equivalent to a phase delay applied to the elastic deformation. We denote the phase-delayed strain as e^*_{ij}. The rate of energy dissipation per unit volume is

$$\dot{W} = X_{ij}\dot{e}^*_{ij} =-p\delta_{ij}\dot{e}^*_{ij} +2\mu e_{ij}\dot{e}^*_{ij}$$
$$=-p\partial_t(\nabla\cdot\vec{u}^*) +2\mu e_{ij}\dot{e}^*_{ij}$$
$$=2\mu e_{ij}\dot{e}^*_{ij}, \qquad (a30)$$

where the summation convention is used. The incompressible assumption is used. In spherical coordinates, substitution of (a27) into (a30) gives:

$$\dot{W} = 2\mu\, R^2 g^{-2} k_2^2$$
$$\times[A\dot{A}^*\alpha_0^2 +2A\dot{A}^*\alpha_1^2$$
$$+(A\dot{B}^*+B\dot{A}^*+A\dot{C}^*+C\dot{A}^*)\alpha_1\alpha_2$$
$$+(B\dot{B}^*+C\dot{C}^*+2E\dot{E}^*)\alpha_2^2$$
$$+2(D\dot{D}^*+H\dot{H}^*)\alpha_3^2]. \qquad (a31)$$

Now we can see the separation of $\dot{W}$'s dependence on radius and on the angles. The r-dependence is completely expressed in α_i, and the θ- and ϕ-dependences are expressed in $A\dot{A}^*$, $A\dot{B}^*$ ... A, B... functions are determined by the planet's distance and orientation relative to the satellite, and $\dot{A}^*$, $\dot{B}^*$ ... are determined by the planet's orbital motion, the satellite's rotation, and the phase lags in the satellite's tidal responses.

We take $A\dot{A}^*$ as an example to study the form of the angle-dependent part of $\dot{W}$. Let (θ', ϕ'), (θ, ϕ) denote the colatitude and longitude of the planet and the point of evaluation. ϕ' and ϕ are measured from a particular meridian of the satellite, which is an instantaneous inertia frame of reference (χ_1). According to the spherical harmonic addition theorem,

$$A = GMr'^{-3}\,\Sigma_{m=0}^{2}\, c_m P_{2m}(\cos\theta')P_{2m}(\cos\theta)\cos[m(\phi'-\phi)],$$

---

[4] When $\eta=0$, $\alpha_0 =8/3 -3r_1^2$, $\alpha_3 =4/3 -4/3r_1^2$.

[5] As a test, we compute values $k_2\cdot\alpha_i$ at particular parameter values, and compare the result with Peale & Cassen (1978) and Meyer *et al.* (2010). Take $\rho=3.34$, $g=162$, $R=1.738e^8$, $\mu=6.5e^{11}$ (in cgs).

For $\eta=0.5$,
$k_2\cdot\alpha_0 = 9.138e\text{-}3\ r_1^{-5} -3.233e\text{-}2\ r_1^{-3} +9.084e\text{-}2 -0.1135\ r_1^2$,
$k_2\cdot\alpha_1 = -2.284e\text{-}3r_1^{-5} +1.617e\text{-}2r_1^{-3} +9.084e\text{-}2 -3.784e\text{-}2r_1^2$,
$k_2\cdot\alpha_2 =\ 7.615e\text{-}4\ r_1^{-5} +4.542e\text{-}2 -3.154e\text{-}2\ r_1^2$,
$k_2\cdot\alpha_3 = -3.046e\text{-}3r_1^{-5} +8.083e\text{-}3r_1^{-3} +4.542e\text{-}2 -5.046e\text{-}2r_1^2$.

For $\eta=0.95$,
$k_2\cdot\alpha_0 = 0.8874\ r_1^{-5} -1.174\ r_1^{-3} +0.7768 -0.8688\ r_1^2$,
$k_2\cdot\alpha_1 = -0.2219\ r_1^{-5} +0.5871\ r_1^{-3} +0.7768 -0.2896\ r_1^2$,
$k_2\cdot\alpha_2 = 7.395e\text{-}2\ r_1^{-5} +0.3884 -0.2413\ r_1^2$,
$k_2\cdot\alpha_3 = -0.2958\ r_1^{-5} +0.2936\ r_1^{-3} +0.3884 -0.3861\ r_1^2$.
These agree with $k_2'\cdot\alpha_0$, $k_2'\cdot\alpha_2$, $k_2'\cdot\alpha_1$, $k_2'\cdot\alpha_3$ in Peale & Cassen (1978) and Meyer *et al.* (2010), except for a typo and two errors in P&C 1978.

where $c_m=(2-\delta_{0m})(2-m)!/(2+m)!$.

We then transform r', θ' and ϕ' to the planet's orbital elements to study the satellite's tidal response at different disturbing frequencies. Let Ω, ω, M, f, i, a denote the planet's longitude of ascending node, argument of pericenter, mean anomaly, true anomaly, inclination relative to the satellite's equatorial plane, and semi-major axis, respectively. Note that these elements are with respect to the inertia frame of reference (χ_0), so $\phi'=\Omega-\psi$, where ψ is the longitude of the basis meridian of χ_1 measured in χ_0 .

The transform is based on

$$P_{lm}(\cos\theta')\cdot\begin{Bmatrix}\cos\\ \sin\end{Bmatrix}(m\phi') = \Sigma_{p=0}^{l} F_{lmp}(i)\begin{Bmatrix}\cos\\ \sin\end{Bmatrix}[m(\Omega-\psi)+(l-2p)(\omega+f)+\kappa_{(l-m)}], \qquad (a32)$$

where $\kappa_x = \begin{cases} 0, & x \text{ is even} \\ -\frac{\pi}{2}, & x \text{ is odd} \end{cases}$,

$$F_{lmp}(i) = \sum_{t=0}^{\min\left[\text{floor}\left(\frac{l-m}{2}\right),\,p\right]} \frac{(2l-2t)!}{t!\,(l-t)!\,2^{2l-2t}} \sin^{l-m-2t} i \sum_{s=0}^{m} \binom{m}{s} \cos^{s} i \sum_{c=\max[0,\,p-t-m+s]}^{\min[l+s,\,m+p+t]-m-2t} \frac{\binom{l-m-2t+s}{c}\binom{m-s}{p-t-c}}{(l-m-2t)!}(-1)^{c-\text{floor}\left(\frac{l-m}{2}\right)}$$

(Kaula 1961), and the Hansen expansion

$$\left(\frac{R_{EM}}{a}\right)^m \begin{Bmatrix}\cos\\ \sin\end{Bmatrix}(nf) = \Sigma_{k=-\infty}^{\infty} X_k^{m,n}(e)\begin{Bmatrix}\cos\\ \sin\end{Bmatrix}(kM). \qquad (a33)$$

So A(r', θ', ϕ', θ, ϕ) is transformed to:

$$A = \Sigma_{m=0}^{2}\Sigma_{p=0}^{2}\Sigma_{q=-\infty}^{\infty} A_{2mpq},$$

$$A_{2mpq} = GMa^{-3} c_m P_{2m}(\cos\theta) F_{2mp}(i) G_{2pq}(e) \times \cos[-m\phi - m\psi + \nu_{2mpq} + \kappa_m],$$

where

$$\nu_{lmpq} = m\Omega + (l-2p)\omega + (l-2p+q)M,$$

$$G_{lpq}(e) = X_{(l-2p+q)}^{-l-1,\,l-2p}(e).$$

Note that $\kappa_{(l-m)} \neq \kappa_m$ when l is 3, 5...

The phase delayed form is

$$A^*_{2mpq} = GMa^{-3} \times c_m P_{2m}(\cos\theta) F_{2mp}(i) G_{2pq}(e) \times \cos[-m\phi - m\psi + \nu_{2mpq} + \kappa_m - \varepsilon_{2mpq}].$$

The frequency of A^*_{lmpq} due to the orbital motion of the perturber and the rotation of the satellite is

$$f_{lmpq} = -m\dot{\psi} + \dot{\nu}_{lmpq} = -m\dot{\psi} + m\dot{\Omega} + (l-2p)\dot{\omega} + (l-2p+q)\dot{M}.$$

In completely damped 1:1 spin-orbit resonance, $\dot{\psi} = \dot{\Omega} + \dot{\omega} + \dot{M}$, so

$$f_{lmpq} = (l-2p-m)\dot{\omega} + (l-2p+q-m)\dot{M}.$$

When $\dot{\omega}/n$ is small, $f_{lmpq} \approx (l-2p+q-m)n$. So

$$A_{2mpq}\dot{A}^*_{2m'p'q'} = G^2M^2a^{-6} c_m c_{m'} P_{2m}(\cos\theta) P_{2m'}(\cos\theta) \times F_{2mp}(i) F_{2m'p'}(i) G_{2pq}(e) G_{2p'q'}(e)(-f_{2m'p'q'}) \times\cos[-m\phi - m\psi + \nu_{2mpq} + \kappa_m] \times\sin[-m'\phi - m'\psi + \nu_{2m'p'q'} + \kappa_{m'} - \varepsilon_{2m'p'q'}]$$

$$= G^2M^2a^{-6} c_m c_{m'} P_{2m}(\cos\theta) P_{2m'}(\cos\theta) \times F_{2mp}(i) F_{2m'p'}(i) G_{2pq}(e) G_{2p'q'}(e) \times(-1)(2-2p'+q'-m')n\cdot\tfrac{1}{2}$$

$$\times\{\sin[-(m'+m)\phi-(m'+m)\psi+\nu_{2m'p'q'}+\nu_{2mpq}+\kappa_{m'}+\kappa_m-\varepsilon_{2m'p'q'}]$$
$$+\sin[-(m'-m)\phi-(m'-m)\psi+\nu_{2m'p'q'}-\nu_{2mpq}+\kappa_{m'}-\kappa_m-\varepsilon_{2m'p'q'}]\} \quad (a34)$$

The secular terms are those with m+m' being even, and

2-2p-m = 2-2p'-m', q=q'

(i.e., $f_{2mpq} = f_{2m'p'q'}$),

or

2-2p-m = -(2-2p'-m'), q=-q'

(i.e., $f_{2mpq} = -f_{2m'p'q'}$).

Apply the form of phase lag in the constant-Q Darwin-Kaula tidal model

$$\varepsilon_{2mpq} = Q^{-1}\,\mathrm{sign}(f_{2mpq}) \quad (a35)$$

to the expression, and ignore the periodic terms, we get the secular part of (a34):

$$\dot{A}^*_{2mpq}A^*_{2m'p'q'}$$
$$=G^2M^2a^{-6}c_mc_{m'}P_{2m}(\cos\theta)P_{2m'}(\cos\theta)$$
$$\times F_{2mp}(i)F_{2m'p'}(i)\,G_{2pq}(e)G_{2p'q'}(e)$$
$$\times \tfrac{1}{2}(2-2p'+q'-m')n\,Q^{-1}\,\mathrm{sign}(2-2p'+q'-m')$$
$$\times\begin{cases}\cos(m-m')\phi & (m+m'even, f_{2mpq}=f_{2m'p'q'})\\ (-1)^m\cos(m+m')\phi & (m+m'even, f_{2mpq}=-f_{2m'p'q'})\\ 0 & (else)\end{cases} \quad (a36)$$

The angle-averaged value is

$$\dot{A}A^*_{\theta\phi\text{-}avg}$$
$$=(4\pi)^{-1}\int_{[0,2\pi]}\int_{[0,\pi]}\dot{A}A^*\cdot\sin\theta\,d\theta\,d\phi$$
$$=G^2M^2a^{-6}nQ^{-1}\cdot\frac{21}{10}(e^2+\frac{403}{56}e^4+\ldots). \quad (a37)$$

$\dot{A}B^*\ldots$, $\dot{A}\dot{B}^*_{\theta\phi\text{-}avg}\ldots$ can be computed in a similar way. Then with (a31), we get the angle-averaged tidal heating:

$$\dot{W}_{\theta\phi\text{-}avg} = \mu G^2M^2nR^2a^{-6}Q^{-1}g^{-2}k_2^2$$
$$\times(21/5\alpha_0^2+42/5\alpha_1^2-252/5\alpha_1\alpha_2+126\alpha_2^2+252/5\alpha_3^2)$$
$$\times(e^2+\frac{403}{56}e^4)+o(e^4). \quad (a38)$$

The total heating rate in the outer layer (up to e^2) is

$$\dot{W}_{total} = \int_{[R\cdot\eta,R]}4\pi r^2\dot{W}_{\theta\phi\text{-}avg}\,dr$$
$$=k_2^2\cdot 28\lambda/\xi\cdot 4\pi\mu G^2M^2nR^5e^2a^{-6}Q^{-1}g^{-2}. \quad (a39)$$[6,7]

Using parameters appropriate for Io[8], (a22) and (a39) give the relationship between $\dot{W}_{total}/(\dot{W}_{total})_{\eta=0}$ and η, as shown in Fig. a1, which agrees well with Peale *et al.* (1979) and Meyer *et al.* (2010).

---

[6] When η=0, we get λ=19, ξ=24, $\dot{W}_{total} = k_2^2\cdot 133/6\cdot 4\pi\mu^E G^2M^2nR^5e^2a^{-6}Q^{-1}g^{-2}$.

[7] R=1.821e8, ρ=3.53, g=179.71, μ=6.5e11, in cgs.

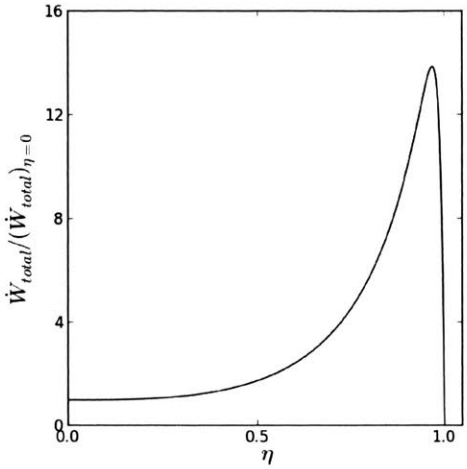

Fig. a1. The dependence of $\dot{W}_{total}$ (scaled with $(\dot{W}_{total})_{\eta=0}$) on η.

References

Aharonson, O., Zuber, M.T. and Solomon, S.C., 2004. Crustal remanence in an internally magnetized non-uniform shell: a possible source for Mercury's magnetic field? *Earth Planet. Sci. Lett.* **218**, 261-268, doi:10.1016/j.epsl.2003.11.020.

Anderson, B.J. *et al.*, 2011. The global magnetic field of Mercury from MESSENGER orbital observations. *Science* **333**, 1859-1862, doi:10.1126/science.1211001.

Anderson, B.J. *et al.*, 2012. Low-degree structure in Mercury's planetary magnetic field. *J. Geophys. Res.* **117**, doi:10.1029/2012JE004159.

Andrews-Hanna, J.C., Zuber, M.T. and Banerdt, W.B., 2008. The Borealis basin and the origin of the martian crustal dichotomy. *Nature* **453**, 1212-1215, doi:10.1038/nature07011.

Beuthe, M., 2013. Spatial patterns of tidal heating. *Icarus*, **223**, 308-329. doi:10.1016/j.icarus.2012.11.020

Bullard, E., Gellman, H., 1954. Homogeneous dynamos and terrestrial magnetism. Phil. Trans. Roy. Soc. London A 247, 213-278.

Cameron, A.G.W., Ward, W.R. 1976. the Origin of the Moon. Proc. Lunar Planet. Sci. Conf. 7, 120.

Canup, R.M. and Asphaug, E. 2001. Origin of the Moon in a giant impact near the end of the Earth's formation. *Nature* **412**, 708. doi:10.1038/35089010

Canup, R.M., 2004. Simulations of a late lunar-forming impact. *Icarus* **168**, 433. doi:10.1016/j.icarus.2003.09.028

Canup, R.M., 2008. Lunar-forming collisions with pre-impact rotation. *Icarus* **196**, 518. doi:10.1016/j.icarus.2008.03.011

Canup, R.M., 2012. Forming a Moon with an Earth-like Composition via a Giant Impact. *Science* **338**, 1052. doi: 10.1126/science.1226073

Cao, H., Aurnou, J.M., Wicht, J., Dietrich, W., Soderlund, K.M., Russell, C.T., 2014. A dynamo explanation for Mercury's anomalous magnetic field. *Geophy. Res. Lett.* **41**, 4127-4134, doi: 10.1002/2014GL060196.

Christensen, U.R., 2006. A deep dynamo generating Mercury's magnetic field. *Nature* **444**, 1056-1058, doi:10.1038/nature05342.

Christensen, U.R., Wicht, J., 2008. Models of magnetic field generation in partly stable planetary cores: Applications to Mercury and Saturn. *Icarus* **196**, 16-34, doi:10.1016/j.icarus.2008.02.013.

Cuk, M. and Stewart, S.T. 2012. Making a Moon from a Fast-Spinning Earth: A Giant Impact Followed by Resonance Despinning. *Science* **338**, 1047. doi:10.1126/science.1225542

Dharmaraj, G., Stanley, S., Qu, A.C., 2014. Scaling laws, force balances and dynamo generation mechanisms in numerical dynamo models: influence of boundary conditions. *Geophys. J. Int.* **199**, 514-532, doi:10.1093/gji/ggu274.

Elkins-Tanton, L.T., 2008. Linked magma ocean solidification and atmospheric growth for Earth and Mars. *EPSL* **271**, 181–191.

Elkins-Tanton, L., Burgess, S., Yin, Q.-Z. 2011. The lunar magma ocean: Reconciling the solidification process with lunar petrology and geochronology. *EPSL* **304**, 326. doi:10.1016/j.epsl.2011.02.004

Giampieri, G., Balogh, A., 2002. Mercury's thermoelectric dynamo model revisited. *Planet. Space Sci.* **50**, 757-762, doi:10.1016/S0032-0633(02)00020-X.

Glassmeier, K.-H., Auster, H.-U., Motschmann, U., 2007. A feedback dynamo generating Mercury's magnetic field. *Geophy. Res. Lett.* **34**, L22201, doi: 10.1029/2010GL044533.

Goldreich, P., 1963. On the eccentricity of satellite orbits in the Solar System. *Mon. Not. R. Astron. Soc.* **126**, 257–268.

Goldreich, P., 1966. History of the lunar orbit. *Rev. Geophys. Space Phys.* **4**, 411–439.

Gomez-Perez, N., Solomon, S.C., 2010. Mercury's weak magnetic field: A result of magnetospheric feedback? *Geophy. Res. Lett.* **20**, L20204, doi:10.1029/2010GL044533.

Grote, E., Busse, F.H., Tilgner, A., 2000. Effects of hyperdiffusivities on dynamo simulations. *Geophy. Res. Lett.* **27**, 2001-2004, doi:10.1029/1999GL011155.

Hartmann, W.K., Davis, D.R., 1975. Satellite-sized planetesimals and lunar origin. *Icarus* **24**, 504. doi:10.1016/0019-1035(75)90070-6

Hauck, S.A., Dombard, A.J., Phillips, R.J., Solomon, S.C., 2004. Internal and tectonic evolution of Mercury. *Earth Planet. Sci. Lett.* **222**, 713-728, doi:10.1016/j.epsl.2004.03.037.

Hauck, S.A., Margot, J.-L., Solomon, S.C., Phillips, R.J., Johnson, C.L., Lemoine, F.G., Mazarico, E., McCoy, T.J., Padovan, S., Peale, S.J., Perry, M.E., Smith, D.E., Zuber, M.T., 2013. The curious case of Mercury's internal structure. *J. Geophys. Res.* **118**, 1204-1220, doi:10.1002/jgre.20091.

Hut, P., 1981. Tidal evolution in close binary systems. *Astron. Astrophys.* **99**, 126–140.

Head, J.W. *et al.*, 2011. Flood volcanism in the northern high latitudes of Mercury revealed by MESSENGER. *Science* **333**, 1853-1856, doi:10.1126/science.1211997.

Heimpel, M.H., Aurnou, J.M., Al-Shamali, F.M., Gomez Perez, N., 2005. A numerical study of dynamo action as a function of spherical shell geometry. *Earth Planet. Sci. Lett.* **236**, 542-557, doi:10.1016/j.epsl.2005.04.032.

Hess, P.C., Parmentier, E.M., 1995. A model for the thermal and chemical evolution of the Moon's interior: implications for the onset of mare volcanism. *Earth Planet. Sci. Lett.* **134**, 501-514.

Heyner, D. *et al.*, 2010. The initial temporal evolution of a feedback dynamo for Mercury. *Geophys. Astrophys. Fluid Dyn.* **104**, 419-429, doi:10.1080/03091921003776839.

Heyner, D. *et al.*, 2011. Evidence from numerical experiments for a feedback dynamo generating Mercury's magnetic field. *Science* **334**, 1690-1693, doi:10.1126/science.1207290.

Kaib, N., Cowan, N. B., 2015. The feeding zones of terrestrial planets and insights into Moon formation. *Icarus* **252**, 161-174. doi:10.1016/j.icarus.2015.12.042

Kaula, W. M. 1961. Analysis of Gravitational and Geometric Aspects of Geodetic Utilization of Satellites. *Geophy. J. Int.* **5**, 104-133. doi:10.1111/j.1365-246X.1961.tb00417.x

Kaula, W.M., 1964. Tidal dissipation by solid friction and the resulting orbital evolution. *Rev. Geophys.* **2**, 661–685. doi:10.1029/RG002i004p00661

Kaula, W.M., 1974. Apollo laser altimetry and inferences as to lunar surface structure, Proc. Lunar Planet. Sci. Conf. 5, 3049-3058.

Kivelson, M.G., Khurana, K.K., Volwerk, M., 2002. The permanent and inductive magnetic moments of Ganymede. *Icarus* **157**, 507-522, doi:10.1006/icar.2002.6834.

Kuang, W., Bloxham, J., 1999. Numerical modeling of magnetohydrodynamic convection in a rapidly rotating spherical shell: weak and strong field dynamo action. *J. Comp. Phys.* **153**, 51-81, doi:10.1006/jcph.1999.6274.

Laneuville, M., Wieczorek, M. A., Breuer, D., Tosi, N., 2013. Asymmetric thermal evolution of the Moon. *JGR:Planets* **118**, 1435-1452.

Lock, S. J., Stewart, S. T., Petaev, M. I., Leinhardt, Z. M., Mace, M., Jacobsen, S. B., Cuk, M., 2016. A new model for lunar origin: equilibration with Earth beyond the hot spin stability limit. LPSC XXXXVII.

Longhi, J., 2003. A new view of lunar ferroan anorthosites: Postmagma ocean petrogenesis. *Journal of Geophysical Research* **108**, 1. doi:10.1029/2002JE001941

Love, A. E. H. 1944. A Treatise on the Mathematical Theory of Elasticity, 4th Ed. Dover publications, New York.

Love, J.J., 2000. Dynamo action and the nearly axisymmetric magnetic field of Saturn. *Geophys. Res. Lett.* **27**, 2889-2892, doi:10.1029/1999GL008466.

Lugmair, G.W., Shukolyukov, A., 1998. Early solar system timescales according to ^{53}Mn-^{53}Cr systematics. *Geochim. Cosmochim. Acta* **62**, 2863. doi:10.1016/S0016-7037(98)00189-6.

Margot, J.-L. *et al.*, 2007. Large longtitude libration of Mercury reveals a molten core. *Science* **316**, 710-714, doi:10.1126/science.1140514.

Margot, J.-L. *et al.*, 2012. Mercury's moment of inertia from spin and gravity data. *J. Geophy. Res.* **117**, doi:10.1029/2012JE004161.

Mastrobuono-Battisti, A., Perets, H.B., Raymond, S.N., 2015. A primordial origin for the compositional similarity between the Earth and the Moon. *Nature* **520**, 212. doi:10.1038/nature14333

Melosh, H.J., 2009. An isotopic crisis for the giant impact origin of the Moon? In: Annual Meeting of the Meteoritical Society LXXII, p. 5104.

Meyer, J., Elkins-Tanton, L., Wisdom, J., 2010. Coupled thermal-orbital evolution of the early Moon. *Icarus* **208**, 1-10. doi:10.1016/j.icarus.2010.01.029

Michel, N.C. *et al.*, 2013. Thermal evolution of Mercury as constrained by MESSENGER observations. *J. Geophy. Res.* **118**, 1033-1044, doi:10.1002/jgre.20049.

Mignard, F., 1979. The evolution of the lunar orbit revisited. I. *Moon Planets* **20**, 301-315. doi: 10.1007/BF00907581

Nittler, L.R. *et al.*, 2011. The major-element composition of Mercury's surface from MESSENGER X-ray spectrometry. *Science* **333**, 1847-1850, doi:10.1126/science.1211567.

Ojakangas, G.W., Stevenson, D.J., 1986. Episodic Volcanism of Tidally Heated Satellites with Application to Io. *Icarus* **66**, 341. doi:10.1016/0019-1035(86)90163-6

Pahlevan, K., Stevenson, D.J., 2007. Equilibration in the aftermath of the lunar-forming giant impact. *EPSL* **262**, 438. doi:10.1016/j.epsl.2007.07.055

Peale, S.J., 1976. Excitation and relaxation of the wobble, precession, and libration of the Moon. *J. Geophys. Res.* **81**, 1813–1827.

Peale, S.J., 1977. Rotation histories of the natural satellites. In: Natural Satellites. U. Arizona.

Peale, S.J., Cassen, P., 1978. Contribution of tidal dissipation to lunar thermal history. *Icarus* **36**, 245. doi:10.1016/0019-1035(78)90109-4

Peale, S.J., Cassen, P., Reynolds, R.T., 1979. Melting of Io by Tidal Dissipation. *Science* **203**, 892-894. doi: 10.1126/science.203.4383.892

Peplowski, P.N. *et al.*, 2012. Variations in the abundances of potassium and thorium on the surface of Mercury: Results from the MESSENGER Gamma-Ray Spectrometer. *J. Geophy. Res.* **117**, doi:10.1029/2012JE004141.

Plummer, H.C., 1960. An Introductory Treatise on Dynamical Astronomy. Dover.

Pozzo, M. *et al.*, 2012. Thermal and electrical conductivity of iron at Earth's core conditions. *Nature* **485**, 355-358, doi:10.1038/nature11031.

Reufer, A, Meier, M.M.M., Benz, W., Wieler, R., 2012. A hit-and-run giant impact scenario. *Icarus* **221**, 296. doi: 10.1016/j.icarus.2012.07.021

Schubert, G., Chan, K.H., Liao, X., Zhang, K., 2004. Planetary dynamos: effects of electrically conducting flows overlying turbulent regions of magnetic field generation. *Icarus* **172**, 305-315, doi:10.1016/j.icarus.2004.06.007.

Smith, D.E. *et al.*, 2012. Gravity field and internal structure of Mercury from MESSENGER. *Science* **336**, 214-217, doi:10.1126/science.1218809.

Smith, D. E., Zuber, M. T., Neumann, G. A., Mazarico, E., Lemoine, F. G., Head III, J. W., Lucey, P. G., Aharonson, O., Robinson, M. S., Sun, X., Torrence, M. H., Barker, M. K., Oberst, J., Duxbury, T. C., Mao, D., Barmouin, O. S., Jha, K., Rowlands, D. D., Goossens, S., Baker, D., Bauer, S., Gläser, P., Lemelin, M., Rosenburg, M., Sori, M. M., Whitten, J., McClanahan, T., 2016. Summary of the results from the Lunar Orbiter Laser Altimeter after seven years in orbit. *Icarus*. doi: 10.1016/j.icarus.2016.06.006.

Smith, E.J. *et al.*, 1980. Saturn's magnetic field and magnetosphere. *Science* **207**, 407-410, doi:10.1126/science.207.4429.407.

Srnka, L., 1976. Magnetic dipole moment of a spherical shell with TRM acquired in a field of internal origin. *Phys. Earth Planet. Int.* **11**, 184–190

Stanley, S., Bloxham, J., 2004. Convective-region geometry as the cause of Uranus' and Neptune's unusual magnetic fields. *Nature* **428**, 151-153, doi:10.1038/nature02376.

Stanley, S. *et al.*, 2005. Thin shell dynamo models consistent with Mercury's weak observed magnetic field. *Earth Planet. Sci. Lett.* **234**, 27-38, doi:10.1016/j.epsl.2005.02.040.

Stanley, S., Bloxham, J., 2006. Numerical dynamo models of Uranus' and Neptune's magnetic fields. Icarus 184, 556-572, doi:10.1016/j.icarus.2006.05.005.

Stanley, S. *et al.*, 2008. Mars' paleomagnetic field as the result of a single-hemisphere dynamo. *Science* **26**, 1822-1825, doi:10.1126/science.1161119.

Stanley, S., Mohammadi, A., 2008. Effects of an outer thin stably stratified layer on planetary dynamos. *Phys. Earth Planet. Inter.* **168**, 179-190, doi:10.1016/j.pepi.2008.06.016.

Stanley, S., 2010. A dynamo model for axisymmetrizing Saturn's magnetic field. *Geophy. Res. Lett.* **37**, doi:10.1029/2009GL041752.

Stanley, S., Glatzmaier, G.A., 2010. Dynamo models for planets other than Earth. *Space Sci. Rev.* **152**, 617-649, doi:10.1007/s11214-009-9573-y.

Stegman, D. R., Jellinek, A. M., Zatman, S. A., Baumgardner, J. R., Richards, M. A., 2003. An early lunar core dynamo driven by thermalchemical mantle convection. *Nature* **421**, 143-146.

Stephenson, A., 1975. Crustal remanence and the magnetic moment of Mercury. *Earth Planet. Sci. Lett.* **28**, 454–458.

Stevenson, D.J., 1980. Saturn's luminosity and magnetism. *Science* **208**, 746-748, doi:10.1126/science.208.4445.746.

Stevenson, D.J., 1982. Reducing the non-axisymmetry of a planetary dynamo and an application to Saturn. *Geophys. Astrophys. Fluid Dyn.* **21**, 113-127, doi:10.1080/03091928208209008.

Stevenson, D.J., 1987. Mercury's magnetic field: a thermoelectric dynamo? *Earth Planet. Sci. Lett.* **82**, 114-120, doi:10.1016/0012-821X(87)90111-7

Sussman, G.J., Wisdom, J., 2015. Structure and Interpretation of Classical Mechanics, second edition, MIT Press. ISBN:9780262028967

Takahashi, F., Matsushima, M., 2006. Dipolar and non-dipolar dynamos in a thin shell geometry with implications for the magnetic field of Mercury. *Geophys. Res. Lett.* **33**, doi:10.1029/2006GL025792.

Touboul, M., Klein, T., Bourdon, B., Palme, H., Weiler, R., 2007. Late formation and prolonged differentiation of the Moon inferred from W isotopes in lunar metals. *Nature* **450**, 1206. doi:10.1038/nature06428

Touma, J., Wisdom, J., 1993. Lie–Poisson integrators for rigid body dynamics in the Solar System. *Astron. J.* **107**, 1189–1202. doi: 10.1086/116931

Touma, J., Wisdom, J., 1994. Evolution of the Earth–Moon system. *Astron. J.* **108**,1943–1961.

Touma, J., Wisdom, J., 1998. Resonances in the Early Evolution of the Earth-Moon System. *Astron. J.* **115**, 1653.

Turcotte, D.L., Schubert, G., 2002. Geodynamics, Cambridge University Press, Cambridge.
van der Hilst, R.D. *et al.*, 2007. Seismostratigraphy and thermal structure of Earth's core-mantle boundary region. *Science* **315**, 1813-1817, doi:10.1126/science.1137867.
Vilim, R., Stanley, S. and Hauck, S.A., 2010. Iron snow zones as a mechanism for generating Mercury's weak observed magnetic field. J. Geophy. Res. 115, doi:10.1029/2009JE003528.
Wahr, J. M., Zuber, M. T., Smith, D. E., Lunine, J. I., 2006. Tides on Europa, and the thickness of Europa's icy shell. *Journal of Geophysical Research*, **111**, E12005. doi:10.1029/2006JE002729.
Wang, K., Jacobsen, S. B., 2016. Potassium isotopic evidence for a high-energy giant impact origin of the Moon. *Nature* doi:10.1038/nature19341.
Weider, S.Z. *et al.*, 2015. Evidence for geochemical terranes on Mercury: Global mapping of major elements with MESSENGER's X-Ray Spectrometer. *Earth Planet. Sci. Lett.* **416**, 109-120, doi: 10.1016/j.epsl.2015.01.023.
Wiechert, U., Halliday, A.N., Lee, D.-C., Snyder, G.A., Taylor, L.A., Rumble, D., 2001. Oxygen Isotopes and the Moon-Forming Giant Impact. *Science* **294**, 345. doi:10.1126/science.1063037
Wieczorek, M.A. *et al.*, 2013. The Crust of the Moon as Seen by GRAIL. *Science* **339**, 671-675. doi:10.1126/science.1231530
Williams, J.G., Boggs, D.H., Ratcliff, J.T., 2005. Lunar fluid core and solid-body tides. LPSC XXXVI, p. 1503.
Williams, J. G. *et al.*, 2014. Lunar interior properties from the GRAIL million. *JGR Planets* **119**, 1546–1578. doi:10.1002/2013JE004559
Winslow, R.M. *et al.*, 2014. Mercury's surface magnetic field determined from proton-reflection magnetometry. *Geophys. Res. Lett.* **41**, 4463-4470, doi:10.1002/2014GL060258.
Wisdom, J., Holman, M., 1991. Symplectic maps for the N-body problem. *Astron. J.* **102**, 1528–1538. doi:10.1086/115978
Wisdom, J., Tian, Z., 2015. Early evolution of the Earth–Moon system with a fast-spinning Earth. *Icarus* **256**, 138. doi:10.1016/j.icarus.2015.02.025
Yoder, C., Peale, S.J., 1981. The tides of Io. *Icarus* **47**, 1–35.
Zahnle, K., Arndt, N., Cockell, C., Halliday, A., Nisbet, E., Selsis, F., Sleep, N.H., 2007. Emergence of a habitable planet. *Space Sci. Rev.* **129**, 35-78. doi:10.1007/s11214-007-9225-z
Zhang, J., Dauphas, N., Davis, A.M., Leya, I., Fedkin, A., 2012. The proto-Earth as a significant source of lunar material. *Nat. Geosci.* **5**, 240. doi:10.1038/ngeo1429

Zhang, K., Jones, C.A., 1997. The effect of hyperviscosity on geodynamo models. *Geophy. Res. Lett.* **24**, 2869-2872, doi:10.1029/97GL02955.

Zhong, S., Parmentier, E.M., Zuber, M. T., 2000. A dynamic origin for the global asymmetry of lunar mare basalts. *EPSL* **177**, 131-140.

Zuber, M. T., Smith, D. E., Lemoine, F. G., Neumann, G. A., 1994. The shape and internal structure of the Moon from the Clementine mission. *Science* **266**, 1839-1843.